Contributions to Robust Chromatic Digital Image Processing

By

Ramón Moreno Jiménez

http://www.ehu.es/ccwintco

Dissertation presented to the Department of Computer Science
and Artificial Intelligence in partial fulfillment of the
requirements for the degree of
Doctor of Philosophy

PhD Advisor:

Prof. Manuel Graña Romay

Dr. Alicia D'Anjou D'Anjou

At
The University of the Basque Country
Donostia - San Sebastian
2012

emen ta zabal zazu

Universidad del País Vasco
Euskal Herriko Unibertsitatea

AUTORIZACION DEL/LA DIRECTOR/A DE TESIS PARA SU PRESENTACION

Dr/a. ____ con N.I.F. ________________________

como Director/a de la Tesis Doctoral: ____

____

____

realizada en el Departamento ____

____

por el Doctorando Don/ña. ____ ,

autorizo la presentación de la citada Tesis Doctoral, dado que reúne las condiciones necesarias para su defensa.

En ________________ a _____ de ___________________ de _____

EL/LA DIRECTOR/A DE LA TESIS

Fdo.: _______________________________

emman ta zabal zazu

Universidad del País Vasco Euskal Herriko Unibertsitatea

CONFORMIDAD DEL DEPARTAMENTO

El Consejo del Departamento de ____

____

en reunión celebrada el día ____ de ___________ de _____ ha acordado dar la conformidad a la admisión a trámite de presentación de la Tesis Doctoral titulada: ___________

____

____

dirigida por el/la Dr/a. ____

____

y presentada por Don/ña. ____

ante este Departamento.

En ________________a _____de ___________________de _____

Vº Bº DIRECTOR/A DEL DEPARTAMENTO SECRETARIO/A DEL DEPARTAMENTO

Fdo.: ________________________________ Fdo.: ____________________________

eman ta zabal zazu

Universidad del País Vasco
Euskal Herriko Unibertsitatea

AUTORIZACIÓN DE LA COMISIÓN ACADÉMICA DEL PROGRAMA DE DOCTORADO

La Comisión Académica del Programa de Doctorado en ____

____

en reunión celebrada el día ____ de _______________ de _____ ha acordado dar la

conformidad a la presentación de la Tesis Doctoral titulada: ____________________________

____

____

dirigida por el/la Dr/a. ____

____

y presentada por Don/ña. ____

e inscrita en el Departamento____.

En __________________a _____de ______________________de _____

EL COORDINADOR O COORDINADORA DEL PROGRAMA DE DOCTORADO

Fdo.: __________________________________

eman ta zabal zazu

Universidad del País Vasco
Euskal Herriko Unibertsitatea

ACTA DE GRADO DE DOCTOR

ACTA DE DEFENSA DE TESIS DOCTORAL

DOCTORANDO DON/ÑA. ____

TITULO DE LA TESIS: ____

____

____

El Tribunal designado por la Subcomisión de Doctorado de la UPV/EHU para calificar la Tesis Doctoral arriba indicada y reunido en el día de la fecha, una vez efectuada la defensa por el doctorando y contestadas las objeciones y/o sugerencias que se le han formulado, ha otorgado por__________________la calificación de:
unanimidad ó mayoría

En ________________ a _____de ___________________de _____

EL/LA PRESIDENTE/A, EL/LA SECRETARIO/A,

Fdo.: Fdo.:

Dr/a: ____________________ Dr/a: ______________________

VOCAL 1º, VOCAL 2º, VOCAL 3º,

Fdo.: Fdo.: Fdo.:

Dr/a: ____________________Dr/a:______________________Dr/a:____________________

EL/LA DOCTORANDO/A,

Fdo.: __

Acknowledgments

I would like to thank my advisor, Prof. Manuel Graña, who caught me some years ago and led me to this exciting research life. Thanks for his invaluable guidance. I am grateful for his wisdom, encouragement and patience. I extend too this thank to Dr. Alicia D'Anjou for her support and follow up.

I would thank to Prof. Kurosh Madani from LISSI (Paris-Est Créteil Val-de-Marne University, France) who gave me the chance to share three months with his research group, where I had the opportunity to experiment with robot vision systems.

I would thank to Dr. José Carlos Neves Epiphanio from DSR (Instituto Nacional de Pesquisas Espaciais - INPE, Brazil) who gave me the chance to share three months into his research center, where I had the opportunity to play with multispectral and hyperspectral images.

I would thank to the Basque Government for the financial support through the FPI grant (Formación de Personal Investigador - BF108.207) which has allowed to fulfil this Thesis and its internships.

I would thank at last and not at least, to my family, friends and colleagues of GIC research group. Una mención especial a Natalia quien me ha visto envejecer desde que cogí el primer libro. Gracias también a *mamá* y a *Txús*, vosotros hacéis la vida más bonita.

Thanks so much to everybody!

Ramón Moreno Jiménez

“Para papá y para Félix”

Contributions to Robust Chromatic Digital Image Processing by

Ramón Moreno Jiménez

Submitted to the Deapartament od Computer Science and Artificial Intelligence on the May 7, 2012, in partial fulfillment of the requirements for the degree of Doctor of Philosophy

abstract

This Thesis deals with digital image segmentation starting from a physical analysis of image formation under the Dichromatic Reflection Model (DRM), pursuing color constancy (CC) properties such as those shown by the human vision system, as psychology vision research has demonstrated. In order to provide robustness regarding illumination changes, first we perform illumination correction. By estimating the illumination chromaticity is possible to normalize the image respect to the illumination accomplishing some degree of CC in image processing. Afterwards, it is possible to separate the diffuse and specular image components. Once the image is normalized, we proceed to the image segmentation, where the key innovative tools introduced in this Thesis are a chromatic gradient and a hybrid gradient defined over a new chromatic distance. Most of this work is based on the identification of Spherical coordinates representation of the colors in the RGB cube, which allow to work with image chromaticity in straightforward manner. Segmentation methods proposed in this Thesis work in the image domain. Specifically, this Thesis proposes two approaches, one is a region growing and the other is a Watershed Transformation. First half of this thesis is focused on RGB images whereas the second one is devoted to the extrapolation of the segmentation methods to hyperspectral images through the use of Hyperspherical coordinates.

Contents

List of Figures

List of Tables

Chapter 1

Introduction

1.1 Thesis Context

The overall context of this Thesis is the processing of digital images for robust segmentation. The kind of images treated are conventional RGB images and hyperspectral images. The transition from low dimensional valued images to high dimensional valued images introduces additional problems due to the curse of dimensionality, and it is by no means trivial. Nevertheless, we have had some success porting the same philosophy to obtain robust image segmentation methods. The meaning of the word "robust" in this Thesis is intimately associated with the Color Constancy property of the human vision, and the branch of artificial vision that tries to reproduce it for the design of improved digital image processing algorithms. Color Constancy means that human can perceive the same color surface despite the changes imposed by illumination effects. In this Thesis we have focused on avoiding the false segmentations introduced by highlights and shadows in the images. Highlights are image regions of high intensity due to the particular strong reflection of the illumination on some specific surface patch. Shadows are dark image regions produced by the occlusion of some surface patch relative to the illumination source. Highlights and shadows are primarily effect on the achromatic component of the image, therefore, the main aim of the Thesis has been to identify efficiently the chromatic components of the image in order to perform the image segmentation operations on them, thus avoiding the effects on the achromatic component.

The works pursued in this Thesis have touched several aspects of image processing, the two most salient are:

- The Dichromatic Reflection Model, which has served as the guiding and supporting model for most of the processes proposed and tested in this thesis. The basic decomposition into diffuse and specular components, has served to predict the effects of the proposed algorithms, and to explain sometimes the results obtained.

- The spherical coordinate representation, which provides the chromatic characterization of the image. After computing this representation, discarding all the effects of the illumination is immediately achieved by discarding the luminosity component. Using this representation we do not need to perform color space transformations for the extraction of the chromatic information. We have found also straightforward to extend this approach to the hyperspectral image domain, contrary to any other color space representation, whose high-dimensional correspondent is not known. Therefore, the spherical coordinate representation is the key for the definition of robust chromatic processing of hyperspectral images.

The kind of image segmentation pursued is twofold. We have developed approaches for region growing and gradient based segmentation, including chromatic variations of the well known watershed algorithm. Robust region based segmentation means that the identified regions are chromatically homogeneous and no homogeneous chromatic region is partitioned in several regions. Specifically, shadowed regions are expected to be ignored, and included in larger regions of the same color, despite its low intensity. Highlight regions are also expected to be ignored and included in the larger homogeneous regions. These goals are not easy to achieve, depending on factors such as the quality of the camera, or the existence of motion artifacts (for instance in robotic applications). For edge detection segmentation based on chromatic gradients, the sought effect is the absence of spurious edges produced by the shadow or highlight borders.

Finally, we have found that the chromatic processing is quite sensitive to noise in the dark regions of the image. This effect is easy to explain taking into account that small color perturbations in the vicinity of the space origin may introduce large angular variations. To overcome this problem, we have proposed hybrid approaches combining chromatic and achromatic distances.

1.2 Thesis Framework

The scheme in Fig. 1.1 summarizes the works developed on RGB images that are presented in the ensuing chapters. The basic flow is that the input image is subject to some preprocessing operations (light blue regions of the scheme) previous to the segmentation (green) which produces the output image. The paths that can be followed from input to output image correspond to some of the approaches proposed, developed and tested.

One approach is to compute the specular free image (block label 8), removing highlights and enhancing the chromatic content of the image, and apply a simple thresholding approach (block label 9) to identify the regions of interest. We have pursued such an approach in some robotic applications.

Other approaches may combine several processes, always based in the spherical representation of the RGB color (block label 1):

- Perform the illumination source chromaticity estimation (block label 2), which allows the image chromatic normalization (block label 3) so that the resulting image corresponds to the image obtained with a pure white illuminant. This process is needed when the ensuing processes assume white illumination.

- The normalized image can be subject to the separation of diffuse and specular components (block label 4) so that the diffuse image can be used for further robust region segmentation and the specular image can be used to obtain some geometrical information.

- The normalized image can be used to compute the chromatic (or hybrid) gradient, which allows the detection of edges (block label 5).

- The watershed segmentation (block label 6) uses the chromatic gradient image to perform the flooding process and identify regions. It uses also the chromatic distance for region merging into coherent color image regions.

- The region growing (block label 7) uses the chromatic distance on the normalized image to obtain the region segmentation in one pass over the image.

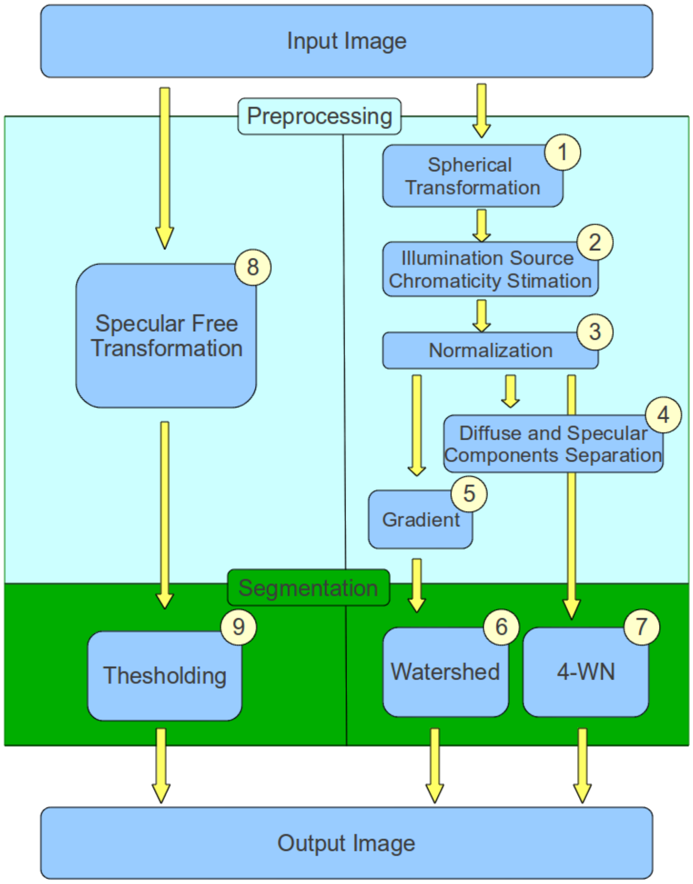

Figure 1.1: Schema of the first part of the thesis. On RGB images.

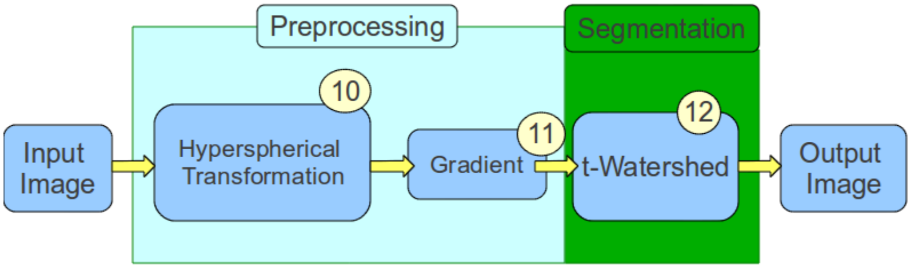

Figure 1.2: Scheme of the second part of the thesis. On hyperspectral images.

All these processes are the subject of some chapter in this Thesis, were we explain our attempts to define and apply the above ideas to develop them. The extension to the hyperspectral image domain is illustrated in Fig. 1.2. Here we have a simple linear pipeline, where the input image is subject to the computation of the hyperspherical coordinates for the subsequent processes (block 10). The hyperspectral chromatic gradient is computed on this representation after removal of the luminosity component (block label 11). Finally, the watershed algorithm is computed on the gradient information (block label 12). These processes are the subject of the last chapters of the Thesis. In fact, the processing of hyperspectral images is the main avenue for future works after the Thesis presentation.

1.3 Thesis Outline

Each of the chapters explaining the contributions of this Thesis has a specific conclusions section, therefore we do not introduce a final chapter of conclusions and further work.

Chapter 2 contains introductory material about color, color spaces, the Dichromatic Reflectance Model, and image segmentation algorithms.

Chapter 3 contains four approaches to the problem of color image normalization, including the separation of diffuse and specular reflectance components supported by the DRM introduced in the first chapter.

Chapter 4 contains two approaches to specular free image transformation, the first one has been applied to a practical problem of detection and following of robots in an scene.

Chapter 5 contains the definition and experimental results of a chromatic gradient operator based on the chromatic distance defined on the angular distance among the vector representation of the RGB color space points.

Chapter 6 contains the description of image segmentation contributions performed on the basis of the chromatic distance defined on the spherical coordinate representation of pixel coordinates in RGB color space. These contributions are a robust region growing algorithm and chromatic watershed segmentation algorithm.

Chapter 7 contains some introductory material on hyperspectral images and the definition of chromatic ideas based on the hyperspherical coordinate representation that is used in the ensuing chapters.

Chapter 8 contains gradient operator definitions on the hyperspectral images, considering the hypersherical representation and a hybridization to allow for improved edge detection in dark regions.

Chapter 9 contains the contributions on hyperspectral region segmentation using the chromatic gradient hyperspherical coordinates for watershed segmentation.

1.4 Publications performed in this Thesis

1. R. Moreno, M. A. Veganzones, and M. Graña, A Remote Mycological Assistant, 4th IEEE Workshop on Intelligent Data Acquisition and Advanced Computing Systems Technology and Applications IDAACS, pp. 408-412, 2007.
2. R. Moreno, Inteligencia Ambiental, Sistemas Ubícuos y Visión por computador en Telefonía Móvil. Estado del arte, in Actas de las I jornadas de Inteligencia Computacional (M. Veganzones & R. Moreno, ed.), pp. 417-431, Servicio editorial UPV/EHU, 2007. ISBN 978-84-9860-019-3.

3. R. Moreno, Visión por Computador y Clasicación Aplicadas a la Micología, in Actas de las I jornadas de Inteligencia Computacional (M. A. Veganzones & R. Moreno, ed.), pp. 208-224, Servicio editorial UPV/EHU, 2007. ISBN 978-84-9860-019-3.

4. R. Moreno, M. Graña, and A. d'Anjou, Evolutive Parametric Approach for Specular Correction in the Dichromatic Reflection Model, in Hybrid Articial Intelligence Systems, vol. 5271 of Lecture Notes in Computer Science, pp. 665-672, Springer Berlin / Heidelberg, 2008.

5. R. Moreno, Reflectance Analysis I, in Actas de las II jornadas de Inteligencia Computacional (A. Savio & R. Moreno, ed.), pp. 258-269, Servicio editorial UPV/EHU, 2008. ISBN 978-84-296-2316-1.

6. R. Moreno, Estimación de la Cromacidad de la luz, in Actas de las III Jornadas de Inteligencia Computacional (J.M. López Guede, ed.), pp. 159-170, Servicio editorial UPV/EHU, 2009. ISBN: 978-84-9860-320-0.

7. I. Villaverde, Z. Echegoyen and R. Moreno. Control Visual para Multirobots, Implementación de una Prueba de Concepto de un SRMC Enlazado, in Actas de las III jornadas de Inteligencia Computacional, Servicio editorial UPV/EHU, 2009. ISBN: 978-84-9860-320-0.

8. R. Moreno, M. Graña , A. d'Anjou, and C. Hernandez, Bayesian Reflectance Component Separation, in Knowledge-Based and Intelligent Information and Engineering Systems, vol. 5712 of Lecture Notes in Computer Science, pp. 846-852, Springer Berlin / Heidelberg, 2009.

9. R. Moreno, J. López-Guede, and A. d'Anjou, Hybrid Color Space Transformation to Visualize Color Constancy, in Hybrid Articial Intelligence Systems, vol. 6077 of Lecture Notes in Computer Science, pp. 241-247, Springer Berlin / Heidelberg, 2010.

10. R. Moreno, M. Graña, and A. d'Anjou, A Color Transformation for Robust Detection of Color Landmarks in Robotic Contexts, in Trends in Practical Applications of Agents and Multiagent Systems, vol. 71 of Advances in Soft Computing, pp. 665-672, Springer Berlin / Heidelberg, 2010.

11. Z. Echegoyen, I. Villaverde, R. Moreno, M. Graña, and A. d'Anjou, Linked Multi-component Mobile Robots: Modeling, Simulation and

Control, Robotics and Autonomous Systems, vol. 58, pp. 1292-1305, Dec. 2010.

12. R. Moreno, M. Graña, and E. Zulueta, Rgb Colour Gradient Following Colour Constancy Preservation, Electronics Letters, vol. 46, no. 13, pp. 908-910, 2010.

13. I. Villaverde, Z. Echegoyen, R. Moreno, and M. Graña, Experiments on Robotic Multi-agent System for Hose Deployment and Transportation, in Trends in Practical Applications of Agents and Multiagent Systems, vol. 71 of Advances in Soft Computing, pp. 573-580, Springer Berlin / Heidelberg, 2010.

14. R. Moreno, M. Graña, and A. d'Anjou, An image Color Gradient Preserving Color Constancy, in Fuzzy Systems (FUZZ), 2010 IEEE International Conference on, pp. 1-5, july 2010.

15. R. Moreno, M. Graña, and A. d'Anjou, A hybrid Color Distance for Image Segmentation, in Hybrid Articial Intelligent Systems (E. Corchado, M. Kurzynski, and M. Wozniak, eds.), vol. 6679 of Lecture Notes in Com- puter Science, pp. 447-454, Springer Berlin / Heidelberg, 2011.

16. R. Moreno, M. Graña, and A. d'Anjou, A Geometrical Method of Difuse and Specular Image Components Separation, in Advances in Computational Intelligence (J. Cabestany, I. Rojas, and G. Joya, eds.), vol. 6692 of Lecture Notes in Computer Science, pp. 83-89, Springer Berlin / Heidelberg, 2011.

17. R. Moreno, M. Graña, and A. d'Anjou, Illumination Source Chromaticity Estimation Based on Spherical Coordinates in Rgb, Electronics Letters, vol. 47, no. 1, pp. 28-30, 2011.

18. R. Moreno, M. Graña, D. Ramik and K. Madani. Image Segmentation by Spherical Coordinates, in Proceedings of the 11th International Conference on Pattern Recognition and Information Processing, pp. 112-115, Belarusian State University of Informatics and Radioelectrics, MAY 2011.

19. L. Rossi, R. Moreno, K. Madani, M. Graña, V. Amarger, D. M. Ramík, Wildland Fires' Outlines Extraction a Spherical Coordinates Framed

Rgb Color Space Dichromatic Feflection Model Based Image Segmentation Approach, in Proceedings of the 11th International Conference on Pattern Recognition and Information Processing, pp. 451-454, Belarusian State University of Informatics and Radioelectrics, May 2011.

20. R. Moreno and M. Graña, About Gradient Operators on Hyperspectral Images, in Proceedings of the 1st International Conference on Pattern Recognition Applications and Methods, pp. 433-437, SciTePress, 2012.

21. R. Moreno and M. Graña, A hybrid Gradient for n-Dimensional Images through Hyperspherical Coordinates, in Hybrid Articial Intelligent Sys- tems (E. Corchado, et. al., eds.), vol. 7209 of Lecture Notes in Computer Science, pp. 404-415, Springer Berlin / Heidelberg, 2012.

22. R. Moreno, M. Graña and A. d'Anjou, Hyperspectral image segmentation by t-watershed and hyperspherical coordinates, in Knowledge-Based and Intelligent Information and Engineering Systems, 2012. (accepted)

23. R. Moreno, M. Graña, D. Ramik and K. Madani, Image Segmentation on the Spherical Coordinate Representation of the Rgb Color Space, IET Image Processing, 2012. (in review)

1.5 Symbols

Symbol	Description
θ	Zenith angle
ϕ	Azimuth angle
Ψ	Chromaticity
Π_Ψ	Chromatic plane, Maxwell plane
Λ	Diffuse chromaticity
Λ^{sf}	Diffuse specular free chromaticity
Γ	Specular chromaticity
I^{sf}	Specular free image
I^{est}	Illumination source chromaticity stimation
I^{norm}	Normalized image respect to the illumination
L_d	Diffuse line
L_s	Specular line
L_w	Achromatic line
Π_{dc}	Dichromatic plane

Chapter 2

Reflectance, Color and Segmentation

This chapter provides background ideas and definitions relevant to this Thesis. Section 2.1 refers to illumination, the main factor on computer vision. Section 2.2 discusses surface reflectance. Section 2.3 introduces color and color spaces, discussing in detail the RGB color space, and defining “chromaticity” which is a key concept in this thesis. Section 2.4 introduces a spheric coordinate representation of colors in the RGB color space, providing a new but equivalent definition of “chromaticity”. Section 2.5 discusses “color constancy” both for human vision and computer vision. Section 2.6 discusses reflectance models, focusing on the the Dichromatic Reflection Model (DRM). Section 2.7 recalls from the literature a formal and general definition of image segmentation, gives a short review of current segmentation approaches, and discusses the main segmentation issues. Section 2.8 discuss about the state of the art on image gradient computation.

2.1 Illumination

Illumination is a main component in any vision systems, be it biological or artificial. If the illumination is in the infrared spectrum, few animals could see some things, and artificial systems need sensors designed for this light wavelength interval to be able to detect some things. The same applies to ultraviolet light, red light or any single-color (narrow-band) illuminant. The reference to establish some performance benchmarks for vision systems is the human vision system (HVS), and the typical kind of illumination is the white (wide-band) illumination provided by the Sun. But natural illumination is not constant, it is different from morning to evening, from summer to spring, in sunny days or in cloudy days. Artificial illumination also shows strong changes in artificial environments; shops, pubs, city ways, town streets, industrial environments, etc.

There are many works in the literature which estimate illumination properties in the visible spectrum. Hara [1] proposes a method for illumination source position and reflectance estimation from a single view without the distant illumination assumption. Sato [2] introduces a method for recovering an illumination distribution of a scene from image brightness inside shadows cast by an object of known shape in the scene. Other works are focused only in the estimation of the chromaticity of the illumination [3, 4, 5, 6].

2.2 Surface Reflectance

There are many definitions of “reflectance”, some times conflicting if coming from different sciences: optics, physics, radiometry, astronomy, and recently computer science for visualization. We are interested in it from the point of view of computer vision.

In digital image processing research, we can not ignore the physical effect of the reflectance, because it is our “a priori knowledge”. Unfortunately, the reflectance depends on the illumination and the surface properties, and, therefore, this “a priori knowledge” is generally unknown. In computer vision, we refer to the reflectance phenomenon as the “surface reflectance”.

The measurement of light is a field in itself, known as radiometry. A brief and clear introduction to radiometry is exposed in Forsyth and Ponce [7]. Fig. 2.1[1] shows the basic case of reflectance where a beam of light strikes a surface with an angle ω_1 respect to the normal angle n , and the outgoing beam leaves it with the same magnitude but at different direction ω_2. Here, we can formulate some interesting questions; the outgoing beam has the same energy over all the wavelength range as the incoming beam? The angle between ω_1 and n: is it the same as the angle between n and ω_2? The answer for both questions depends of the surface properties.

Generally some simplifying assumption have been done on the surface nature: radiance leaving a point (irradiance) is due to the radiance arriving

---

[1] http://en.wikipedia.org/wiki/File:BRDF_Diagram.svg

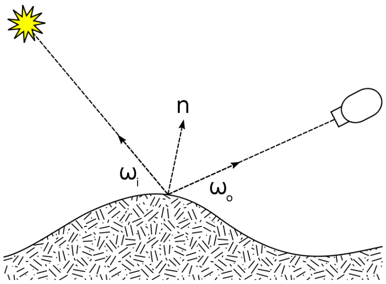

Figure 2.1: Surface reflectance by BRDF

to this point, all light leaving at a wavelength is due to the incoming light to this wavelength (surfaces only can absorb some light at some wavelength) , and fluorescent surfaces are ignored.

Surfaces are classified into two main classes; specular surfaces and diffuse or lambertian surfaces. The specular surfaces (after the Latin word 'speculum', a mirror) have a behavior like a mirror: all incoming radiance leaves the surface without changes (ideally). The diffuse surfaces or lambertian surfaces (after Lamber) have the property to absorb some of the incoming radiance, and the outgoing beam follows the Lambert cosine law [8]. In a diffuse surface we can detect the surface color and textures.

Fig.2.2 helps to understand these kind of refectances. The sketch in Fig. 2.2(a)[2] shows a light beam arriving the surface and interacting inside the matter. The energy of some wavelengths of the light beam are absorbed by the matter. The light beam leaves surface in a undermined direction. The sketch in Fig. 2.2(b)[3] shows the behavior of a lot of light beams striking a surface, then the general reflection can be modeled by the Lambert cosin law. The sketch in Fig. 2.2(c) [4] shows the behavior of a specular surface. In this case, the incoming light beam leaves the surface following the symmetrical geometry respect the normal angle at the strike point.

---

[2] http://en.wikipedia.org/wiki/File:Diffuse_reflection.gif

[3] http://en.wikipedia.org/wiki/File:Reflection_angles.svg

[4] http://en.wikipedia.org/wiki/File:Diffuse_reflection.PNG

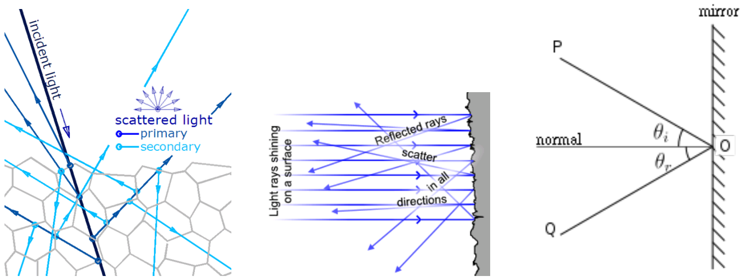

(a) (b) (c)

Figure 2.2: Diffuse and specular reflections

In nature most of the surfaces have a mixture of both reflectances due to the diversity of the surface composition, e.g. human skin could be matte, however grease and sweat can originate highlights, and so on in the common surfaces. Usually surfaces have not single component: Vegetables have a wax layer and light can go trough them. Rocks and stones have different material composition with different reflectance properties. For computer vision and visualization *reflectance models* are used trying to explain the light behavior in different surfaces.

2.3 Color and Color Spaces

Color is an important descriptor for visual object recognition [9], however it is a subjective value, a human perception feature, always under research [10]. Color perception derives from the filtering of the light spectrum by the spectral sensitivities of the light receptors in the retina. Colors may be defined and quantified by the degree of stimulation of these cells. These physical or physiological quantifications of color, however, do not fully explain the psychophysical perception of color appearance. Color categories and physical specifications of color are also associated with objects, materials, light sources, etc., based on their physical properties such as light absorption, reflection, or emission spectra.

Defining a color space, colors can be identified and be quantitatively described by their coordinates. There are two kind of color spaces. First, the "additive color spaces" created by addition of primary colors (Red, Green and Blue) where all colors are represented as a sum of dimensional units: examples are the RGB, sRGB, RGBa, HSV,HSI, HSL, CIE l*a*b, and CIE

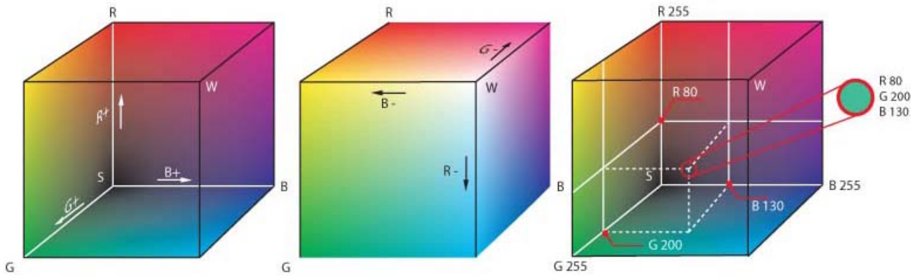

Figure 2.3: Rendering of the RGB color space in the range [0-255]. Left, the view of the boundary color planes intersecting at the black color corresponding to the space origin. Middle, view of the boundary color planes intersecting at the white color. Right, one specific color point and its RGB coordinates.

L*u*v color spaces. Second, the "subtractive color spaces" created by the superposition of secondary color (Cyan, Magenta , Yellow and Black) each absorbing its respective wavelength. These spaces are used in paints, inks and printing systems. The most famous is CMYK . There are also some specific color spaces for specific devices like NTCS for TV sets.

2.3.1 RGB

Most of this thesis work is done on the RGB color space [11]. Fig. 2.3[5] shows the RGB cube in the range [0-255]. In general, RGB is defined on the Natural (discrete) range [0-255] because $2^8 = 256$ and first computers work with 8 bits providing enough quality for the human vision on screens. We are going to work in the Real (continuous) range [0-1] for a better precision. In this color space the three orthogonal lines represent the primary colors (Red, Green and Blue) which give the name to this space. The other three orthogonal lines have the secondary colors (Cyan, Magenta and Yellow). These six lines begin on the origin [0,0,0] and finish on its respective extrema. The achromatic line, corresponding to the gray scale, begins on the black color at the space origin [0,0,0] and finishes on the white corner with coordinates [255,255,255] or [1,1,1], depending on the color space scale chosen.

---

[5] http://upload.wikimedia.org/wikipedia/commons/0/03/RGB_farbwuerfel.jpg

$$Color \begin{cases} Chromaticity & \begin{cases} Hue \\ Saturation \end{cases} \\ \\ Intensity \end{cases}$$

Figure 2.4: Decomposition of color concepts

2.3.2 Chromaticity

Color is decomposed into Chromaticity and Intensity. Chromaticity refers to the quality color information regardless of the intensity. Intensity relates to the energy, the amount of photons received by unit surface. In the HSI family of color spaces, chromaticity is defined by the pair (H, S) of Hue and Saturation. Hue relates to the difference between colors, corresponding to the perceived wavelength class, e.g. measures the difference between red and blue. Saturation one represents the relative mixture with white. These ideas are drawn on the schema of Fig.2.4. If we interpret color on RGB like vectors, previous ideas can be explained as follow: Intensity is the vector magnitude, Saturation is the orthogonal distance to the achromatic line, and Hue is the rotational distance around the achromatic line to the Red corner.

In RGB Chromaticity corresponds to the normalized RGB values $r = \frac{R}{R+G+B}$, $g = \frac{G}{R+G+B}$ and $b = \frac{B}{R+G+B}$, so that $r + g + b = 1$. Therefore, one of the normalized coordinates is redundant and can be discarded. Usually, the pair (r, g) is used as the chromaticity. The effect of computing the normalized RGB values is that all color pixels are projected into the Maxwell triangle [12], shown in Fig. 2.5. This triangle is the region of the plane defined by the points $\{(1,0,0), (0,1,0), (0,0,1)\}$ lying inside the RGB cube. We will name this plane chromatic plane, denoting it by Π_Ψ.

2.4 Spherical Coordinates

RGB is most used color space in computer vision, despite its lack of perceptual continuity. Without changing the color space, we can obtain a quite different representation of the color information by using an equivalent system of coordinates to specify the location of the color in the RGB color space. In this Thesis we have used extensively this alternative representation. Denote $c = \{R_c, G_c, B_c\}$ the point in the RGB color space corresponding to an image

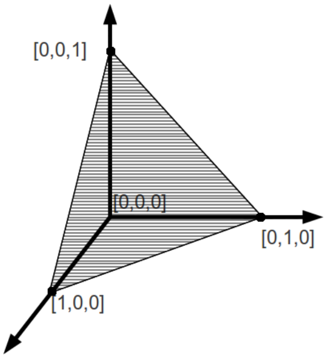

Figure 2.5: Maxwell triangle

pixel's color. The vector going from the origin up to this point, shown in Fig. 2.6, can be represented using spherical coordinates $c = \{\theta_c, \phi_c, l_c\}$, where θ is zenithal angle, ϕ is the azimuthal angle and l is the vector's magnitude.

As said before, in the RGB color space, chromaticity Ψ_c of a color point is represented by its normalized coordinates $r_c = \frac{R_c}{R_c+G_c+B_c}$, $g_c = \frac{G_c}{R_c+G_c+B_c}$, $b_c = \frac{B_c}{R_c+G_c+B_c}$, such that $r_c + g_c + b_c = 1$. Therefore, chromaticity corresponds to the projection onto the chromatic plane Π_Ψ of Fig. 2.5 , along the line defined as $L_c = \{y = k \cdot \Psi_c; k \in \mathbb{R}\}$. In other words, all the points in line L_c have the same chromaticity Ψ_c, which is a 2D representation equivalent to one provided by the zenithal and azimuthal angle components of the spherical coordinate representation of the a color point. Given an image $\mathbf{I}(x) = \{(R, G, B)_x ; x \in \mathbb{N}^2\}$, where x refers to the pixel coordinates in the image grid domain, we denote the corresponding spherical representation as $\mathbf{P}(x) = \{(\phi, \theta, l)_x; x \in \mathbb{N}^2\}$, which allows us to use $(\phi, \theta)_x$ as the chromaticity representation of the pixel's color.

2.5 Color Constancy

Color Constancy (CC) is the mental ability to identify chromatically equivalent homogeneous surfaces under illumination changes [13, 14]. This mental ability is still an open neupsicological research topic [10]. The CC property is complementary to the ability to detect the color discontinuity represented by

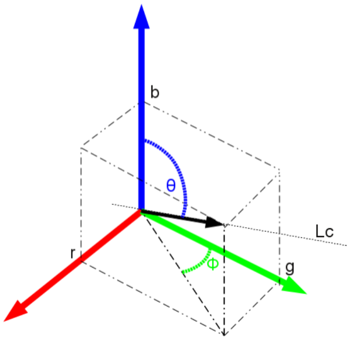

Figure 2.6: The vector corresponding to a color point in the RGB space

the chromatic edges (CE) under illumination changes. CC, Relational Color Constancy and CE can be viewed as different and complementary aspects under the neurological and retinal activity [15]. Measurements on human subjects lead to the conclusion that retinal processing is not enough to extract chromatic features and chromatic based structural image information. Some works demonstrate that CC analysis is done in the visual cortex, in the areas V4 and V4A [13]. Assuming the analogy with the human vision biology, artificial vision systems need no trivial processing to ensure CC results on the processing real images. Dark scenes are critical for CC, because dark image regions are usually very noisy, that is, the signal to noise ratio is very high due to the low magnitude of the visual signal. In these regions, the ubiquitous thermodynamical noise has an amplified effect that distorts region and edge detection ensuring CC conditions.

In computer vision, CC refers to the automatic removal of the illumination effects. There are two main approaches to deal with it. On the one hand, by specific image filtering, such as the algorithm proposed by Spitzer [16] based on local and remote retinal adaptation mechanisms (gain control). Geusebroek [17] proposes a physics-based method, valid for Lambertian reflectance, considering spatial and spectral derivatives of the image formation model to derive object reflectance properties independently of the spectral energy distribution of the illuminant. On the other hand, estimating the illuminant chromaticity, normalizing afterwards the image relative to the illumination chromaticity, so that the transformed image illumination would be pure white color. Yoon [18] uses the $r - g$ chromaticity looking for the chromatic lines, R. Tan [4] proposed a method using the inverse intensity space and the Hough transform. Most of these methods are grounded on DRM [19]. Other approaches try to obtain segmentation procedures which are inherently robust to illumination effects [20, 21].

2.6 Reflectance Models

A reflectance model is a mathematical model which try to explain the surface reflection of a specific kind of materials under a specific kind of illumination. Still, we haven't got an universal reflection model that explains the reflection of light on any surface. Therefore there are a lot of reflectance models trying to explain the reflectance phenomenon. Mainly we can group them in the following categories:

- Models used for image processing (photo retouching and color restoring, they are inspired in human vision)
- Models used for visualization (games, virtual reality and synthetic images)
- Models used for computer vision (we want to extract information about the scene from the images)

The first category encompasses reflectance models inspired in the human (or mammalian) perception, based in the more recent bio-medical discoveries about vision from the neural and ophthalmological points of view, focused on retina response and visual cortex function understanding. The most used model of this category is *Retinex* [22, 23] which is directly inspired in the human vision, specifically in the function of rods and cones retinal cells. It is used mainly for color image restoration, but it is too sensitive to changes in the color of nearby objects to serve as an adequate model of color constancy in the human vision system [24]. Recently, new models have been proposed, such as the *Neuromorphic* model introduced by Hong and Grossberg [25].

The second category is composed of the reflectance models used for visualization, that is for the generation of synthetic digital images. The most used model is the *Bidirectional Reflection Distribution Function (BRDF)* [26] which expresses the ratio between the irradiance and surface radiance depending of the point of view and direction of the illumination. As an improvement of this model Torrance & Sparrow [27] add a pseudo-spheric globe on the specular component. A further improvement of both models have been proposed by Ragheb and Edwin [28] allowing the simulation of a wax (or glass) layer over surfaces. The *Bidirectional Texture Functions (BTF)* are used to simulate textures [29, 30] allowing to synthesize images of objects showing diffuse and specular reflections. However, these models are not enough to simulate all surfaces, e.g. human vision system is very exact discriminating the human skin. No one of the previous models are adequate to simulate images of human faces. *Bidirectional Surface Scattering Distribution Function (BSSRDF)* [31] allows the simulation of light behavior through epidermis. A well parametrized BSSRDF function has been introduced by Jensen & Donner[32] which can simulate all kinds of human skins.

The third category includes reflectance models that can be applied in computer vision. These models are grounded in physical models, allowing the use of real measurements for model calibration, etc. The first and most widely used model is *BRDF* [33, 34]. By observing a homogeneous surface, we can measure the BRDF reflection parameters using a scatterometer [35], even in the infrared [36]. Another important reflection model in this category is the *Dichromatic Reflection Model* (DRM) introduced by Shafer [37]. It has been widely used to separate diffuse and specular components, and for the estimation of the illuminant chromaticity. An evolution of this model is the DRM under bi-illuminant conditions [38]. This model tries to help understanding illumination changes in chromatic edges.

2.6.1 DRM

We can formulate digital image taken with a camera is defined on DRM as:

$$I(x) = w_d(x) \int\limits_{\Omega} S(\lambda, x) E(\lambda) q(\lambda) d\lambda + w_s(x) \int\limits_{\Omega} E(\lambda) q(\lambda) d\lambda \tag{2.1}$$

where:

- $I = \{I_r, I_g, I_b\}$ is the color of an image pixel obtained through a camera sensor.
- x is the two dimensional coordinate vector of the pixel site in the image domain.
- $q = \{q_r, q_g, q_b\}$ is the three element vector of sensor sensitivity at the red, green and blue spectral bands.

- $w_d(x)$ and $w_s(x)$ are the weighting factors for diffuse and specular components, respectively. They depend on the geometric structure of the scene corresponding to the pixel at location x.
- $S(\lambda, x)$ is the diffuse spectral reflectance.
- $E(\lambda)$is the illumination spectral power distribution function, which is independent of the pixel spatial location x assuming an uniform illumination color.
- The integral is computed over the entire light visible spectrum Ω.

In reduced form, Eq. (2.1) becomes the Dichromatic Reflection Model (DRM) introduced by Shafer [37]. It explains the perceived color intensity $I \in \mathbb{R}^3$ of each pixel in the image as the addition of two components, one diffuse component $D \in \mathbb{R}^3$ and a specular component $S \in \mathbb{R}^3$. The diffuse component refers to the chromatic properties of the observed surface, while the specular component refers to the illumination color. The mathematical expression of the model, when we have only one surface color in the scene, is as follows:

$$\mathbf{I}(x) = m_d(x)\mathbf{D} + m_s(x)\mathbf{S}, \tag{2.2}$$

where m_d and m_s are weighting values for the diffuse and specular components. Equivalently, Eq.(7.1) can be expressed in spherical coordinates as:

$$\mathbf{I}(x) = (\theta_{\mathbf{D}}, \phi_{\mathbf{D}}, l_{\mathbf{D}}(x)) + (\theta_{\mathbf{S}}, \phi_{\mathbf{S}}, l_{\mathbf{S}}(x)),$$

where $\mathbf{\Lambda} = (\theta_{\mathbf{D}}, \phi_{\mathbf{D}})$ is the diffuse chromaticity,

$$l_{\mathbf{D}}(x) = \sqrt{(m_d(x)\mathbf{D}_R)^2 + (m_d(x)\mathbf{D}_G)^2 + (m_d(x)\mathbf{D}_B)^2},$$

and $\mathbf{\Gamma} = (\theta_{\mathbf{S}}, \phi_{\mathbf{S}})$ is the specular chromaticity and

$$l_{\mathbf{S}}(x) = \sqrt{(m_s(x)\mathbf{S}_R)^2 + (m_s(x)\mathbf{S}_G)^2 + (m_s(x)\mathbf{S}_B)^2}.$$

For a scene with several surface colors, the DRM equation must assume that the diffuse component may vary spatially, while the specular component is constant across the image domain:

$$\mathbf{I}(x) = m_d(x)\mathbf{D}(x) + m_s(x)\mathbf{S}, \tag{2.3}$$

which is expressed in spherical coordinates as:

$$\mathbf{I}(x) = (\theta_{\mathbf{D}}(\mathbf{x}), \phi_{\mathbf{D}}(\mathbf{x}), l_{\mathbf{D}}(x)) + (\theta_{\mathbf{S}}, \phi_{\mathbf{S}}, l_{\mathbf{S}}(x)), \tag{2.4}$$

where $\mathbf{\Lambda}(x) = (\theta_{\mathbf{D}}(x), \phi_{\mathbf{D}}(x))$, and

$$l_{\mathbf{D}}(x) = \sqrt{(m_d(x)\mathbf{D}_R(x))^2 + (m_d(x)\mathbf{D}_G(x))^2 + (m_d(x)\mathbf{D}_B(x))^2},$$

and $\mathbf{\Gamma} = (\theta_{\mathbf{S}}, \phi_{\mathbf{S}})$ and

$$l_{\mathbf{S}}(x) = \sqrt{(m_s(x)\mathbf{S}_R(x))^2 + (m_s(x)\mathbf{S}_G(x))^2 + (m_s(x)\mathbf{S}_B(x))^2}.$$

In Eq. (2.4) the chromaticity of the specular component $\theta_{\mathbf{S}}, \phi_{\mathbf{S}}$ is space invariant, meaning that the illuminant source chromaticity is the same for all the illuminants. This is the most common situation in practice, where we have one colored illumination source irradiating over a scene with objects of different colors.

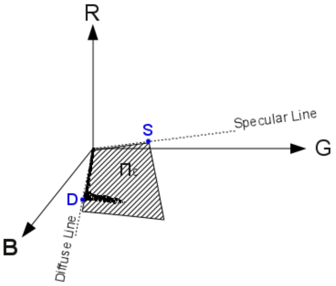

Figure 2.7: Dichromatic reflection model

The RGB color space has some advantages versus the HSI family of color spaces when working with DRM. First, the DRM is defined as a linear combination in an Euclidean space. The hue component of the color representation in the HSI color family is an angle, corresponding to a value in a non-Euclidean subspace. Consider the image in Fig.2.8(c) and the distribution of its pixels in the color space. In Fig. 2.8(a) we can see the distribution of the pixels in the HSV color space. On the one hand pixels with low intensity value are very separated from each other. When intensity increases pixel

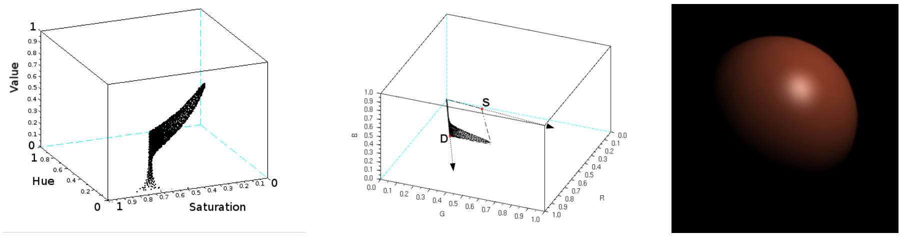

(a) (b) (c)

Figure 2.8: Distribution of the pixel colors of the ball image in the HSV color space (a) and in the RGB color space (b)

colors fall in a line (the chromatic line) in the HSV color space. On the other hand specular pixels are placed in a curved, horn-like shape. Comparing with Fig. 2.8(b) the linearity is lost, hence the difficulty to formulate DRM in HSV parameters.

2.6.2 Geometry in RGB induced by the DRM

From the DRM we can deduce some interesting features of the distribution of the pixels in the RGB cube. In Fig. 2.9 we illustrate the main expected effects for a single color image (disregarding the black background) with a bright spot due to the illumination source. According to DRM we need to know only two colors: D corresponding to the observed surface and S corresponding to the illumination source. Drawing a line in the RGB cube passing over these colors and the RGB origin (black), we obtain two chromatic lines L_d and L_s, respectively. These two lines define a chromatic plane in RGB illustrated as the stripped region in Fig. 2.9a. All the image pixels must fall in this plane, discounting additive Gaussian noise perturbations, according to DRM equation 7.1 for image colors D and S. Looking to the image pixel distribution inside the chromatic plane, we obtain the plot in Fig. 2.9b, whose axes are the chromatic lines L_d and L_s. We have that non-specular pixels fall close to the diffuse line L_d, while specular pixels go away from the origin and the diffuse line parallel to the specular line L_s. There is an intensity threshold for the pixels having a significative specular component ($m_s(x) >> 0$). This threshold is the albedo of the material in the scene.

For intensities greater than the albedo, pixels fall away from the L_d diffuse line along the direction of L_s.

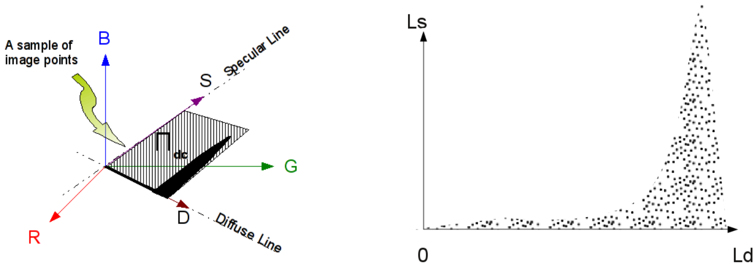

(a) (b)

Figure 2.9: Expected distribution of the pixels in the RGB cube according to DRM for a single color image.

When there are more than one color in the image, we can expect several diffuse lines, so that the we can base our image segmentation on this observation. All these lines cross the RGB origin, therefore the pixel polar coordinates of diffuse pixels contain much information relative to underlying reflectance regions. For an scene with several surface colors, the DRM equation assumes that the diffuse component may vary spatially: $I(x) = m_d(x)D(x) + m_s(x)S$. However, the specular component is space invariant in both cases, because the illumination is constant for all the scene. Finally, assuming several illumination colors we have the most general DRM $I(x) = m_d(x)D(x) + m_s(x)S(x)$ where the surface and illumination chromaticity are space variant.

2.6.3 Angular chromatic distance

For diffuse pixels having a small specular weight $m_s(x)$, of the image expressed on the DRM, the zenith ϕ and azimuthal θ angles are almost constant, while they are changing for specular pixels, and dramatically changing among diffuse pixels belonging to different color regions. Therefore, the angle between the vectors representing two neighboring pixels $\mathbf{I}(x_p)$ and $\mathbf{I}(x_q)$, denoted $\angle(I_p, I_q)$, reflects the chromatic variation among them. For two pixels in the same chromatic regions, this angle must be $\angle(I_p, I_q) = 0$ because they will be collinear in RGB space. The angle between I_p, I_q is calculated according to the equation:

$$\angle(I_p, I_q) = \arccos\left(\frac{\mathbf{I}\left(x_p\right)^T \mathbf{I}\left(x_q\right)}{\sqrt{\left\|\mathbf{I}\left(x_p\right)\right\|^2 + \left\|\mathbf{I}\left(x_q\right)\right\|^2}}\right). \tag{2.5}$$

2.7 Image Segmentation

Image segmentation is among the foremost topics in image processing and in computer vision. It is the first step in most computer vision system pipelines, so that the whole system performance may be heavily dependent on the segmentation results. Popular instances of segmentation methods for color images proposed in the literature are based on watershed transform [39, 40, 41, 42, 43], and on clustering procedures [44, 45, 46, 47]. Unfortunately previous gradient detectors are not enough for color image segmentation, because there not exists an universally accepted color gradient definition.

The image segmentation process defines a partition of the image domain F according to some pixel property [48, 49]: If $P\left(x\right)$ is some homogeneity predicate defined on groups of connected pixels, then the image segmentation is a partition of the set F into connected regions $\left(S_1, S_2, ..., S_n\right)$ such that $\bigcup_{i=1}^{n} S_i = F$ with $\forall i \neq j, S_i \cap S_j = \varnothing$, and each pixel in a region fulfills the same property, i.e. $\forall x, y \in S_i; P\left(x\right) = P\left(y\right)$.

2.7.1 Current segmentation approaches

Image segmentation can be carried out in two different ways. First, *pixel based* segmentation performs clustering in the color space. In this approach, the pixels corresponding to a color cluster may be aggregated into several disconnected regions in the image domain. Second, *region based* segmentation takes into account the pixel neighborhood, working in the image domain.

In color images, a straightforward *pixel based* segmentation may be done using the classical k-means algorithm [47, 50]. There are three major difficulties in this approach: (1) determining the optimal number of clusters to be created, (2) choosing the initial cluster centroids, and (3) handling color distributions characterized by arbitrary cluster shape, cluster density, and the number of points in different clusters. Dae-Won [50] proposes an automatic initialization of the fuzzy c-means for color clustering. More recently, the same idea has been applied on hyperspectral images [47], where the pixel feature vector is defined by its spectral signature. In both cases, the shortcoming is the dependence on the color space, spectral signature for hyperspectral images or the strategy for dimensional reduction. This drawback comes from the distance used in the fuzzy c-means, usually the euclidean distance. In this way, Oussalah[51] uses a divergence distance, which builds a bridge to the notion of probabilistic distance. A good idea for image segmentation, is to take into account a pixel distance and the neighborhood, such as [52] where for clustering uses c-means and for the neighborhood Random Markov Fields.

Mathematical morphology (MM) is a *region based* segmentation methods grounded in the Lattice Theory [53, 54, 55]. First introduced as a shape based tool for binary images, MM has become a powerful non-linear image analysis technique with operators for image segmentation, image filtering, and feature extraction in binary or gray-scale images. The definition of morphological operators is based in a totally ordered set that is a complete lattice structure: for any two elements in a lattice, we can determine if they are equal or one is bigger than the other one. The extension to color spaces of the results from grayscale morphology are not trivial, and highly dependent on the definition of a suitable distance and the appropriate selection of the color space. Hanbury [56, 57, 58] presents MM operators on the CIElab and HSL color spaces, introducing the IHSL color space. Angulo [59] applies this technics extracting information from cartographic images.

Watershed transformation algorithm is a MM method, therefore it is a *region based* segmentation method. It was introduced by Beucher [43] three decades ago. This algorithm has a topological inspiration, interpreting a gray-scale image as a topological function that gives the elevation at each point in the image domain [43, 42, 41]. The watershed transformation performs a flooding process where each region is a catchment basin. The reference gray-scale image for segmentation is the gradient image, therefore, the basins correspond to smooth regions between edges regardless of image intensity. The original algorithm has been improved in the literature based on the construction of the gradient image. Wang [60] proposes a multiescale morphological gradient, avoiding over-segmentation by the detection of isolated local minima. To avoid over-segmentation, "region merging" processes can be applied. Dagher [61] presents Waterballoons which are a mixture of "balloon snakes" and watershed. On each local minimum of the gradient image an active contour is initialized, so that the flooding process is replaced by snake-surface growing. This strategy avoids isolated small regions, such as points, which can be assumed as a noise consequence. Other improvements of the standard watershed are focused on the speed-up. An original idea is to apply a raining simulation instead of the flooding process [39] to find faster the image edges. Other approaches reduce the computational cost optimizing the algorithm in the neighborhood looking for shorter paths [40, 42].

A difficult task is the evaluation of the segmentation method. Each person has different perception of segmentation quality. Different applications may perform better using different segmentations, therefore the criteria of a good segmentation are often application-dependent. A review of measures for the validation of segmentation process in [62] lacks measures for color images and multi or hyperspectral images.

Segmentation can be stated as a supervised learning process. A handicap for the validation of segmentation methods is that usually the ground truth is unknown, or we have scarce information about it. Therefore it may be difficult or impossible to to measure the classification error. For example, in earth observation when the location of agricultural crops is known, we can apply supervised segmentation. When ground truth knowledge is expensive it is possible to apply 'active learning'. In active learning the user provides incrementally the training samples that lead to the greatest improvement of the classifier. We can see an example for RGB images in Fiji[6] and a plugin for image segmentation named 'Advanced Weka Segmentation'[7].

2.7.2 Main segmentation issues

There are four main sources of problems in image segmentation: illumination, noise, edge ambiguity and computational cost. In this section we discuss those topics, offering some ideas about how we have addressed these problems when developing our segmentation algorithm along the Thesis.

Illumination in real environments: both real and artificial illumination sources introduce some important problems in image understanding. Because of highlights or shadows, both depending on the illuminant position, a surface of a scene can produce a lot of different image perceptions. In digital image processing, it is very usual to assume a uniform chromatic illumination because it makes easier to deal with the problems derived from

---

[6] http://fiji.sc/wiki/index.php/Fiji

[7] http://fiji.sc/wiki/index.php/Advanced_Weka_Segmentation

the illumination. Our approach works on a chromatic representation derived from a spherical coordinate interpretation of the RGB color space which is rather insensitive to achromatic variations in the image pixel colors. That means that we avoid highlights introducing falsely detected regions. Dark image regions, such as object shadows, are characterized by the fact that small pixel color perturbations introduce strong chromatic shifts. Therefore, the chromatic representation is useless in these regions. We will try to imitate the human vision system (HVS), shifting our computation of pixel distance from color to grayscale representation in dark regions.

Noise: there are two main sources of image noise, introduced, on one hand, by thermal noise of the camera and robot motion, and, on the other hand, by lossy compression algorithms. The chromatic representation is rather insensitive to additive noise in high intensity regions. However, it is very sensitive to it in dark image regions. We look for robust segmentation processes in all cases.

Edge ambiguity: The proposed segmentation algorithm is region-oriented, therefore edge detection is obtained indirectly as the boundaries between detected regions. An edge appears where two neighboring pixels have different properties. Therefore, any edge detector is always based on the definition of a distance between pixel properties. If this distance is bigger than a given threshold, we can declare that there is an edge between the pixels, otherwise they belong to the same region. A chromatic representation helps to avoid spurious edge detection due to highlights. Usually, color transition around highlights is smooth while in true boundaries between surfaces the chromatic information changes dramatically.

Computing time: Most image segmentation methods are not designed with real time applications in mind, therefore they have high computational costs. However, for some applications like robotics, computing time is critical because these applications have to run in real time. Our algorithm performs only one-pass over the image, processing each pixel only once. The order of pixel processing is row-wise therefore we use the 4-WN neighborhood for pixel processing. We look for algorithm implementations that may obtain real-time performance on off-the-shelf personal computers for small images.

2.8 Image Gradient Computation

The detection of edges provides a way to find shapes in images, because they give knowledge about the localization of object boundaries. Edge detection is the dual process to region segmentation, we can identify an image region by drawing the edges surrounding it. An image edge is a line whose neighboring pixels have a significant gray level variation among them. Isolated points with strong differences in their neighborhood are sometimes referred as *edgels*.

Edge detection is based on the examination of the image spatial derivatives at each point in the image domain. The gradient magnitude and orientation give the edge magnitude and direction. Another well-known second-order derivative method for edge detection is the Laplacian operator, given the addition of the second derivatives in all directions; therefore, it is an isotropic edge detector. These tools may be combined, for instance using the magnitude of the gradient vector as edge detector and the sign of the Laplacian to determine if the edge pixel belongs to the dark or the light side of the border.

Well-known methods based on he first derivative are the Sobel [63] and Prewitt [64] convolution operators. Sobel and Prewitt apply a threshold on the gradient magnitude to decide whether a point is a edge or not. The Canny [65] edge detection approach avoids edgels, therefore all line edges are connected. Canny's algorithm uses the direction of the gradient vector to find the nearest edge point, so that the output is compound by convex regions, whereas Sobel and Prewitt approached follows the mathematical definition of gradient but these ones not use the gradient direction. Roberts operator [66] was one of the first contributions on edge detection, it marks only the edge points without their direction. This operator is fast and has good results when working with binary images. Kirsch masks [67] also known as 'compass' because they are defined by using a simple mask and rotating in the eight main directions (North, Northwest, West, Southwest, South, Southeast, East and Northeast). Robinson masks [68] follow the same compass idea but in this case by using one of the Sobel masks. These aforegoing methods are performed in the eight neighborhood but they could be extended easily to a bigger neighborhood.

It is significantly more difficult to analyze edges in multichannel images (color images, multi-spectral and hyper-spectral images) [69]. A straightforward approach to edge detection on his kind of images is to compute the gradient vector on each channel and obtain an spectral gradient by linear combination of the single-channel gradients. However, each channel has different information of the image, so that the single-channel gradients at a point may have conflicting information, for instance, the sum of all channels gradient direction could be 0 though the single-channel gradients are non null. To overcome this shortcoming, the following expression can be used $S = J^T J$, where J is the Jacobian matrix and S is a diagonal matrix. If only one member of S is non-zero, then is is called a perfect edge and it gives de direction of the variation. However, usually this diagonal matrix has more non-zero members, as a consequence of image noise. The trace of S is a measure of the edge strength.

Nowadays, edge detection remains an active research topic. For example Ségonne[70] presents a novel framework to exert topology control over a level set evolution. It is an active contour which works in a three dimensional space and have excellent results in medical image segmentation. Respect to the evolution of the traditional gradient based methods, McIlhagga [71] discuss about Canny's work. He improves it solving two problems. First, he provides a more accurate localization criterion, and second, the width of the optimal detector is limited by considering the effect of the neighboring edges in the image.

Chapter 3

Component Separation

The works in this chapter have in common the use of the DRM to postulate different techniques addressing related problems of image correction. First, we consider the problem of illumination source chromaticity (ISC) estimation for chromatic normalization of the image [3] based on the spherical coordinate representation. The chromatic normalization can be a preprocessing for the remaining processes dealt with in this chapter. Second, we deal with the problem of estimation of a regularized illumination field over all the image [72] which can be applied to perform illumination intensity correction previous to segmentation. Third, we propose a bayesian approach for image component separation [73]. Fourth and final contribution is the proposition of a geometrical approach in the RGB color space for component separation [74].

This chapter's outline is as follows: Section 3.1 presents a review of the state of the art on illumination correction. Section 3.2 describes a method for illumination source chromaticity estimation on RGB spherical coordinate representation. Section 3.3 proposes a method to reduce the highlights using an evolutionary algorithm. Section 3.4.2 shows a Bayesian approach. Section 3.5 describes a geometrical method for separation of diffuse and specular component. Section 3.6 gives the conclusions of our works on illumination correction.

3.1 State of the Art

Following the Dichromatic Reflectance Model (DRM) the information about the illumination source is contained in the specular component of the image, hence the detection and separation of the diffuse and specular components of the image is required for illumination correction methods. Besides bright spots and highlights are considered as a kind of image noise for some applications. The detection of the specular image component solves two problems. On the one hand, the specular component of an image depends also on the geometrical properties of the image, so this information may be used too for 'shape from shading' 3D data reconstruction from images [75, 76, 77]. On the other hand, we can remove the specular component from the original image obtaining a diffuse image giving an estimation of the true chromatic surface properties. Specular reflection reduction by using a multi-flash mechanism is reported in [78] . The main drawback of this method is that it requires a complex hardware setup to obtain many images taken with synchronized flash devices. Other advance technics use only an image giving a reflectance estimation [1].

The estimation of the illumination source chromaticity (ISC) [79] is a necessary step for color image normalization which is a critical step for constant color perception either in biological human perception [13, 10] or in the design of robust artificial vision systems [80]. Highlights correspond to image pixels with a high specular component. Therefore, if an image does not have a bright area were the specular component is strong relative to adjacent image regions, it is not possible to make ISC estimation by any means. Color normalization to a reference ISC, usually white, allows the robust estimation of reflectance components, and subsequent segmentation of the image. Most ISC estimation algorithms [81, 79] work on the normalized RGB color space ($r + g + b = 1$). Methods grounded [5, 6, 4] in the DRM only need one image. Kuk-jin method [5] takes profit of the DRM and uses chromatic lines estimation by local ratios. Roby Tan method [4, 82] uses the inverse intensity space and by the Hough transform can estimate the illumination chromaticity. Ebner [6] estimates the illuminant chromaticity by segmentation and filtering looking for dichromatic lines performing a linear regression on the x- and y-coordinates in CIE XYZ chromaticity space.

Separation of diffuse and specular image components is another hot topic [20, 74, 83, 84, 85, 86]. Mallick [20] presents a photometric stereo method for non-diffuse materials that does not require an explicit reflectance model or reference object. By computing a data-dependent rotation of RGB color space, the specular reflection effects can be separated from the approximately Lambertian diffuse reflection effects in surfaces that can be modeled with dichromatic reflectance. Hui-Liang [83] proposes a method to separate reflections in a color image based on the chromaticity error analysis and appropriate selection of body color for each pixel. By solving the least-squares problem of the dichromatic reflection model, reflection separation is implemented on a single pixel level, without requiring image segmentation and even local interactions between neighboring pixels. R. Tan method [84] is based solely on chromaticity, without requiring any geometrical information. One of the basic ideas is to iteratively compare the intensity logarithmic differentiation of an input image and its specular-free image. Umeyama [85] shows a method where diffuse and specular components of surface reflection can be separated as two independent components applying Independent Component Analysis to the images observed through a polarizer of different orientations. Kuk-jin method [87] proposes a specular-free two-band image that is a specularity-invariant color image representation, so that reflection components separation is achieved by comparing local ratios at each pixel and making those ratios equal in an iterative framework. Recent solutions [88, 75] require uniform illumination and the identification of constant color regions, working on synthetic “clean” images.

3.1.1 Motivation

An application framework for the contributions in this chapter is the work on the design of multirobot systems for highly unstructured environments, such as shipyards, where a potentially critical role is that of observer or monitoring, corresponding to a member of the team located in a position where it can monitor all the environment and serve this information to the remaining members of the team. This robot will be static once it has reached the surveillance position, so that images will be relatively static also. That means that illumination conditions will vary slowly and it is possible to perform illumination estimation and correction under real time constraints. The Fig. 3.1 shows two views of a ship hold that illustrate the point of view of the images used in the experiments reported below. Naturally, the kind of images obtained contain a lot of speculaties, because of the presence of water and metal surfaces.

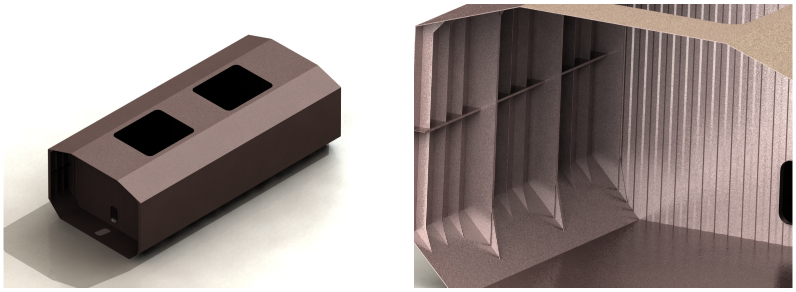

Figure 3.1: Synthetic images of a ship hold. The images used in the experiments were taken from the upper aperture of the hold.

3.1.2 Specular-Free Image

Computation of the specular free image is critical for the detection of the reflectance component. An specular free image, is a geometrical transformation of a image such, the returned image hasn't got specular component: $m_s(x) = 0$. We use the Specular-Free Two-Band method proposed by [5]. The process consists in subtracting to each pixel color bands the value of its minimum band. The image is geometrically identical to the original .

3.2 Illumination Source Chromaticity Estimation

In this section we propose a novel method that uses spherical coordinates in the RGB color space for ISC estimation. We test our method on synthetic images whose ISC is known. This allows a quantitative comparison with a state of the art algorithm, showing that the proposed algorithm improves over the competing algorithm. This method does not need any previous image segmentation and its computational complexity is linear in the number of pixels, therefore it is suitable for real time.

3.2.1 Method

The proposed ISC estimation method is illustrated in Fig. 3.2. The objects in the Fig. 3.2(a) are labeled as (1), (2) and (3). These object labels are used in Fig. 3.2(b),(c) and (d) for easy tracking the results of each step of the algorithm in each of the figures. The process' first step is the detection

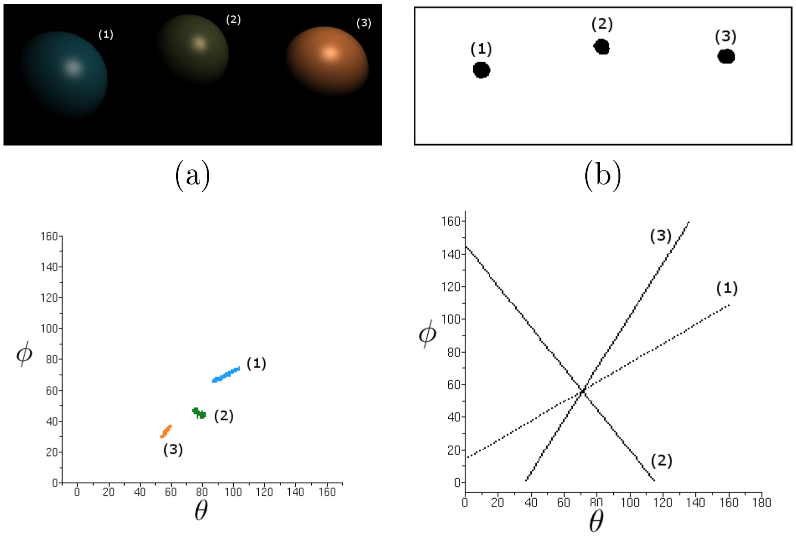

(a) (b)

(c) (d)

Figure 3.2: (a) Original Synthetic Image, (b) Specular regions detected in the original image, (c) distribution of spherical coordinates of specular pixels, (d) linear regressions of each specular region and ISC detected as their intersection.

of the specular pixels in the image. Second, we extract the ISC information from the spherical coordinates of the pure specular pixels, according to the DRM.

The detection of specular pixels is performed as follows [89]:

1. Compute the specular free image, i.e. using the method in [5].
2. Compute the pixelwise difference between the specular free and original image intensities,
3. Detect specular pixels setting a threshold on this difference image.

The specular regions identified in Fig. 3.2(a) are shown in Fig. 3.2(b) as black colored connected components (blobs).

The second step of ISC estimation is to compute the spherical coordinates in RGB space of the specular pixels' color. We construct a 2D representation using the Zenith and Azimuth angle values. In this representation, specular regions correspond to elongated shapes due to the transition between the pure ISC to the surface color that occurs in those regions. Fig. 3.2(c) shows the Zenith-Azimuth representation corresponding to the pixels in the specular regions identified in Fig. 3.2(b). For each connected specular region we compute independently a linear regression. Fig. 3.2(d) shows the regression lines computed for the region corresponding regions in Fig. 3.2(c). The intersection between those lines corresponds to the estimation of the ISC's spherical coordinates of the illuminant: $\theta_{\mathbf{S}}, \phi_{\mathbf{S}}$.

To obtain the corresponding ISC's normalized RGB coordinates, Ψ_{ISC} we compute the intersection of the line determined by $\theta_{\mathbf{S}}, \phi_{\mathbf{S}}$ with the chromatic plane Π_{Ψ}. To perform the image color normalization to the pure white illuminant, it suffices to compute the differences between the Zenith and Azimuth of the white color and the estimated ISC: $\triangle\theta_{\mathbf{S}} = \theta_{\mathbf{S}} - \frac{\pi}{\mathbf{4}}$ and $\triangle\phi_{\mathbf{S}} = \phi_{\mathbf{S}} - \frac{\pi}{\mathbf{4}}$. Applying this correction to the spherical coordinates of the pixels in the image we obtain the image colors under a pure white ISC. A Scilab implementation of the algorithm is available at http://www.ehu.es/ccwintco/index.php/GIC-source-code-free-libre.

3.2.2 Experimental results

We apply the proposed approach and Tan's method [4] to synthetic images generated rendering a known surface under a known ISC. Therefore, we can compute the squared error of the estimations given by the algorithms to achieve a quantitative comparison of both approaches. Fig. 3.2(a) shows an instance of the synthetic test images.

The experimental images have been generated as follows:

1. We select three ISC values (left column in Table 3.1) as the means of the Gaussian distribution of ISC, with standard deviation $\sigma = 0.05$.
2. We generate 30 samples of these ISC Gaussian distributions
3. We generate the synthetic images using a common reflectance image
4. We apply both our approach and the competing method to estimate the ISC from the synthetic images.
5. Finally, we compute the estimation error for each image and give separate mean estimation errors for each separate Gaussian distribution.

	Proposed Method		R. Tan Method	
Ψ_{ISC}	$\widetilde{\Psi}_{ISC}$	$\bar{e}$	$\widetilde{\Psi}_{ISC}$	$\bar{e}$
$r = .28$	$r = .2684$	.010790	$r = .2664$	.052410
$g = .32$	$g = .3102$		$g = .3403$	
$b = .40$	$b = .4212$		$b = .3733$	
$r = .32$	$r = .3301$	.006410	$r = .3232$	.052410
$g = .40$	$g = .4061$		$g = .4118$	
$b = .38$	$b = .2637$		$b = .2627$	
$r = .40$	$r = .3824$	.005964	$r = .4062$	.008008
$g = .32$	$g = .3246$		$g = .3321$	
$b = 28$	$b = .2929$		$b = .2595$	

Table 3.1: Experimental ISC, estimated vales of the normalized RGB and the estimation errors.

The error is computed as the angle between the true and the estimated ISC divided by the maximum possible error $\frac{\pi}{2}$. Table 3.1 contains the average ISC estimation $\widetilde{\Psi}_{ISC}$ and the mean error $\bar{e}$ for each method. It can be appreciated that our approach improves always over Tan's method.

3.3 Evolutive Parametric Approach

Assuming the DRM, we propose here a global correction of specularity effects by means of parametric illumination gradient images obtained by fitting 2D Legendre polynomials to the specular component of the images by a tailored Evolution Strategy (ES). Legendre polynomials have applied successfully to intensity inhomogeneity correction in Magnetic Resonance Imaging [90], as a parametric model of the inhomogeneity field that can be estimated by an energy minimization method like the ES. Our approach mimics that one, applying it to the dichromatic model. We obtain a specularity bias that can be used to normalize the images easing further segmentation and detection processes. Due to the slow change in natural illumination, we expect that the estimated bias would valid for several frames, reducing the time constraint for real life application.

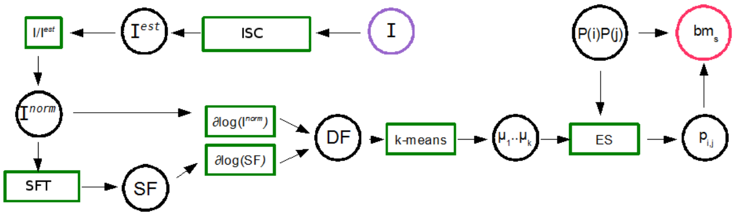

Figure 3.3: Flow diagram of the process of estimating bm_s.

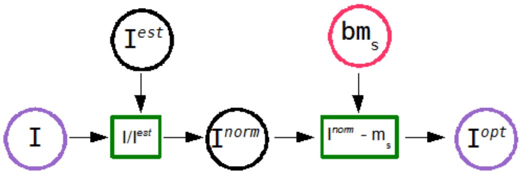

Figure 3.4: Illumination correction using the specular field bm_s.

3.3.1 Description of the approach

Fig. 3.3 shows a flow diagram describing the process to obtain a specularity field. The captured image I that is chromatically normalized by the ISC estimation I^{est} computing the ratio $I^{norm} = \frac{I}{I^{est}}$. To obtain a Specular-Free image [91] (SF), we use the Specular Free Two Band method [87]. Computing the derivatives of the logarithm of SF and I^{norm}, we obtain the diffuse pixels. From them we select the most representative k classes $\{\mu_1, ..., \mu_k\}$, corresponding to chromatic regions in the image. Finally, the ES estimates the parameters of the 2D Legendre polynomials that gives the estimation of the smooth reflectance field bm_s. Fig. 3.4 shows the flow diagram computing the correction of the image removing the specular field bm_s estimated before. The following sections provide a detailed description of the steps in this process.

3.3.2 Image chromatic normalization

Before trying to separate specular and diffuse image components it is necessary to carry out a process of normalization, because the separation process needs the specular component to be pure white color. The value of the ISC I^{est} which can be obtained by some methods [5, 92, 6, 4, 81], included the one described in the previous section. Image chromatic normalization is computed as $I^{norm} = \frac{I}{I^{est}}$, where the ratio is computed at each band independently (it is not a vector operation). After normalization, we ca assume that the image specular component Γ is pure white $[1,1,1]$, therefore the DRM is as follows

$$I^{norm}(x) = m'_d(x)\Lambda'(x) + m_s(x)[1,1,1],$$

because if the ISC is a close approximation to the specular chromatic component of the original image $I^{est} \backsimeq \Gamma$ then the ratio would correspond to the white color $\frac{\Gamma}{I^{est}} \simeq [1,1,1]$, therefore, the DRM of the normalized image is:

$$I^{norm}(x) = \frac{m_d(x)\Lambda(x) + m_s(x)\Gamma}{I^{est}} = \frac{m_d(x)\Lambda(x)}{I^{est}} + \frac{m_s(x)\Gamma}{I^{est}},$$

so that, we have:

$$\frac{m_d(x)\Lambda(x)}{I^{est}} + m_s(x)\frac{\Gamma}{I^{est}} = \frac{m_d(x)\Lambda(x)}{I^{est}} + m_s(x)[1,1,1],$$

where

$$\frac{m_d(x)\Lambda(x)}{I^{est}} = m'_d(x)\Lambda'(x),$$

then we can write:

$$I^{norm}(x) = m'_d(x)\Lambda'(x) + m_s(x)[1,1,1],$$

when working in normalized RGB, this expression becomes:

$$I^{norm}(x) = m'_d(x)\Lambda'(x) + m_s(x)/3.$$

3.3.3 Intensity logarithm differentiation

Pure diffuse pixels are characterized by the lack of contribution of the specular component in DRM:

$$m_s(x) = 0,$$

detection of pure diffuse pixels allows the detection of the specular pixels. Pure diffuse pixels allows us estimate the chromaticity of the surface.

If we compute the logarithm of the chromatically normalized image followed by its spatial differentiation, we have (in normalized RGB color coordinates):

$$\frac{\partial}{\partial x}\log(I^{norm}(x)) = \frac{\partial}{\partial x}\log\left(m'_d(x)\Lambda'(x) + \frac{m_s(x)}{3}\right)$$

For pure diffuse pixels we have that:

$$\frac{\partial}{\partial x}\log(I^{norm}(x)) = \frac{\partial}{\partial x}\log\left(m'_d(x)\Lambda'(x)\right).$$

Assuming that two neighboring pixels have the same diffuse chromaticity thenΛ' does not depend of the spatial coordinate x, therefore:

$$\begin{aligned}\frac{\partial}{\partial x}\log(I^{norm}(x)) &= \frac{\partial}{\partial x}\log\left(m'_d(x)\Lambda'\right)\\ &= \frac{\partial}{\partial x}\left(\log\left(m'_d(x)\right)+\log\left(\Lambda'\right)\right)\\ &= \frac{\partial}{\partial x}\log\left(m'_d(x)\right).\end{aligned}$$

If we compute the logarithm of the Specular-Free image, followed by its spatial differentiation, we have that

$$\begin{aligned}\frac{\partial}{\partial x}\log\left(I^{sf}(x)\right) &= \frac{\partial}{\partial x}\log\left(m'_d(x)\Lambda^{sf}(x)\right)\\ &= \frac{\partial}{\partial x}\left(\log\left(m'_d(x)\Lambda^{sf}(x)\right)\right)\\ &= \frac{\partial}{\partial x}\left(\log\left(m'_d(x)+\Lambda^{sf}(x)\right)\right).\end{aligned}$$

Assuming again that two neighboring pixels have the same diffuse chromaticity, Λ^{sf} does not depend of the spatial coordinate x, then

$$\frac{\partial}{\partial x}\log\left(I^{sf}(x)\right) = \frac{\partial}{\partial x}\left(\log\left(m'_d(x)+\Lambda^{sf}\right)\right) = \frac{\partial}{\partial x}\log\left(m'_d(x)\right)$$

Therefore, to test for a diffuse pixel we compute:

$$\Delta(x) = \frac{\partial}{\partial x}\log(I^{norm}(x)) - \frac{\partial}{\partial x}\log\left(I^{sf}(x)\right).$$

If $\Delta(x) = 0$ then x is a diffuse pixel.

3.3.4 Evolutionary strategy

To build a ES for a given problem, the first step is to propose an energy function whose minimization would solve our problem. This energy function is straightforward to formulate from the DRM

$$E_{tot} = \sum_{x \in I^{norm}} \left(I^{norm}(x) - bm_s(x,p) - \mu_k(x)\right)^2, \tag{3.1}$$

where the illumination bias modeling the specular component field over all the image is given by the 2D Legendre polynomials, built as:

$$bm_s(x,p) = \sum_{i=0}^{l} \sum_{j=0}^{l} p_{i,j} P(i) P(j),$$

where $P(i)P(j)$ denote products of 1D Legendre polynomials. The maximum degree of the Legendre polynomials determined the smoothness of the specular field. The higher the polynomial degrees, the greater the variations allowed in the field.

If we introduce the dichromatic model into the energy function of Eq.3.1, we have

$$E(x) = (m'_d(x)\Lambda'(x) + m'_s(x) - bm_s(x,p) - \mu k)^2,$$

so that

$$E(x) = (m'_d(x)\Lambda'(x) - \mu_k)^2,$$

therefore the energy is proportional to the diffuse component of the image:

$$E(x) \approxeq (m'_d(x))^2$$

The search space is defined by the values of the 2D Legendre polynomials linear coefficients which specify the shape of the specular field. The energy expression in Eq. (3.1) includes class representatives μ_k of the surface reflectance given by the application on samples of the image diffuse pixels of some clustering process (i.e. k-means). Image pixels must be classified according to the reference class before performing the bias search by the ES. The expression in Eq. (3.1) corresponds to the error between the normalized and illumination bias corrected image and the expected color given by the clustering process. It is assumed that scene contains a small number of chromatically different surfaces.

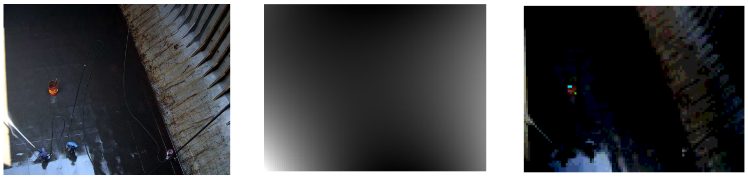

Figure 3.5: From left to right: Original image, the estimated specular bias composed of polynomials of degree up to 2, and the corrected image obtained removing the specular field.

To search for the optimal parameters of the Legendre 2D field, we use an $(\lambda + \mu)$-ES. Each individual in the ES is a matrix of coefficients of the Legendre polynomials. Mutation is provided by random Gaussian perturbations of constant variance. The starting point is population of 50 individuals, which are the seeds for the process. We select the best 20 individuals in an elitist selection process to be the parents for the next generation.

3.3.5 Experimental results

Fig. 3.10 shows the original full image of a ship hold being watered for cleaning. It also shows the recovered image when the highest degree of the Legendre polynomials composing the bias illumination field is 2. Fig. 3.6 shows the bias and the recovered image when the highest polynomial degree is 3. Comparing these figures we can appreciate how increasing the model order the estimated illumination bias tends to fit also the variations in reflectance. Lower order models obtain more robust estimations of the illumination bias. Fig. 3.7 and 3.8 show the effect of the algorithm on the region containing the images of the human operators.

The resulting image after illumination correction is darker than the original image, but it retains all the geometric information, which can be observed computing the spatial gradient of the images. The effect on the hold floor is that we get a constant intensity (color) image of it. The almost specular region on the lower left corner is greatly enhanced, making it more similar to the remaining floor surface. One of the goals of this work is to obtain robust segmentations of objects lying in the surface of the ship hold. It can be appreciated in Fig. 3.7 and 3.8 that the human operators are easily segmented despite the darkening of the image.

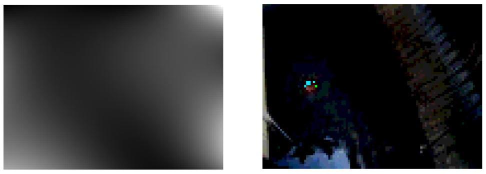

Figure 3.6: From left to right: The estimated specular bias composed of polynomials of degree up to 3, and the corrected image obtained removing the specular field.

Figure 3.7: Detail from figure 4 images. From left to right: original image, estimated specular bias, corrected image obtained removing the specular field.

Figure 3.8: Detail from figure 5 images. From left to right: original image, estimated specular bias, corrected image obtained removing the specular bias.

3.4 Bayesian Reflectance Component Separation

This section proposes a Bayesian approach [93] to the estimation of the specular component of a color image based on DRM. We postulate *a priori* and likelihood energies according to image construction model, composed to formulate an *a posterior*i energy modeling the reflectance estimation process. We postulate the *a priori* distribution based on the fact that the derivatives of the logarithmic images of both diffuse image and specular free must be equal in order to have pure diffuse pixels [91]. Minimization of the *a posteriori* energy gives the desired reflectance estimation. Works on reflectance map estimation usually need to impose some assumptions like the knowledge of a color segmentation of the image, the detection of color region boundaries or color discontinuities, or the knowledge of the decomposition into linear basis functions of the surface color. The approach presented here does not impose any such assumption and does not need previous segmentations of the image.

3.4.1 Separation method

We will base our Bayesian model in the derivative of the logarithm of the normalized image respect to ISC and the specular free transform [4, 91]. We remind the reader that the pure diffuse pixels can be characterized by the following relation:

$$\triangle(x) = d\log(\mathbf{I}'(x)) - d\log(\mathbf{I}^{sf}(x)) = 0, \tag{3.2}$$

where

$$d\log(\mathbf{I}^{sf}(x)) = \frac{\partial}{\partial x}\log(\mathbf{I}^{sf}(x)),$$

and

$$d\log(\mathbf{I}'(x)) = \frac{\partial}{\partial x}\log(\mathbf{I}'(x)),$$

where the logarithm is computed pixel wise, and the spatial derivative can be computed in several ways, for instance in [82] it is computed on the scalar value image given by the summation of the three channels. It can be easily verified that

$$d\log(\mathbf{I}'(x)) = \frac{\partial}{\partial x}\log(m'_d(x)) = d\log(\mathbf{I}^{sf}(x))$$

for pure diffuse pixels if the diffuse chromaticity of neighboring pixels is the same. That means that the method works well inside homogeneous color regions, and needs the estimation of color region boundaries. When $\triangle(x) > 0$ in Eq. (3.2) and the pixel is neither at a color boundary nor a pure specular pixel, then it has some specular component that can be removed to get the diffuse reflectance component. The method proposed in [91] follows from an heuristic observation about the distribution of pixels in the maximum chromaticity versus (normalized illumination color) intensity space. Non diffuse pixels are decreased in intensity iteratively to search for the pure diffuse pixel value.

3.4.2 Bayesian modeling

In this section, we change some notation elements for a better clarity of discourse. Given an image f and a desired unknown response of a computational process d, Bayesian reasoning gives, as the estimate of d, the image which maximizes the *a posteriori* distribution $P(d|f) \propto e^{-U(d|f)}$, where the *a posteriori* energy can be decomposed into the *a priori* $U(d)$ and likelihood (aka conditional) $U(f|d)$ energies $U(d|f) = U(f|d) + U(d)$. The Maximum A Posteriori (MAP) estimate is equivalent to minimize the posterior energy function

$$d^* = \arg\min_d U(d|f) \tag{3.3}$$

The likelihood energy $U(f|d)$ measures the discrepancy between the input image f and the solution d. The *a priori* energy $U(d)$ is a model of the desired solution, usually built as a Random Markov Field (RMF), so that the *a priori* energy can be built up as the summation of the local energies at the pixels, which are expressed as summations over the set of cliques including the pixel, weighted by the local potential parameter. The *a priori* energy usually incorporates any desired constraint, such as smoothness, into the model.

We assume a Gaussian likelihood distribution plus a Chromaticity preservation constraint, therefore the likelihood energy has the following expression:

$$U(d|f) = \sum_{i=1}^{m} \frac{(f_i - d_i)^2}{2\sigma^2} + \sum_{i=1}^{m} \left(\Psi_i^f - \Psi_i^d\right)^2,$$

where f_i and d_i are the RGB pixel values a the i-th pixel position for the observed and desired image, respectively. Also, Ψ_i^f and Ψ_i^d denote the chromaticity pixels of the observed and desired image, respectively.

The *a priori* energy is built up from two components. The first term is the Chromaticity continuity:

$$U_\Psi(d) = \sum_{i=1}^{m} \sum_{j \in N_i} \sum_{c \in \{r,g,b\}} \left(\Psi_{i,c}^d - \Psi_{j,c}^d\right)^2 .$$

The second term models the estimation of the derivatives in Eq. (3.2) as the cliques of the RMF. That is, we assume that the local energy at pixel d_i is defined as

$$U_\triangle\left(d_i\right) = \Big(d \log(d_i) - d \log(d_i^{sf})\Big)^2 ,$$

where d_i^{sf} is the i-th pixel of the specular free image, computed as described above, and $d \log(.)$ in means the local estimation of the derivative, which is approximated as follows:

$$d \log(d_i) = \frac{1}{\#N} \sum_{j \in N_i} \log(\frac{I(x_j)}{I(x_i)}),$$

where N_i is the local neighborhood of pixel d_i, and $\#N$ is its cardinality. After some manipulations, the local derivative component of the *a priori* energy is derived as:

$$U_\triangle\left(d_i\right) = \left(\sum_{j \in N_i} \sum_{c \in \{r,g,b\}} \log \frac{d_{j,c} d_{i,c}^{sf}}{d_{i,c} d_{j,c}^{sf}}\right)^2 .$$

This local energy is equivalent to the Kuk-Jin ratio criterion [87]. The derivative component of the *a priori* energy is, therefore, the addition of these local energies:

$$U_\triangle\left(d\right) = \sum_{i=1}^{m} U\left(d_i\right),$$

and the *a priori* energy is given by:

$$U\left(d\right) = U_\triangle\left(d\right) + U_\Psi\left(d\right).$$

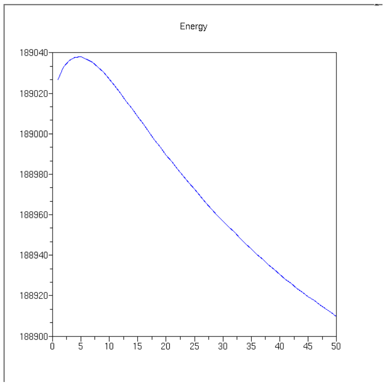

Figure 3.9: Evolution of the energy function in an instance run of the algorithm

3.4.3 Experimental results

In this section we report some experimental results applying the Bayesian approach described above. The starting value for the energy minimization process is set to $f = d(0) = \mathbf{I}'$. Each iteration step of the energy minimization involves the computation of the specular free image $d^{sf}(t)$ of the current hypothesis $d(t)$ of the optimal estimation d^{*}. Instead of using a Monte Carlo minimization technique [93], such as Simulated Annealing, we have employed a simple heuristic to determine the new hypothesis $d(t+1)$, consisting in the reduction of the intensity of the pixels preserving their chromaticity components relative ratios. Although simple, this strategy does in fact produce a minimization of the energy function, as can be appreciated in Fig. 3.9, where we plot an instance of the energy function evolution. We have tested our approach on some images already tested by some authors in the literature i.e. [82, 91] among others. Fig. 3.10 shows the result over a well known test image with two colors and two light sources. Our algorithm does not include any modeling of the underlying color regions in the scene, such as in [82], so it can be appreciated that the almost pure specular pixels can not be corrected, because there almost no chromatic information left in them. To improve our approach we will be including a color map field in the model, to be able to assign those pixels the most likely color. The Fig. 3.11 shows an image with a more complex surface geometry. Our estimation of the diffuse reflectance component recovers the underlying geometry, with some blurring effects.

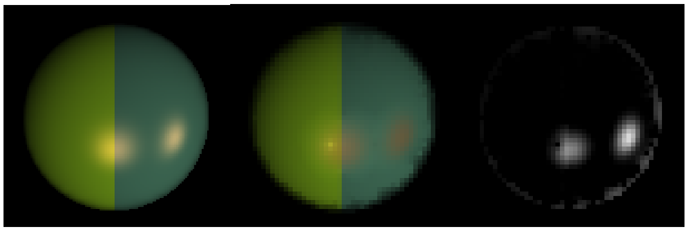

Figure 3.10: From left to righ, the original image, the estimated diffuse reflectance component, and the estimated specular component

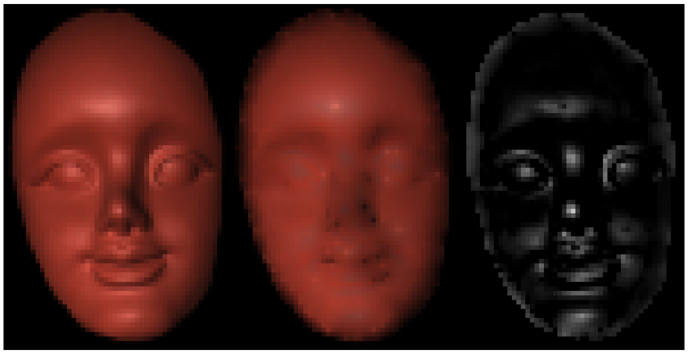

Figure 3.11: From left to right, the original image, the estimated diffuse reflectance component, and the estimated specular component

3.5 A geometrical Method Image Component Separation

The approach presented here is based on observed properties of the distribution of pixel colors in the RGB cube according to DRM. We estimate the lines in the RGB cube corresponding to the diffuse and specular chromaticities. Then the specular component is easily removed by projection onto the diffuse chromaticity line. Besides, the specular component is computed by a straightforward difference. The proposed algorithm does not need any additional information. The process is as follows: first we estimate the chromatic lines; second, we perform the separation process, estimating the diffuse image component; third, we compute the specular image component. We show some computational results on well known benchmark images.

3.5.1 Pixel distribution on RGB color space

Following DRM we can classify image pixels into: Diffuse pixels: showing the observed surface color, with an almost null specular component. Specular pixels: whose specular component is much bigger than the diffuse component. Placement of diffuse and specular pixels is qualitative different in the RGB cube. Let us focus on the pixels in the proximity to the black-white cube diagonal, defined as

$$L_w = \{(r, g, b) = P + sw; \forall s \in [0, 1]\}$$

where $P = (0, 0, 0)$ and $w = (1, 1, 1)$. Given a uniform color region without any specular component, its representation in the RGB cube would be a line, the diffuse chromaticity line for this region. Given a uniform color region in the image with high specular component, it must appear like a line parallel to line L_w or close to it. Specular image regions have RGB representations far from the color space origin. However, due to noise, lines appear as an elongated point clouds. Finally, a uniform color region (color constancy) with some non negligible specular component must show a V shape. The point cloud beginning in the coordinate origin and going away from line L_w contain the diffuse points, while the ones close to line L_w are the specular ones. Using this knowledge, we can filter out the specular component and retain the diffuse component.

3.5.2 General description of the method

We assume that the observed surface is decomposable into patches of homogeneous chromatic characteristics. The proposed method has the following phases:

1. Chromatic line estimation: estimate the diffuse line L_d and the specular line L_s .
2. We compute the parameters of the chromatic plane Π_{dc} in the RGB cube, and we project all the pixel colors into this plane. This step involves some additive noise removal.
3. Component separation: We compute the pure diffuse image component and the specular image component.

3.5.3 Chromatic line estimation

In Fig. 3.12 we have a plot of the pixels in the image of Fig. 3.13 in the RGB cube. Let us denote them $\{I_i; i = 1, ..., M\}$. We can easily appreciate the two main directions in the data. The most clear is the one corresponding to the diffuse line L_d which rises from the coordinate system origin. The second, less defined, appearing at the end of the diffuse elongation, is the specular direction identified by the specular line L_s.

To estimate the diffuse line, we start selecting the less bright pixels in the image region corresponding to the surface, which will have the greatest diffuse component. We plot them in the RGB cube and we estimate the best linear regression on the RGB data. In fact, we perform a Principal Component Analysis [94] (PCA) which give us the direction of the chromatic line $\overrightarrow{u}$. Therefore the diffuse chromatic line is defined as

$$L_d = \{(r, g, b) = P + s\overrightarrow{u}; \forall s \in \mathbb{R}\}\,.$$

Analogously, we select the brightest pixels, obtaining a mean point Q in the RGB cube and the largest eigenvector $\overrightarrow{v}$ for the specular color, therefore the specular chromaticity line is expressed as follows

$$L_s = \{(r, g, b) = Q + t\overrightarrow{v}; \forall t \in \mathbb{R}\}\,.$$

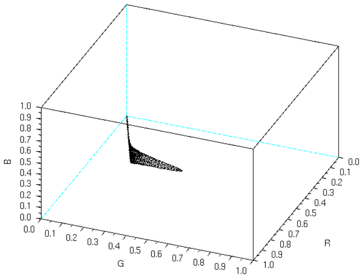

Figure 3.12: Synthetic image plotted in the three-dimensional RGB space

3.5.4 Image regularization

Once we know the chromatic lines, we build the dichromatic plane Π_{dc} in $\mathbb{R}^3$ which is the best planar approximation to the color distribution in RGB. It can be expressed as follows:

$$\Pi_{dc} = \{(r, g, b) = P + s\overrightarrow{u} + t\overrightarrow{v}; \forall s, t \in \mathbb{R}\},$$

The plane normal vector is $\overrightarrow{N} : \overrightarrow{u} \times \overrightarrow{v}$, where $\times$ denotes the conventional vector product. To remove noise and regularize the image colors we project the pixel's colors into this dichromatic plane Π_{dc}. For each pixel color I_i in the RGB cube, we compute the line

$$L_i = \left\{(r, g, b) = I_i + k\vec{N}; \forall k \in \mathbb{R}\right\},$$

which is orthogonal to the dichromatic plane Π_{dc}. To regularize I_i we compute its projection I_i^c as the intersection of L_i with Π_{dc}.

3.5.5 Component separation

Recalling the DRM $I(x) = m_d(x)D + m_s(x)S$ our goal is to bring the pixels to the diffuse chromatic line, that is $\forall x : m_s(x) = 0$. We proceed as follows:

- For each regularized image point I_i^c lying in the plane Π_{dc} we draw the line

  $$L_i = \{(r, g, b) = I_i^c + t\overrightarrow{v}; \forall t \in \mathbb{R}\}$$

  where $\overrightarrow{v}$ is the specular line direction vector.

- The pixel diffuse component corresponds to the intersection point I_i^d of this line with the diffuse line

$$L_d = \{(r, g, b) = P + s\overrightarrow{u}; \forall s \in \mathbb{R}\}$$

existing because they lie in the same plane Π_{dc} and they are not parallel lines.

- We have obtained $I^d(x) = m_d(x)D$ so that $\forall x, : m(x) = 0$, and the resulting image $I^d(x)$ is purely diffuse, without specular components.

- Obtaining the specular image component is then trivial if we recall the DRM definition:

$$I^s(x) = I(x) - I^d(x) = I(x) - m_d(x)D = m_s(x)S.$$

3.5.6 Experimental results

The experimental demonstration of our approach is shown in Figs. 3.13 and3.14. The first is a synthetic image (generated using Blender), and the second is a natural image. Both are monochromatic. Original image is the leftmost image in both figures. Following our approach we obtain the diffuse and specular images, shown at the center and rightmost images, respectively, in both figures. Both original images can be downloaded from http://www.ehu.es/ccwintco/index.php/Images. The natural image has been used as benchmark by several researchers [91, 82]. The visual results are comparable or better than the state of the art results in [91, 82]. As we know the original surface color ($r = 0.790$, $g = 0.347$ and $b = 0.221$) in the synthetic image, we can compute an estimation of the error committed by our estimation of the diffuse image. If we denote Q the original color, the error is the distance of this point to the diffuse line, computed as $d(Q, L_d) = ||\vec{PQ} - \perp(\vec{PQ}, \vec{u})||$, where $\perp(\vec{a}, \vec{b})$ denotes the projection operator. In the images shown in Fig. 3.13 the error committed is 0.0116. Variations in the error are due to the diffuse region pixel selection.

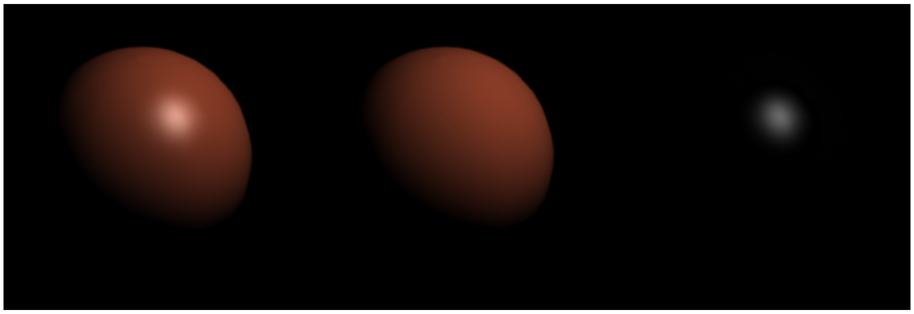

Figure 3.13: Synthetic image, diffuse image and specular image

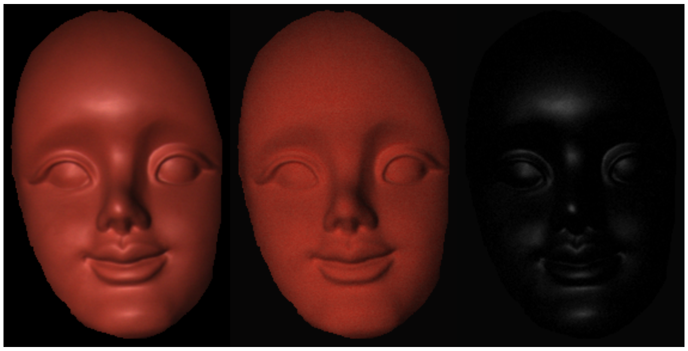

Figure 3.14: Natural image, diffuse image and specular image

3.6 Chapter Conclusions

This chapter gather four works that have in common the separation of the image into diffuse and specular components for normalization and image correction, with the aim of improving ensuing segmentation results. Though there is a common ground on the DRM, these works come from diverse computational backgrounds and have diverse goals, however we have ordered them according to their potential composition in a complete system. First, we presented a method for the illumination source chromaticity estimation, which can be used for the image chromatic normalization. Second, we present a method for the estimation of the illumination field for image correction. Third, we present a bayesian and a geometrical approaches for specular and diffuse component separation.

Bayesian method which does not need any additional assumption, such as models of the colors in scene o previous color segmentations of the image. It converges linearly by intensity reduction in the ISC line. Finally we have propose a geometrical method for separate the diffuse and specular components. This method is faster that other ones and provides excellent results. A further work is to extend this model to multi-chromatic surfaces.

Illumination Source Chromaticity The method for Illumination Source Chromaticity (ISC) estimation is accurate, and its complexity is linear in the number of pixels, therefore it is suitable for real time. It works on the spherical coordinates of the specular pixels of the image, which is a small fraction of the whole image. It does not lose luminosity information, because it is preserved in the magnitude component of the spherical representation which is not affected by color normalization. It can be applied in real time. It is the first step in any segmentation model that let us normalize the images respect to the illumination chromaticity obtaining robustness respect to illumination changes. We have shown in computational experiments that it improves over state of the art competing algorithms.

Evolution Strategy for Parametric Illumination Field Estimation We have shown an image correction approach based on the modeling of the specular component of the image as bias field obtained as the linear composition of 2D Legendre polynomials. Model fitting is done by a $(\lambda + \mu)$-ES on the space of the linear coefficients of the Legendre polynomials. The approach is based on the dichromatic reflectance model. The effect is that we can remove strong specularity effects from difficult scenes, such as the ship hold treated as example, allowing more robust segmentation of objects in the image. The method could be applied to static robotic monitoring in teams of robots, where the illumination gradient image could be computed once and applied to successive frames until the illumination conditions change drastically. The method could be useful for the detection of image regions with different chromatic properties.

Bayesian Component Separation We have presented a Bayesian approach to the problem of reflection component separation. As in previous works, our approach works with only one image [91] and does not need any additional assumption, such as models of the colors in scene o previous color segmentations of the image. We compute the specular free image, which can be done on the fly for each hypothesis. We have tested the approach applying a simple heuristic to provide new hypothesis from the previous iteration, with quite encouraging results. From the experiments we detect the need to incorporate a color map field in the *A Priori* model, so that the color of almost purely specular pixels can be recovered more easily. The problem of diverse color illumination sources may be the subject of further works.

Geometrical Component Separation The geometrical component separation for mono-color images is very effective, fast and robust. It has been inspired in the spatial distribution suggested by DRM so that it is well theoretically grounded despite its simplicity. It consists in the estimation of the diffuse and specular lines as the principal components of diffuse and specular point clouds, respectively, selected from the image by hand. Contrary to other approaches [78, 85] our approach does not need specific hardware devices, and only needs one image. Our approach's complexity time is linear in the image size $O(M)$, while others [87, 91] are quadratic $O(M^2)$. Our approach does not need a Specular Free image, it provides almost simultaneously both image components. Future work will address the extension of this approach to images containing several surface colors, i.e. $I(x) = m_d(x)D + m_s(x)S$, and to images with illumination sources of different colors, i.e. $I(x) = m_d(x)D + m_s(x)S(x)$.

Chapter 4

Specular Free Images

Specular free (SF) images are equivalent to the original image but with their specular component removed. Computation of specular free images are necesary steps for some processess such as image component separation or illumination source chromaticity estimation for chromatic normalization. This chapter contains two algorithms approaching this issue from different points of view. First, we introduce a SF transformation (denoted SF2) based on the pseudo-norm of the saturation [95]. The second SF transformation (denoted SF3) is based in the angular definition of the color saturation following DRM behavior in RGB. SF3 applies the intensity depending of the pixel chromaticity. This SF image is applied on natural and synthetic images. The processes are grounded in the DRM. Both SF transformations are defined on the HSV color space.

The chapter's outline is as follow: Section 4.1 introduces specular free image transformations. Section 4.2 presents the SF2 method and some experimental results. Section 4.3 presents the SF3 . Section 4.4 gives the chapter conclusions.

4.1 Specular Free Image Transformations

There are scarce works on SF transformation, which were introduced by Roby Tan [82] and Kuk-jin Yoon [87] more or less at the same time. In the first approach, the basic idea is to make the saturation constant for all surface colors while retaining their hue values. In other words, if these images preserve their hue and saturation, then preserve the chromaticity, therefore they change only the intensity respect to the original image. In the approach of Kuk-Jin, the transformation project all RGB points within the nearest plane using the achromatic direction. In both cases, specular free transformations are geometrical and injective transformations in the RGB color space where the output image, the specular free image has not specular component.

4.2 A Color Transformation

We expect that in pure color regions the color representation of the pixels in the RGB cube will fall far from the achromatic line. On the other hand, we want to penalize specular regions, those close to achromatic line and far from the coordinate system origin. A main feature of achromatic line is that the three coordinates of its points are equal $r = g = b$, and $r, g, b \in [0, 1]$. For pixels close to this region, we $r \approxeq g \approxeq b; r, g, b \in [0, 1]$. As the pixels fall away from this line, the differences among their components are greater. We use this difference as the intensity of the processed image. As we want to preserve the chromatic information, only the intensity is modified, boosting the diffuse pixels and nullifying the specular pixels. The new intensity of the pixels is computed as difference between the maximum and minimum of their RGB components:

$$I(x) = \max\{r, g, b\}(x) - \min\{r, g, b\}(x)$$

This new intensity replaces the V component in the HSV representation, thus preserving the chromatic content of the pixel. We show in Algorithm 4.1 an implementation for SciLab. The image obtained after the SF2 transformation is characterized by the absence of reflections, substituted by dark spots. Also the diffuse regions are boosted in the image. With an straightforward analysis we can find all the diffuse regions.

4.2.1 Experimental results

The need to detect color regions stems from its conventional use in signaling: red for danger, blue and green for informative, yellow for danger advice. In robotic contexts, working on artificial environments, we must benefit from this information source by the robust detection of signaling symbols drawn in the basic colors. We have performed experiments in

Algorithm 4.1 Scilab code for SF2

```
//I is a RGB image
// IR is the transformed image
Function IR = SF2(I)
  New_Intensity = (max(I,3) - min(I,3));
  Imghsv = rgb2hsv(I);
  Imghsv(:,:,3) = New_Intensity;
  IR = rgb2hsv(Imghsv);
Endfunction
```

three different contexts: first the detection of markers in real scenes, second the process of synthetic images, and third the detection of robots in real time. All the results can be viewed in the following web address: http://www.ehu.es/ccwintco/index.php/SMC

4.2.1.1 Landmark detection

The definition of the experiment is as follows: The place is a lab corridor, with artificial illumination of diverse intensity and uniform color. Landmarks are DIN A4 sheets of different colors: red, cyan, yellow and blue. We use a conventional web cam Phillips SPC 900NC/00. From each image (recorded in a MPEG file) we find the SF2 images, and there we find the markers.

In Fig. 4.1 we have three images from the described scenario. The ones on the left are the closest ones to the camera, the ones on the right are the farthest ones. Notice variations in illumination along the corridor. In Fig. 4.2 we show the SF2 images as follows: left corresponding to the middle one in Fig. 4.1 , middle after the analysis of the intensity and to the right a zoom of the previous one, showing that one mark is missing. In table 4.1 we show the detections performed on each mark, where 'x' means good detection and '+' incomplete detection.

Figure 4.1: Natural images for landmark detection.

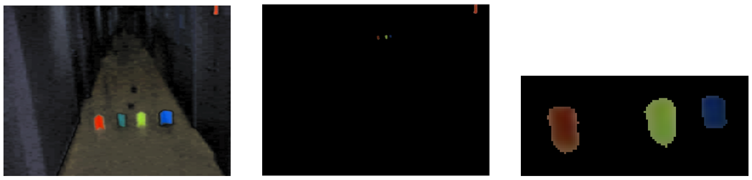

Figure 4.2: Specular free images obtained by SF2.

Milestone	1	2	3	4	5	6	7	8	9	10	11	12	13	14	15
Distance (m)	2.6	4	6	8.4	10.8	12.8	14.5	17.3	20.7	26.02	31.7	36	41.9	46	50
Label 1	x	x	x	x	x	x	x	x	x	x		x	+	x	
Label 2	x	x	x	x	x	x	+								
Label 3	x	x	x	x	x	x	x	x	x	x	x	x	+	x	
Label 4	x	x	x	x	x	x	x	x	x	x	+				

Table 4.1: Measurements

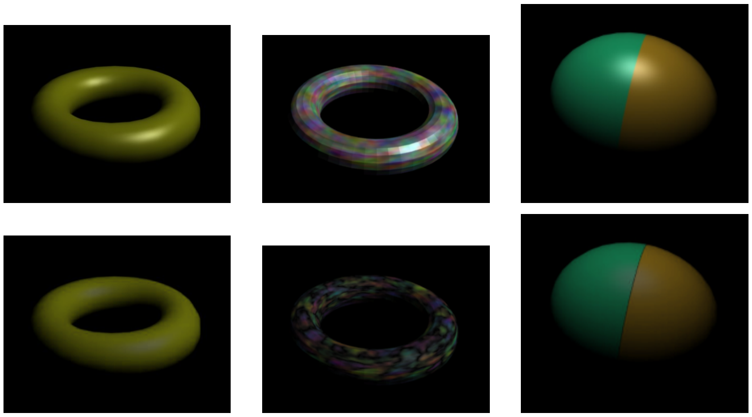

Figure 4.3: Synthetic images for the experiments. Upper row, original images. Lower row, images after SF2.

4.2.1.2 Synthetic images

The SF2 transformation has been applied to natural and synthetic images. Synthetic images have the advantage that we know with precision the color and geometry of the surface, as well as the illumination color. Fig. 4.6 shows some of these images, in the top row we place the original image and on the bottom the computed SF2 images. First image is a monochromatic image, containing a green toroidal surface. The second is a Voronoi tessellated toroidal surface painted with random colors. Last image is a bi-chromatic oval. We observe that SF2 images remove completely all the reflections, canceling the specular component. In the Voronoi tessellated ring surface, besides canceling brights spots, colors have been enhanced.

The SF2 method has been ideated for robotic contexts. In Fig. 4.8 we show results on three natural images. The two first ones are customary marks in the previously described experiment, and the last one is used by other researchers in the literature of specular correction. The first two scenes show the enhancement of the markers in the image. In the last case we see that the bright spots are cleanly removed, retaining the original color.

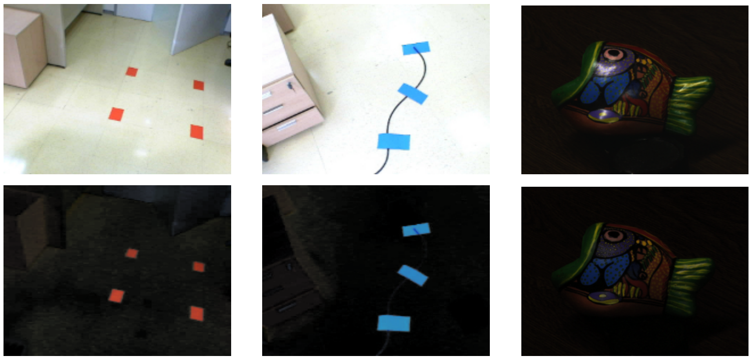

Figure 4.4: Natural image experiments. Upper row, original images. Lower row, SF2 output images.

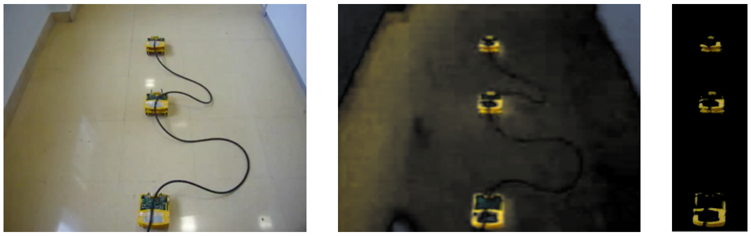

Figure 4.5: Robot detection. Left, original image. Right, the resulting image segmentation. Middle, the result of the SF2 process.

4.2.1.3 Real robot detection

The last experiment is the detection of small robots (SR1) in a real scene and real time. The robots are yellow color against a yelowist background, making visual detection tricky. The floor is very bright with many bright spots front above illumination. Besides, robot's upper part contains the printed board and some fixing for the cable being carried. The robots have lots of shadows, thus only a small part of the robot can be clearly detected as pure yellow. Fig.4.5 contains three images: first the capture from the scene, second its SF2 image, third the SF2 image intensity analysis to detect the robots. The web address http://www.ehu.es/ccwintco/index.php/SMC contains the original video. We must point out that illumination is not constant, there are doors, windows, etc.

4.3 Hybrid Color Space Transformation to Visualize CC

This section presents a hybrid and non linear transformation of the RGB image based on the assignment of the chromatic angle of the pixel (computed in the RGB space) as the luminosity value in the HSV space. The image is preprocessed to remove the specular component. The chromatic angle was defined on the basis of DRM, having thus a physical interpretation supporting it. In the HSV color space the intensity is represented in the V value, changing it does not change the pixel chromatic information. Thus, to visualize CC we assign constant intensity to the pixels having common chromatic features, by assigning the chromatic angle as the V value in HSV space.

4.3.1 Regularized region intensity

The basic idea of our approach is to assign a constant luminosity to the pixels inside an homogeneous chromatic region. To do that we must combine manipulations over the two color space representations of the pixels, the HSV and RGB. The process is highly non linear and it is composed of the following steps:

1. Isolate the diffuse component removing specular components ($m_s = 0$): we are interested only in the diffuse component because it is the representation of the true surface color. We use the method presented in [91] to perform the diffuse and specular component separation.
2. Transform the diffuse RGB image into the HSV color space.
3. Compute for each pixel in the image the chromaticity angle as the angle between the gray diagonal line in the RGB space, going from the black space origin to the pure white corner, and the chromaticity line of the pixel.
4. Assume the normalized chromaticity angle as the new luminosity value in the HSV space pixel representation.

In an homogeneous chromatic region, all pixels fall on the same diffuse line

$$L_d = \left\{(r, g, b) = \mathbf{O} + s\mathbf{\Psi}; \forall s \in \mathbb{R}^{+}\right\}$$

where $\mathbf{O} = [0,0,0]$ and $\mathbf{\Psi} = [\Psi_r, \Psi_g, \Psi_b]$ is the region's chromaticity expressed in Euclidean coordinates. The chromatic reference is the achromatic (pure white) line L_{pw} which is defined as

$$L_{pw} = \left\{(r,g,b) = \mathbf{O} + s\mathbf{u}; \forall s \in \mathbb{R}^+\right\}$$

where $\mathbf{O} = [0,0,0]$ and $\mathbf{u} = [1,1,1]$. Therefore, if all pixels is a region belong to the same chromatic line, the angle between each pixel and the line L_{pw} must be the same, and the result of this angular measurement is a constant for whole region. Our approach normalizes this measure in his domain of definition (the RGB cube) and assume it as the constant luminosity value V. This method is expressed with the equation:

$$V^{new}(x) = \frac{\angle\left(\mathbf{I}(x), \mathbf{u}\right)}{\arccos(\vartheta)} \tag{4.1}$$

where the denominator $\arccos(\vartheta)$ is the normalization constant corresponding to the maximum angle between the extreme chromatic lines of the RGB space (red, green or blue axes) and the pure white line. Algorithm 4.2, shows a Matlab/Scilab implementation of the method, where ϑ takes the value $\frac{1}{3}$ and $\arccos(\vartheta) = 0.9553166$.

Algorithm 4.2 Regularized Region Intensity computatoin

```
function IR = SF3(I)
  Idiff = imDiffuse(I); // look for the diffuse component
  new_intensity = angle(Idiff, [1 1 1]); // return a matrix of chromatic angles
  Ihsv = rgb2hsv(Idiff);
  Ihsv(:,:,3) = new_intensity; // assign the normalized angles as image intensity
  IR = hsv2rgb(Ihsv);
endfunction
```

4.3.2 Experimental results

We present the results from three computational experiments. The first one using a synthetic image and the remaining using natural images. Fig. 4.6

displays the first experimental results. Fig. 4.6(a) is the original image. Fig. 4.6(b) is the diffuse image obtained applying the method in [82]. Fig. 4.6(c) is the result applying our proposed method in Fig. 4.6(a). Fig. 4.6(d) display the result applying the method in Fig. 4.6(b). It can be appreciated that our method is able to identify the main chromatic regions even without component separation (Fig. 4.6c), with some artifact due to the bright reflections. After removal of these reflections, the method has a very clean identification of the chromatic regions.

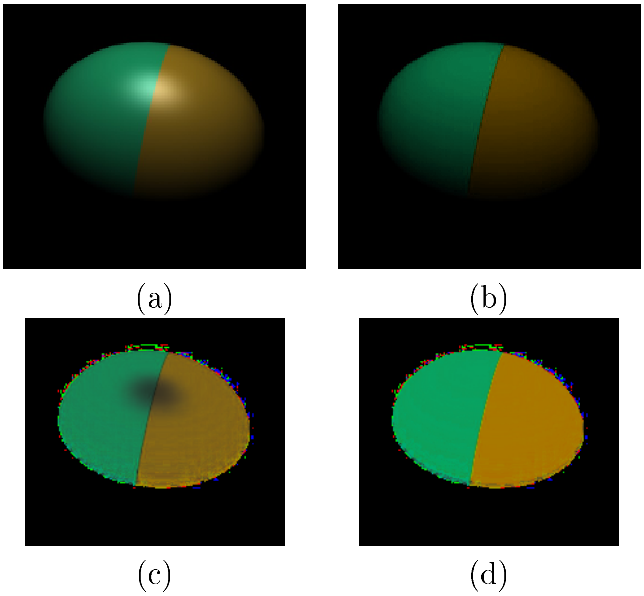
(a) (b)
(c) (d)

Figure 4.6: Synthetic image results (a) original image, (b) diffuse component of the image, (c) our method on image (a), our method on image (b).

For the next experiments we use natural images that have been used by other researchers previously. The Fig. 4.7 and 4.1 show the experimental results. In both cases the sub-figure (a) has the original image, sub-figure (b) shows the diffuse image, sub-figure (c) displays the results applying our proposed method to the original image (a), sub-figure (d) show the results applying our method in the diffuse image (b). In both experiments we can see a similar effect of applying specular correction. The images (c) obtained

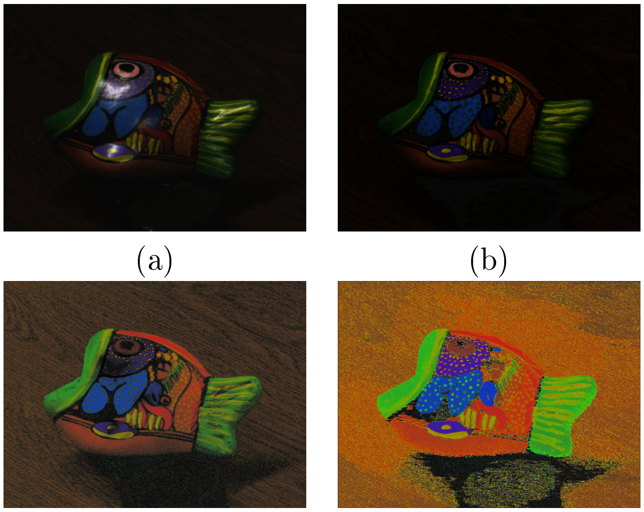

(a) (b)

(c) (d)

Figure 4.7: Natural image results, (a) original image, (b) diffuse component of the image, (c) our method on image (a), our method on image (b).

without component separation, show a better chromatic preservation, although with some degradation in the regions corresponding to the specular brights. The images obtained after diffuse component identification [82] are less sensitive to specular effects, however they show some chromatic region oversegmentation. It is important to note that no clustering process has been performed to obtain these images.

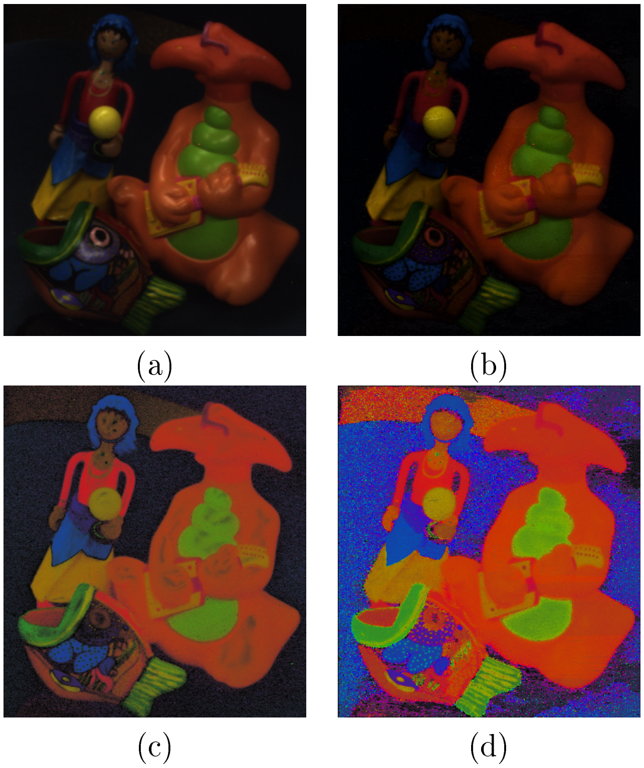
(a) (b)

(c) (d)

Figure 4.8: Natural images, (a) original image, (b) diffuse component of the image, (c) our method on image (a), our method on image (b).

4.4 Conclusions

Specular free images are a powerful tool to overcome the noise introduced by highlights. This chapter presents two specular free transformations. The first one, computes the saturation seudo-norm of the pixels. It is very fast, allowing for real time response in artificial vision environments. It removes efficiently the specular component of the image, retaining and enhancing the original colors, because it preserves chromatic information in the HSV color space.

The second method substitutes the intensity component in the HSV color space representation of each pixel in the image by a normalized angular distance between the pixel color and the achromatic line. The transformation preserves the pixel chromaticity and assigns a constant intensity to the pixels in a homogenously colored region. The result is a new image with strong contrast between chromatic homogeneous regions, and good visualization of these regions as uniform regions in the image. This method performs very well in dark regions, which are critical for most CC methods and image segmentation based on color clustering processes. SF image is a new topic in computer vision or image processing which can help to solve task related with to avoid specular effects on images. We advocate its application and further improvements.

Chapter 5

Chromatic Gradient

This chapter presents a color image spatial gradient with good color constancy preservation properties. The approach does not need a priori information or color space transformations. It is based on the angular distance between pixel color spherical coordinate representation in the RGB space. It is naturally invariant to intensity magnitude, implying high robustness against bright spots produced be specular reflections and dark regions of low intensity [96].

The sructure of the chapter is as follows: Section 5.1 revisits the color constancy in the RGB space. Section 5.2 recalls the linear gradient detection basics. Section 5.3 describes the chromatic gradient. Section 5.4 gives some experimental results. Section 5.5 provides the chapter conclusions.

5.1 Color Constancy in the RGB Space Revisited

We recall that Color Constancy (CC) is our ability to perceive the same color despite changes in illumination. The basic CC is the robustness against changes in illumination intensity. CC is fundamental problem in artificial vision [18, 80, 97], which has been the subject of neuropsicological research [13]. CC can be very influential in Color Clustering processes [81, 98, 46]. In the artificial vision framework, CC assumes some color space, involving the illumination source chromaticity estimation [84, 18] and the separation of diffuse and specular image components [91, 87, 83]. We have observed in previous chapters that chromaticity in the RGB space is characterized by a straight line crossing the RGB space's origin, determined by the ϕ and θ angles of the polar coordinates of the points over the line. The plot of the pixels in a chromatically uniform image region appear as straight line in the RGB space, which we call the *diffuse line* L_d. If the image has surface reflection bright spots, the plot of the pixels in these regions appear as another line L_s intersecting L_d.

For diffuse pixels having a small specular component weight $m_s(x)$ in DRM, the zenithal ϕ and azimuthal θ angles are almost constant, while they are changing for specular pixels, and dramatically changing among diffuse pixels belonging to different color regions. Therefore, the angle between the vectors representing two neighboring pixels I_p and I_q, denoted $\angle\left(I_p, I_q\right)$, reflects the chromatic variation. For two pixels in the same chromatic regions, this angle is $\angle(I_p, I_q) = 0$ because they will be collinear in RGB space.

5.2 Linear Gradient Operators

The notion of CC is closely related to the response to the gradient operators [17]. Regions of constant color must have low gradient response, while color edges must have a strong gradient response. To set the stage for our chromatic gradient proposition, we need to recall the definition of the image gradient

$$G[I(i,j)] = \begin{bmatrix} G_i \\ G_j \end{bmatrix} = \begin{bmatrix} \frac{\partial}{\partial i} I(i,j) \\ \frac{\partial}{\partial j} I(i,j) \end{bmatrix}, \tag{5.1}$$

where $I(i,j)$ is the image function at pixel (i,j). For edge detection, the usual convention is to examine the gradient magnitude:

$$G\left(I\right) = |G_i| + |G_j|. \tag{5.2}$$

For color images, the simplistic approach to perform edge detection is to drop all color information, computing the intensity $Intensity = (Red + Green + Blue)/3$ (sometimes computed as $Intensity = .2989 * Red + .587 * Green + .114 * Blue$), and then convolve the intensity image with a pair of high-pass convolution kernels to obtain the gradient components and gradient magnitude. The most popular edge detectors are the Sobel and the Prewitt detectors, illustrated in Fig.8.1. We build our own operators along similar kernel patterns. To take into account color information, the easiest approach is to apply the gradient operators to each color band image and to combine

$$\begin{bmatrix} -1 & 0 & 1 \\ -2 & 0 & 2 \\ -1 & 0 & 1 \end{bmatrix} \begin{bmatrix} -1 & -2 & -1 \\ 0 & 0 & 0 \\ 1 & 2 & 1 \end{bmatrix}$$

(a)

$$\begin{bmatrix} -1 & 0 & 1 \\ -1 & 0 & 1 \\ -1 & 0 & 1 \end{bmatrix} \begin{bmatrix} -1 & -1 & -1 \\ 0 & 0 & 0 \\ 1 & 1 & 1 \end{bmatrix}$$

(b)

Figure 5.1: Convolution kernels for the (a) Sobel and (b) Prewitt edge detection operators.

the results afterwards: $G(I) = [G(I_r) + G(I_g) + G(I_b)]/3$. Fig. 5.2 show the results of applying those basic approaches to edge detection on a synthetic image. It can be appreciate how the gradient magnitude amplifies noise on one hand when we combine the color band gradient magnitudes, and how the color edge is not detected by the edge operator applied to the intensity image, because the two color regions have quite near intensity values. The edge magnitude computed by the straightforward approaches is also misled by the specular surface reflections, which highlighted as can be appreciated in Fig.5.2(d).

5.3 Chromatic Gradient

We first introduce a distance between pixel color values which preserves chromatic coherence having some color consistency properties. Then we formulate the gradient operators built upon this chromatic distance.

5.3.1 A chromatic distance in RGB

First, we convert the RGB Cartesian coordinates of each pixel to spherical coordinates, with the black color as the RGB space origin. Let us denote the Cartesian coordinate image as $I = \left\{ (r, g, b)_p \, ; p \in \mathbb{N}^2 \right\}$ and the spherical

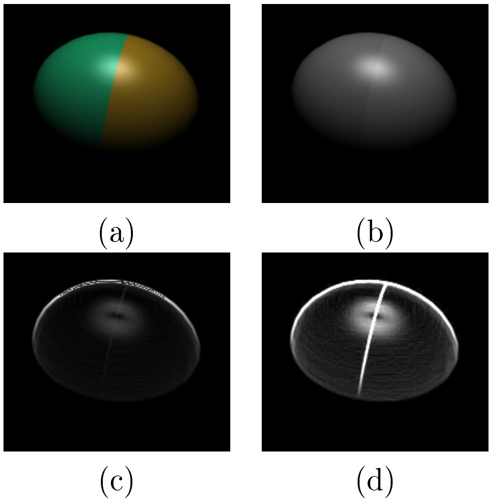
(a) (b)

(c) (d)

Figure 5.2: (a) Original synthetic RGB image, (b) Intensity image, (c) Gradient magnitude computed on the intensity image, (d) gradient magnitude combining the gradient magnitudes of each color band

coordinate as $P = \{(\phi,\theta,l)_p; p \in \mathbb{N}^2\}$, where p denotes the pixel position. We discard the l because it does not contain any chromatic information. For a pair of image pixels p and q, the color distance between them is defined as:

$$\angle(P_p, P_q) = \sqrt{(\theta_q - \theta_p)^2 + (\phi_q - \phi_p)^2}, \tag{5.3}$$

that is, the color distance corresponds to the Euclidean distance of the Azimuth and Zenith angles of the pixel's RGB color polar representation. This distance is not influenced by the intensity and, thus, will be robust against specular surface reflections.

5.3.2 Chromatic gradient operators

Notice that the linear convolution operators are computing distances between pixels to compute the derivative. We substitute the direct difference by the chromatic distance introduced above to obtain pseudo-convolution operators. We formulate a pair of Prewitt-like gradient pseudo-convolution operations on the basis of the above distant. Note that the $\angle(P_p, P_q)$ distance is always positive. Note also that the process is non linear. The row pseudo-convolution is defined as

$$CG_R\left(P\left(i,j\right)\right) = \sum_{r=-1}^{1} \angle\left(P\left(i-r,j+1\right), P\left(i-r,j-1\right)\right),$$

and the column convolution is defined as

$$CG_C\left(P\left(i,j\right)\right) = \sum_{c=-1}^{1} \angle\left(P\left(i+1,j-c\right), P\left(i-1,j-c\right)\right),$$

so that the color distance between pixels substitutes the intensity subtraction of the Prewitt linear operator. The color gradient image is computed as:

$$CG(P) = CG_R\left(P\right) + CG_C\left(P\right) \tag{5.4}$$

5.4 Experimental Results

To demonstrate the efficiency of our proposed approach, we show three experimental results. Two of the experiments are done on synthetic images whose ground truth is know. Fig. 5.3 contains two synthetic images Fig. 5.3(a) and 5.3(b) which are chromatically identical. The image in Fig. 5.3(a) hs constant intensity inside each color region, while the image in Fig. 5.3(b) contains a central square with lower intensity (0.8), preserving the chromatic content of Fig. 5.3(a). Applying the Prewitt operator to each color band of Fig. 5.3(b) we obtain the detection shown in Fig. 5.3(c), while applying our color edge detection of Eq. (8.2) we obtain the detection in Fig. 5.3(d). It is clear that our approach has superior CC properties and an improved intensity invariant detection of color edges.

The second computational experiment was performed on the image shown in Fig. 5.2(a). This image has a strong specular reflection region, and two color regions with a black background. We have tested a Sobel like and a Prewitt like variation of the basic schema of Eq.(8.2). The Fig. 5.4 gives the results of the RGB band combined detection and our approach. It can be appreciated that our approach discovers the edge even in very dark areas, it is also robust against specular reflections, which the linear operators do confound with color edges. The color edge between the two regions is better detected in both cases by our approach.

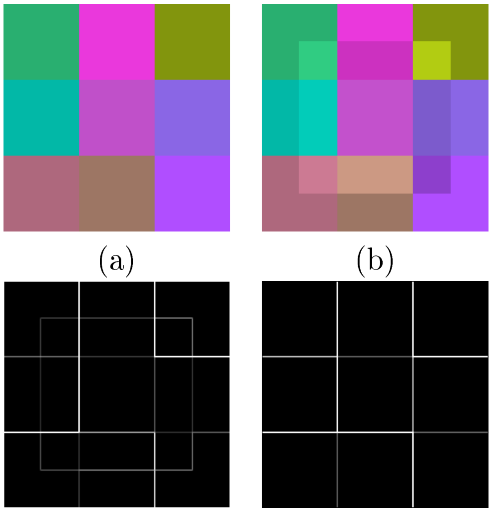

(a) (b)

(c) (d)

Figure 5.3: Results of the color edge detection on a synthetic image with nine uniform chromatic regions and a variation of intensity. (a) Original color distribution, (b) lower intensity central square, (c) Prewitt detection on RGB bands, (c) our approach in equation (8.2).

Final results are given on a natural image, shown in Fig. 5.5. This image contains many color regions, with specular reflections, shadows and light effects. Fig. 5.6 shows the results of the linear operators based on the Sobel and Prewitt masks. Besides the lower response of the Prewitt operator, it can be appreciated the high sensitivity to specular reflections and low color constancy. All bright spots are interpreted as color edges. In the Fig. 5.7 we show the results of our approach under two variations of the neighborhood considered. The 4 neighborhood follows the same pattern of Eq. (8.2) but over a reduced set of neighboring pixels. Again our approach is very robust against specular reflectance. Bright spots do not appear to be detected. Dark regions of the image are equalized in their results relative to brighter regions. A very significative result is the detection of color edges even in the almost black background. A drawback that appears in our approach is the high spurious detection in the black background. This is due to the high angular variations induced by noise. It could be avoided by a simple intensity thresholding.

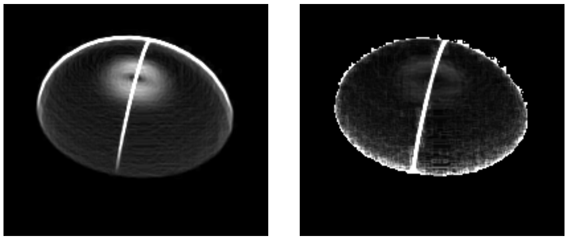

(a) (b)

Sobel

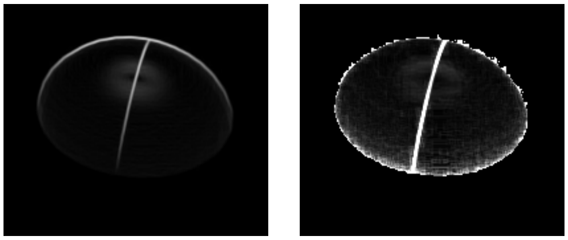

(c) (d)

Prewitt

Figure 5.4: Color edge on the synthetic image of Fig.5.2(a) with two color regions. (a) The Sobel operator over the RGB bands with specular component, (b) our approach in a Sobel-like structure, (c) the Prewitt linear operator, (d) our approach in a Prewitt like structure.

Figure 5.5: Natural image

(a) (b)

Figure 5.6: Results of the linear operators on the natural image (a) Sobel detector, (b) Prewitt detector

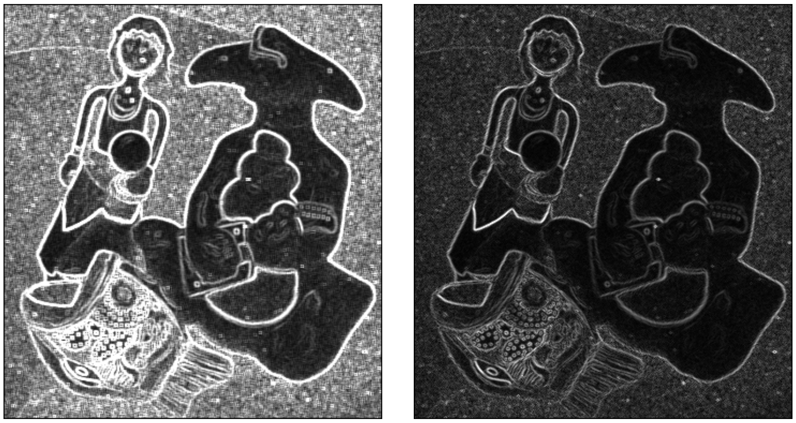

(a) (b)

Figure 5.7: Results of our approach on the natural image (a) taking 8 neighbors, (b) taking 4 neighbors

5.5 Conclusions

This chapter presents an innovative chromatic gradient computation, which has some Color Constancy properties, giving good detection of Color Edges. The method is grounded in the DRM which is a widely accepted image model for reflectance analysis. The method is intensity invariant, and, thus, is robust against the bright spots of specular reflections. It does not imply or need color segmentation, on the contrary can provide good color region separation with little assumptions. It works on the RGB space, which the most common color processing space.

Chapter 6

Color Image Segmentation Contributions

In this chapter we deal with color image segmentation using the chromatic decomposition defined in previous chapters. The chapter contains results from two different points of view: region growing and Watershed Transformation. The region growing segmentation method makes use of the chromatic distance defined on the spherical representation of the color coordinates, enriched with an hybridization that improves the results in the dark regions of the image, working on a 4-NW neighborhood in order to speed-up computations. The watershed based segmentation uses a hybrid gradient defined on the spherical coordinates, as an improvement to the gradient operator defined in the previous chapter. Both approaches have been tested on well know benchmark images. Both methods' hybridization consists in shifting to work with scalar intensity based distances and gradients to better deal with the noise in dark image regions.

Section 6.1 presents a region growing segmentation algorithm. Section 6.2 gives experimental results of this algorithm on benchmark images. Section 6.3 introduces the Watershed Transformation. Section 6.4 presents a new watershed segmentation algorithm based on the chromatic gradient. Section 6.5 gives experimental results of this approach. Finally, Section 6.6 gives the conclusions of the works presented in this chapter.

6.1 Chromatic Region Growing

This section presents a region growing image segmentation algorithm working on the spherical interpretation of the RGB color space. The algorithm uses a hybrid chromatic distance inspired in the human vision system (HSV) that shifts its emphasis from the chromatic to the grayscale distance depending on the pixel's luminance value. For dark areas, the chromatic distance is too much unstable so that the gray scale distance is used instead. Color constancy properties of this segmentation can be easily deduced from the dichromatic reflection model (DRM). The segmentation doesn't need preprocessing steps, such as illuminant source color estimation. The approach is strongly robust regarding highlights and dark spots, and it is amenable to work in real time on a robotic platform. We give results on benchmark databases and robot camera images. A public implementation is made available for independent test of the algorithm image segmentation results. We assign one region label to each and all image pixels, where each label corresponds to a connected region characterized by a chromaticity vector, which is computed along with the segmentation. Therefore, two separated regions with the same chromatic representation will have two different labels. The algorithm's output are a bi-dimensional matrix of integer labels and a bidimensional matrix of chromatic vectors corresponding to the identified image regions.

We introduce a new hybrid distance to measure the similarity between pixel colors, which is used in a one-pass pixel region labeling algorithm. This hybrid distance is a mixture of an intensity difference and a chromatic distance based on the spherical representation of the RGB color space, inspired in the sensitivity of the HSV. Its definition allows to parameterize the algorithm's noise tolerance, and to tune it for optimal color edge detection. Furthermore, it is easy to see that the chromatic component of this distance has some inherent color constancy, analyzing its behavior under the dichromatic reflection model (DRM). The labeling algorithm uses only the four north-west (4-NW) topological neighbors of the current pixel, because it process each pixel onces and does not perform any spatial relaxation processes. According to [49] "the image segmentation problem is basically one of psycho-physical perception, and therefore not susceptible to a purely analytical solution". The parameters of the mixture of the hybrid distance allow a fine tuning of the algorithm to the characteristics of the image being segmented. To allow for independent test of our algorithm we make available[1] a C# implementation, using Emgu [2] running on windows platforms.

6.1.1 The chromatic distance

Image segmentation detects an edge between two neighboring pixels when they have different color properties [60]. The simplest edge detectors are based on spatial gradients of the image intensity, i.e. the Sobel or Prewitt convolution kernels. These approaches ignore the chromatic information leading to poor color edge detection. To improve this approach, the convolution masks can be extended to color representations using hybrid distances [99]. The core of all edge detection methods is the definition of an appropriate distance between pixel colors.

According to the DRM model, the diffuse image component is expressed by the angular components (θ, ϕ), which are almost constant in regions with homogeneous chromatic properties. It is independent of the luminosity coordinate, therefore independent of the illumination assuming an uniform chromatic illumination. If we use only the diffuse component for edge detection, black-white borders may be undetected because both colors belong to the same achromatic line, and hence they have the same chromaticity. On the other hand it is important to avoid the effect of highlights, because they do not correspond to a true surface. Fig.6.1 illustrates the problem of false image regions in the image due to highlights that do not correspond to real objects in the scene.

Figure 6.1: Image with highlights

---

[1] http://www.ehu.es/ccwintco/index.php/Hybrid_Image_Segmentation. In the sources, the method name corresponding with this paper is “fastSegmentation2”

[2] http://www.emgu.com/wiki/index.php/Main_Page

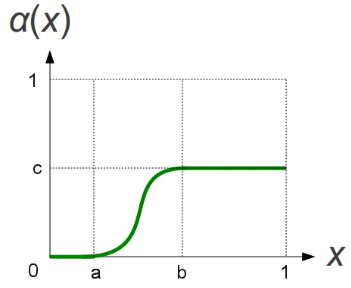

Figure 6.2: Chromatic activation function $\alpha(x)$

Fortunately, some differences exist between image edges due to highlights and those due to true boundaries between diffuse color surfaces. When two surface regions of different chromatic properties are adjacent, this chromatic difference is clear and detectable measuring the difference on the zenithal and azimuthal angles of the spherical representation of pixel colors. In the highlights, the chromaticity of pixels changes smoothly, so it is possible to filter out false edge detection setting a threshold on the chromatic distance based on the diffuse color component. For the human vision system, the main difficulty is to detect a color accurately in dark regions. In fact, chromaticity in dark regions is very unstable because it amplifies small color perturbations due to noise. According to the human vision system, in regions with poor illumination it is more appropriate to use the luminance component. In the human eye's retina we have two kind of photoreceptor cells; rods and cones. The first one is an luminance detector and the other one is a chromatic detector. Both need different energy for his activation. Rods need few energy for its activation, for this reason under poor illumination human vision becomes grayscale. Cones needs more energy, for this reason color are detected better with a good illumination.

Fig. 6.2 shows the activation function $\alpha(x)$ of the chromatic distance component of the proposed hybrid distance. For luminance values below a, the chromatic component of the distance is inactive, for intensity values in the interval $[a, b]$, we smoothly change the contribution of the chromatic component of the hybrid distance from zero to its maximum $c \leq 1$ according to a sinusoidal function. Finally, for intensity values above b its contribution is always c. The three parameters a, b, c are in the range $[0, 1]$.

The function $\alpha(x)$ on the image intensity defines the degree of mixing of the grayscale and chromatic distances. The Eq.6.1 is the mathematical expression of $\alpha(x)$:

$$\alpha(x) = \begin{cases} 0 & x \leq a \\ \frac{c}{2} + \frac{c}{2}\cos\left(\frac{(x-a)\cdot\pi}{b-a} + \pi\right) & a < x < b \ , \\ c & x \geq b \end{cases} \tag{6.1}$$

We define the hybrid distance between the color of two pixels p, q as follows:

$$d_H(p,q) = \left(1 - \alpha\left(\frac{l_p + l_q}{2}\right)\right) \cdot d_I(p,q) + \alpha\left(\frac{l_p + l_q}{2}\right) \cdot d_C(p,q), \tag{6.2}$$

where l_p, l_q are the intensity l in spherical coordinates of the pixels p and q, respectively, d_I is a grayscale intensity distance computed as $d_I(p,q) = |l_p - l_q|$, and d_C is the chromatic distance computed as

$$d_C(p,q) = \sqrt{(\theta_q - \theta_p)^2 + (\phi_q - \phi_p)^2}. \tag{6.3}$$

The foregoing Eq. (6.2) follows a human vision system inspiration, where the first term express the behavior of the rod retinal cells which are sensitive to intensity. They need few energy for its activation. On the other hand, the second term express the behavior of cone retinal cells which can detect chromaticity. They need more energy for its activation. The alfa function depends on the mean image intensity of the pixels being compared.

6.1.2 Proposed region growing segmentation method

The segmentation method proposed in this section combines the spherical interpretation of the RGB space and the aforegoing hybrid distance expressed in the Eq.(6.2). Edge detection can be accomplished applying a threshold on the distance between pixels. In order to decrease the computing time, we use a 4-WN neighborhood as illustrated in Fig.6.3. This structure allows to obtain acceptable results processing only once each pixel. This method travels over the image by rows, hence the 4-WN neighbors of a pixel are always labeled. Our segmentation method is explained by the following algorithm .

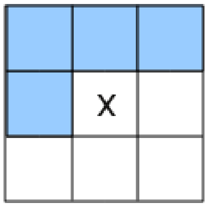

Figure 6.3: 4-WN Neighbors of pixel site x.

Algorithm 6.1 Support functions

```
function create_new_label(x)=
begin
    $L(x) = \text{newlabel}$. /create a new region label/
    $\Psi_{L(x)} = \Psi(x)$ . /update region label chromaticity/
end
function evaluate_neighbor(x)=
begin
/this function is used when there is only a neighboring label/
$d \leftarrow \min\{d_H(x,y)\,|y \in N_4(x)\}$
        if $d < \delta$ /some neighbor's color is similar enough/
            $L(x) = \ell$; /assign region label/
            $\Psi_\ell = \frac{1}{|R_\ell|}\sum_{y \in R_\ell} \Psi(y)$ /update region label chromaticity representation/
        else
            create_new_label($x$)
end
```

6.1.3 Algorithm

Algorithm 6.2 Image Segmentation Algorithm

```
Input: $\Omega(x)$ the color image in spherical coordinates
    Threshold $\delta$, distance parameters values $a, b, c$
-Initialize the pixel labels $\forall x; L(x) = \emptyset$
-The first region is composed of the first pixel $x_0 = (0,0)$: $L(x_0) = \text{newlabel}$.
The region chromaticity is that of the first pixel $\Psi_{L(x_0)} = \Psi(x_0)$.
for each $x$ do
    if $L_4(x) = \{\ell\}$ /there is only one region label in $N_4(x)$/
        evaluate_neighbor($x$)
    else
        $D \leftarrow \{d_C(L(y), L(z)) \mid y, z \in N_4(x) \;\&\; L(y) \neq L(z)\}$
        for all $D_i < \delta$ /region merging/
            $L(y) = \text{merge}(y, z)$ /merge both regions into $L(y)$ /
            $\Psi_{L(y)} = \frac{1}{|R_{L(y)}|} \sum_{y \in R_{L(y)}} \Psi(y)$ /update region chromaticity rep./
        end for
        if $L_4(x) = \{\ell\}$ /there is only one region label in $N_4(x)$/
                evaluate_neighbor($x$)
        else /regions can not be merged/
            $d \leftarrow \min\{d_H(x,y) \mid y \in N_4(x)\}$
            if $d < \delta$ /assign to region with the lower distance/
                $L(x) = L(y)$ s.t. $d_H(x,y) = d$;
                $\Psi_{L(x)} = \frac{1}{|R_{L(x)}|} \sum_{y \in R_{L(x)}} \Psi(y)$ /update region chromaticity /
            else /current pixel can not be assigned to existing regions/
                create_new_label($x$)
end for
```

This algorithm returns a bi-dimensional matrix of integer labels. While performing the computation, we also need to relate each label with a chromaticity and the amount of pixels labeled with it. That is necessary because each time that we assign a new pixel to a label we must update the label's chromaticity. The chromaticity of a label is the average chromaticity of all pixels labeled with it.

The most critical parameter of this algorithm is the distance threshold δ. The segmentation granularity and the noise tolerance depends on it. For small threshold values we obtain a lot of regions, and, conversely, with a high value we obtain few big coarse regions. On the other hand, the parameters

a, b, c of function $\alpha(x)$ as specified in Eq. (6.1) allow to tune the hybrid distance $d_H(p, q)$. In the limit cases, when $b = 0$ and $c = 1$ it becomes a pure chromatic distance. If $a = 1$ it becomes a pure intensity distance.

The Algorithm 6.2 gives the details of our method. In this algorithm $L(x)$ denotes the region label of pixel x, $L_4(x)$ denotes the set of labels of the 4-WN neighbors of pixel x, that can be expressed as $L_4(x) = \bigcup_{x' \in N_4(x)} L(x')$, where $N_4(x)$ the 4-WN neighborhood of pixel x illustrated in Fig. 6.3. The algorithm may be applied to any color image $\Omega(x)$ represented in RGB spherical coordinates. It needs the specification of the distance $d_H(x, y)$ that gives a measure of the similarity between pixel colors $\Omega(x)$ and $\Omega(y)$. We build a map $\Psi_\ell = (\theta_\ell, \phi_\ell)$ assigning to region labeled ℓ a chromatic value. We denote R_ℓ the current set of pixels labeled in region ℓ, $R_\ell = \{x \,\text{s.t.}\, L(x) = \ell\}$, the number of pixels in a region is its cardinality $|R_\ell|$. Function newlabel creates a new region label. Function merge $(\ell_1, \ldots, \ell_\text{n})$ creates as a side effect the union of the regions $R_{\ell_1} \cup \ldots \cup R_{\ell_n}$ relabeling pixels accordingly with a new created label ℓ, returning the new label as the function value. To avoid tedious repetition of multiple similar definitions of the distances when they applied to pixels or to region chromatic representations, the definition of the chromatic distance of Eq. (6.3) is extended to the case when two regions of labels ℓ_1 and ℓ_2 are the function parameters computing the distance over their chromatic representations Ψ_{ℓ_2} and Ψ_{ℓ_2} of as follows:

$$d_C(\ell_1, \ell_2) = \sqrt{(\theta_{\ell_1} - \theta_{\ell_2})^2 + (\phi_{\ell_1} - \phi_{\ell_2})^2}. \tag{6.4}$$

6.2 Chromatic Region Growing Results

In this section we present some computational results of the algorithm described in section 6.1.3. The algorithm's parameter are set to some nominal values: $\delta = 0.02$, $a = 0.2$, $b = 0.4$ and $c = 0.5$. According to these values, for the dark regions whose normalized intensity is less than 0.2 we use only the intensity distance, whereas for pixels with an intensity greater than 0.4 we use a hybrid distance where intensity and chromaticity have the same importance. In order to validate our approach, we have tested the proposed algorithm firstly with the well-known Berkeley database [100], and, secondly, with images obtained from the camera of a real robot Nao, Aldebaran Robotics, Paris, because we have developed the algorithm with robotic applications in mind. The main features of the images taken by the robot on-board camera are, (a) the low signal to noise ratio, due to the poor quality of this cameras, and (b) the appearance of many highlights in the images due to illumination sources of the real environment where the robot is working. For a visual assessment of the results, the output images are pictured using the mean color image of each region.

6.2.1 Results on the Berkeley database

Fig.6.4 shows the segmentation results on some images from the Berkeley image database [100]. The first row show original pictures as provided with the database. The second row shows segmentation results using the chromatic distance of Eq. (6.3). We present results using the hybrid distance of Eq. (6.2) in the third row. Comparison of images in those rows show the improvement obtained using the hybrid distance, obtaining more natural segmentations, specially in shadowy regions, like the tree or the sky in the right-most image. Smooth regions in the images are identified as homogeneous regions despite small color fluctuations and brightness. The fourth row shows the edges between regions identified in the images of the third row. Fifth row shows the human segmentation provided with the Berkeley data-set. Comparison between these edge images must take into account that the human edge delineation is an idealization of the actual image, drawing regions whose identification involve semantic processing of the image. Nevertheless, our approach captures most of the salient image partitions. Small detail edges appear in regions with randomized textures such as the tree, forest or rocky soil. Notice that in the chromatic images of the third row this over-segmentation is less apparent, suggesting that post-processing the chromatic segmentation image those textures could be removed if desired. Smooth regions, like the river in the left-most image or the wave in the surf image are identified quite closely to the hand made edge delineations, minimizing spurious detection due to highlights. Finally, last row shows the result of a standard implementation of the Canny edge detection, as found in the Matlab image processing toolbox (threshold 0.05, sigma 0.2). The Canny edge detection is defined for grayscale images, therefore the edge detection needs a previous transformation of the image from RGB to grayscale.

Fig. 6.4 shows the results of the segmentation using the same parameters of the alpha function (a, b, c, δ) for all images, corresponding to a neutral setting so that the alpha function is rather symmetric. However, for some image these parameters may need further tuning to obtain a perceptually

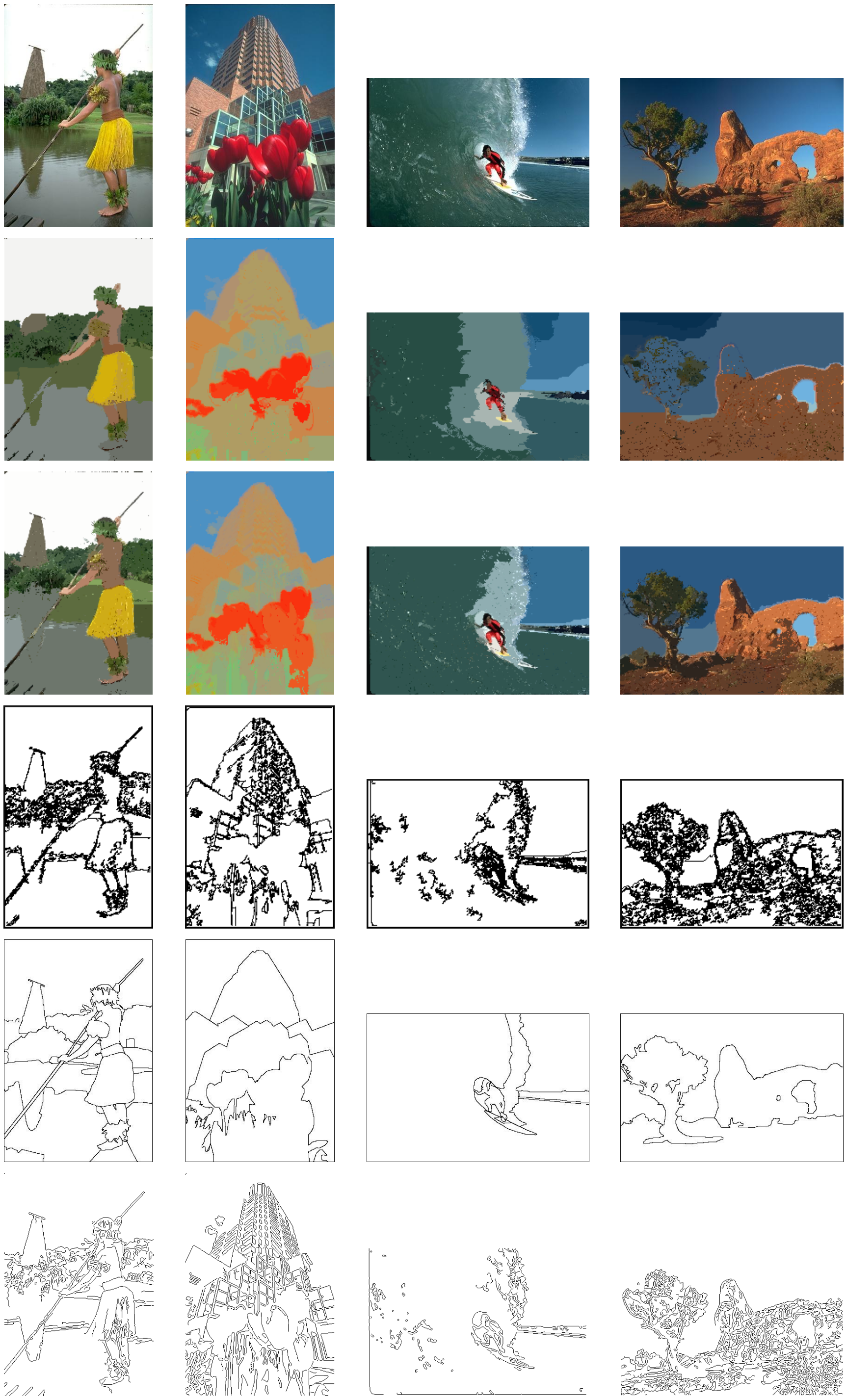

Figure 6.4: Segmentation of Berkeley data-set images.

Figure 6.5: Segmentation results obtained with interactive evolutionary optimized of the alpha function parameters.

correct segmentation. We do not have a direct quantitative measure of the segmentation quality, neither we have an expression relating the change of parameters, but we it is easy to obtain the desired segmentation tackling with the parameters. Therefore, we have embedded our segmentation in an interactive evolutionary algorithm [101], which provides good quality segmentations in a few iterations. The underlying evolutionary strategy is a conventional $(\lambda + \mu)$-ES [102] where each individual corresponds to a parameter setting, the fitness value of each individual is provided by the user by filling a Likert scale associated to each image obtained after segmentation with the corresponding parameter value settings.

Fig.6.5 shows the experimental results of this approach on the images of the left columns of Fig. 6.4. In the case of the first image the values found are: $a = 0.1, b = 0.2, c = 0.5, \delta = 0.025$. Notice the improvement in the segmentation of the river reflection of the hut in the background. In the case of the second image, values found are: $a = 0.1, b = 0.3, c = 0.8, \delta = 0.015$. Notice the improvement of the segmentation of the tulips stems, which were confused in Fig. 6.4.

6.2.2 Results on NAO's camera images

The images obtained from the Nao robot's camera are characterized by strong illumination effects and high noise ratios due to the poor camera quality and robot motion. In Fig. 6.6 we show the segmentation results for some original images. The left column shows the original images. The second column shows the color region segmentations, and the third column shows the edges between identified regions. Fourth column shows the result of a standard implementation of the Canny edge detection (parameter settings are threshold 0.05, sigma 0.15). Comparing them with the third column we can see than our method presents better results, regarding to the edge detection and avoiding the specular highlights. The most salient feature of the segmentation results obtained on these images is that most of the highlights on the floor are not identified as distinct image regions and the object shadows are ignored as well. All the segmented regions correspond to actual objects in the scene. For robotic applications, this robustness may be critical for task accomplishment. Although it was not the main goal of our work at this point, to obtain real time performance (of the order of 50 milliseconds per image) we downsampled the images to 80×60 pixels. This experiment has been carried out in a laptop with a processor Intel Core i3 M330 with 4GB of memory. The code has been written in C#.

In most cases the proposed segmentation shows a good behavior despite of some incorrectly detected regions. That's the case of the shadow of the red ball on the second row. The balls are hollow and translucent, thus when the ball is strongly illuminated the light is filtered across it, and the resulting shadow is heavily tinted by the ball color. In the case of the red ball, the shadow's colour is quite different from the surrounding floor color.

6.3 Watershed Transformation

The Watershed Transformation is a powerful mathematical morphology technique for image segmentation. It was introduced in image analysis by Beucher and Lantuejoul [43], and many algorithm variations and applications have been proposed subsequently [103, 41, 61].

The Watershed Transformation regards an image as a topographic relief map, where the gray level value of a pixel is interpreted as its elevation. The

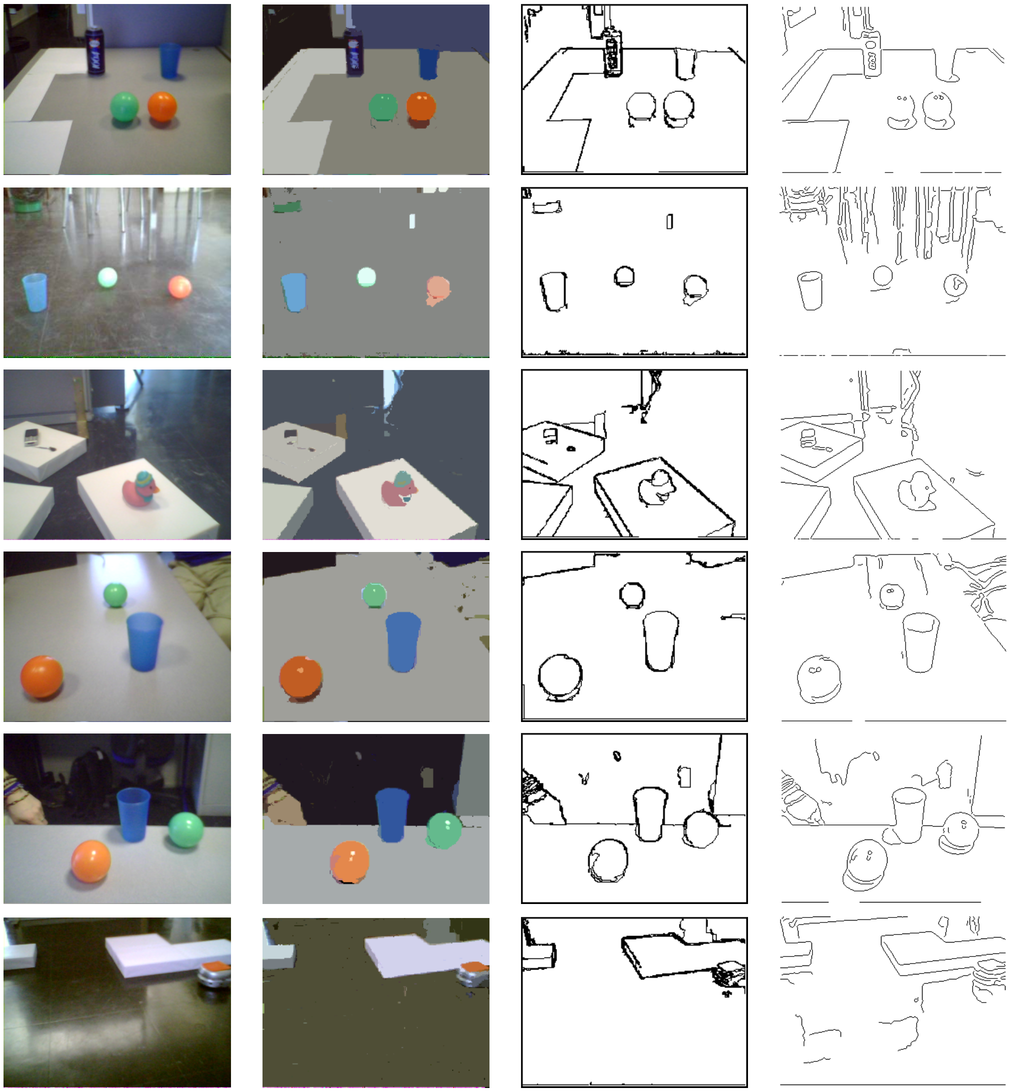

Figure 6.6: Segmentation of the images captured by the Nao Robot camera, performed using the hybrid distance of Eq. (6.2). The first (leftmost) column shows the original images, the second column shows the regions detected, the third column shows the boundaries between regions, and the last column shows the edges computed by the Canny edge detection algorithm.

watershed lines divide the image into catchment basins, so that each basin is associated with one local minimum in the topographic relief map. For image segmentation, the Watershed Transformation works on the image's spatial gradient magnitude. The crest lines in the gradient magnitude image correspond to the edges of image regions.

The baseline Watershed Transformation computation algorithm is as follows. The local minimum gradient pixel sites are selected as the sources of their respective catchment basins. A flooding process fills each catchment basin from its respective source. When a catchment basin is full, the contour points which are in touch with a neighbor catchment basin are identified as the watershed points. The process is finished when all the image gradient domain is covered. The closed lines defined by the watershed points give us the Watershed Transformation, and, implicitly, the image domain partition into regions. Usually, this partition is very fine, therefore a subsequent step of region merging is needed to obtain partitions closer to the natural segmentation of the image. Region merging needs the specification of the conditions for merging two neighboring catchment basins into a single region. In other words, the region merging criterion defines which watershed lines are removed. Watershed regions are image regions with homogeneous properties. The aforegoing defined hybrid chromatic gradient ensures that its basins correspond to homogeneous chromatic regions.

6.3.1 General Watershed Transformation

The general algorithm of the watershed method follows a flooding process which performs a region growing based on the ordered examination of the level sets of the gradient image. In fact, an ordered succession of thresholds are applied to produce the progression of the flooding. The image is examined iteratively n times; at each iteration step the threshold is raised and pixels of the gradient image below the new threshold are examined to be labeled with a corresponding region. Initially each region will contain the source of its catchment basin when the flooding level reaches it. Each flooded region is also characterized by a chromaticity value, corresponding to the source pixel chromaticity. This chromaticity value is used to perform region merging simultaneously with the flooding process. A pixel whose neighboring pixels belong to different regions is a watershed pixel. When a watershed pixel is detected, the adjacent regions may be merged into one if the chromatic distance between the region chromatic values is below a chromatic threshold.

The merged region chromatic value is the average of that of the merged regions. The final labeling of the image regions is performed taking into account the equivalences established by the merging process. Watershed pixels whose adjacent regions do not merge into one are labeled as region boundary pixels and retain their chromaticity.

The Algorithm 6.3 gives the details of this general algorithm. In this algorithm, $L\left(x\right)$ denotes the region label of pixel x, $L_8\left(x\right)$ denotes the set of labels of the 8 neighbors of pixel x, which can be expressed as $L_8\left(x\right) = \bigcup_{x' \in N_8(x)} L\left(x'\right)$, where $N_8\left(x\right)$ the 8-th neighborhood of pixel x. The algorithm can be applied to any color image $\Omega\left(x\right)$ and gradient magnitude image $\Phi\left(x\right)$. The algorithm needs the specification of a chromatic distance $\Delta\left(\Omega\left(x\right), \Omega\left(y\right)\right)$ that gives a measure of the similarity between pixel colors $\Omega\left(x\right)$ and $\Omega\left(y\right)$. To label the regions we keep a counter R, and we build a map Ψ_R assigning to each region label a chromatic value. While the flooding process performs region growing, the region chromatic value is updated to the average chromaticity of the pixels in the region. Each region R has a corresponding chromatic value Ψ_R which can be used for visualization.

6.4 A Robust Chromatic Watershed Transformation

The representation of the RGB color space points in spherical coordinates allows to retain the chromatic components of image pixel colors, discarding easily the intensity component. This representation allows the definition of a chromatic distance and a hybrid gradient with good properties of perceptual color constancy. In this section we present a watershed based image segmentation method using using this hybrid gradient. Over-segmentation is solved by applying a region merging strategy based on the chromatic distance defined on the spherical coordinate representation. We show the robustness and performance of the approach on well known test images and the Berkeley benchmarking image database.

Color images have additional information over grayscale images that may allow the development of robust segmentation processes. There have been works using alternative color spaces with better separation of the chromatic components like HSI, HSL, HSV, Lab [104, 57] to obtain perceptually correct image segmentation. However, chromaticity's illumination source can blur

Algorithm 6.3 General algorithm of watershed and region merging for color image segmentation.

```
Set number of iterations $n$, the chromatic distance threshold $\delta$, initialize the pixel labels $\forall x; L(x) = \emptyset$, the region label counter $R = 0$,
$\Omega(x)$ is the color image, $\Phi(x)$ is the gradient magnitude image.

1. Calculate $\Phi_{\min} = \min_x \{\Phi(x)\}$ and $\Phi_{\max} = \max_x \{\Phi(x)\}$. Calculate the step at each interaction $s = (\Phi_{\max} - \Phi_{\min}) / n$
   Initialize $t = \Phi_{\min}$;
2. Iterate $n$ times, setting
   (a) Calculate threshold $t = t + s$.
   (b) Consider $X'(t) = \{x' \,|\Phi(x') < t\}$, for each $x \in X'(t)$ perform:
       i. If $L(x) = \emptyset$ the pixel is unprocessed, then one of the following cases apply
          A. If $L_8(x) = \emptyset$
             - Assign new label $R \leftarrow R + 1$; $L(x) = R$.
             - Assign the region chromatic value $\Psi_R = \Psi(\Omega(x))$.
          B. If $|L_8(x)| = 1$
             - $L(x) = L_8(x)$
             - Update $\Psi_{L(x)}$ using $\Psi(\Omega(x))$.
          C. If $|L_8(x)| > 1$ there are at least two adjacent regions, $x$ is a gradient watershed pixel. Consider all pairs of adjacent regions of labels $r_1$ and $r_2$
             - If $\triangle(\Psi_{r_1}, \Psi_{r_2}) \leq \delta$ then we can merge both regions into one of label $r^*$. Compute $\Psi_{r^*} = \left(\frac{|r_1|\Psi_{r_1} + |r_2|\Psi_{r_2}}{|r_1| + |r_2|}\right)$. We keep record of the detected equivalence. Update $\Psi_{r^*}$ using $\Psi(\Omega(x))$. $L(x) = r^*$.
             - If $\triangle(\Psi_{r_1}, \Psi_{r_2}) > \delta$ the pixel $x$ is a region boundary pixel with a special label $L(x) = b$.
3. From the recorded label equivalences compute the final region labels, and assign definitive labels.
4. Each region $R$ has a corresponding chromatic value $\Psi_R$ which can be used for visualization
```

and distort color patterns. Image segmentation methods based on spatial gradients need a correct definition of the spatial color gradient and unambiguous contour definition. In fact, formulation of watershed segmentation methods in color images is still an open research issue. A straightforward but inexact approach is the independent application of the watershed segmentation on each image channel [103]. This approach loses chromatic information, and has difficulties merging the subsequent independent segmentations into one.

In this section we will use the RGB spherical coordinates representation to archive color constancy properties of our image segmentation approach [99, 96, 89]. We define a chromatic distance on this representation. The robustness and color constancy of the approach is grounded in the dichromatic reflection model (DRM) [37]. We propose a chromatic gradient operator suitable for the definition of a Watershed Transformation on color images and a robust region merging for meaningful color image segmentation. The baseline chromatic gradient operator [99, 89] suffers from noise in the dark areas of the image. We propose in this chapter a hybrid gradient operator overcoming this problem and we use it to build a watershed transformation on color images. To achieve a natural segmentation, we perform region merging on the basis of our proposed chromatic distance over the chromatic characterization of the watershed regions. We give a general algorithm that combines watershed flooding with region merging in a single process. Finally, we specify our proposal as an instance of the aforementioned general algorithm.

6.4.1 Gradient operators

Here, we recall the **chromatic** gradient definition presented on the previous chapter. The row pseudo-convolution is defined as

$$CG_R\left(P\left(i,j\right)\right)=\sum_{r=-1}^{1} d_C\left(P\left(i-r,j+1\right),P\left(i-r,j-1\right)\right),$$

and the column pseudo-convolution is defined as

$$CG_C\left(P\left(i,j\right)\right)=\sum_{c=-1}^{1} d_C\left(P\left(i+1,j-c\right),P\left(i-1,j-c\right)\right),$$

where d_C is the chromatic distance of Eq. (6.3). So, the color distance between pixels substitutes the intensity subtraction of the Prewitt linear operator. The color gradient image is computed as:

$$CG(x) = CG_R(x) + CG_C(x) \tag{6.5}$$

The **intensity** gradient definition is as follows: The row pseudo-convolution is defined as

$$G_R(J(i,j)) = \sum_{r=-1}^{1} \|J(i-r, j+1) - J(i-r, j-1)\|,$$

and the column pseudo-convolution is defined as

$$G_C(J(i,j)) = \sum_{c=-1}^{1} \|J(i+1, j-c) - J(i-1, j-c)\|,$$

where J is the intensity image, then the intensity gradient image is computed as:

$$G(x) = G_R(x) + G_C(x) \tag{6.6}$$

6.4.2 Hybrid gradient

Empirical experiments show that the chromatic gradient of Eq. (6.5) is very sensitive to image noise. The angular distance of Eq. (6.3) is more sensitive to noise for pixel colors lying close to the origin in RGB space. This is due to the fact that the angular distance between two points at a given euclidean distance grows as the points are closer to the origin. Small perturbations as measured by the euclidean distance are mapped into big angular differences. The background noise which has little effect in well illuminated regions is amplified in the dark regions.

Inspired in human vision system, we propose a hybrid gradient which is an intensity gradient when the illumination is poor, and a chromaticity gradient in better illuminated image regions. For intensity values below a threshold a it is an intensity gradient, for values above another threshold b it is a chromatic gradient, and for values between both it is a mixture of the two kinds of gradients whose mixing coefficient is sinusoidal function of the image

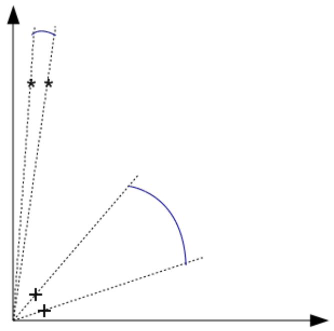

Figure 6.7: Effect of distance to the origin in the angular distance for pairs points at the same euclidean distance.

intensity. This idea is expressed mathematically as a convex combination of the two gradient operators:

$$HG(x) = \beta\,(x)\,G\,(x) + \overline{\beta}\,(x)\,CG\,(x) \tag{6.7}$$

where x is the pixel location, $G(x)$ is the intensity gradient magnitude of Eq.6.6, $CG(x)$ is the chromatic gradient of Eq.6.5 and $\overline{\beta}(x) = 1 - \beta(x)$, $\beta(x)$ is normalized to the range $[0, 1]$.

$$\beta(x) = \begin{cases} 1 & I(x) < a \\ \frac{1}{2} + \frac{\cos(\frac{x-a}{b-a}\pi)}{2} & a \leq I(x) < b \\ 0 & b \leq I(x) \end{cases}, \tag{6.8}$$

where $I(x)$ is the pixel intensity.

Note that by difference with the α mixing function presented in the previous work, this β function does not have a lower bound $c > 0$, therefore the hybrid gradient is either a chromatic gradient or an intensity gradient except in the range $[a, b]$. Fig.6.8 shows the activation of the intensity gradient depending of the intensity.

Fig.6.9 shows the response of different gradient operators on the same test image. Fig. 6.9(a) presents the original image. Fig. 6.9(b) contains the response of the intensity gradient, it shows false border detection in some

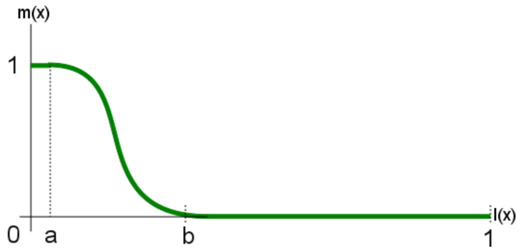

Figure 6.8: Hybrid gradient convex combination factor as a function of the image intensity.

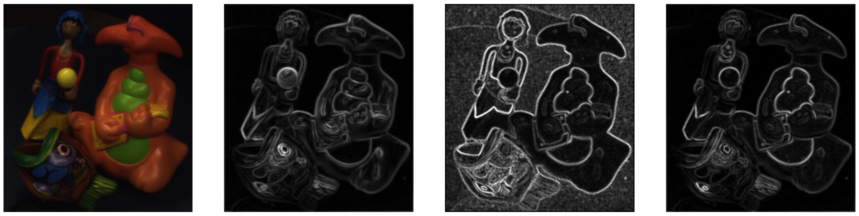

(a) (b) (c) (d)

Figure 6.9: Response of different gradient operators. (a) original image (b) intensity gradient, (c) chromatic gradient, (d) hybrid gradient.

diffuse regions, i.e. the yellow ball, green thorax. It also shows false edge detection in bright spots. Fig.6.9(c) shows the response of the chromatic gradient operator. It does not give false edge detection inside diffuse regions. It does not give false edge detection in bright spot areas. However, it is very sensitive to noise in the dark regions, showing false edge detections due to small random variations. Fig.6.9(d) presents the response of the hybrid gradient which has the good detection properties of the chromatic gradient operator and it is not sensitive to noise in the dark image regions.

6.4.3 The proposed approach

Our color image segmentation process proposal can be precisely specified by Algorithm 6.3 applied on the zenithal and azimuthal angles of the spherical color representation of the image, computing the gradient magnitude image by the hybrid gradient $HG(x)$ of Eq.(6.7), using the chromatic distance of Eq.(6.5). The algorithm does not compute any specular free image to remove highlights.

6.5 Experimental results

The watershed-merge Algorithm 6.3 is parametrized by:

- The number of iterations n, which determines the resolution of the flooding process going over the gradient magnitude image level sets.
- The gradient operator used to compute the gradient magnitude image, which can be either the intensity gradient $G(x)$ of Eq. 6.6 or the hybrid gradient $HG(x)$ of Eq.6.7.
- The color representation of the image. Assuming the RGB space, it can be either the Cartesian representation $\mathbf{I}(x)$ or the zenithal and azimuthal angles of the Spherical representation $\mathbf{P}(x)$. This selection determines the selection of the chromatic distance.
- The Chromatic distance, which can be either the Euclidean distance in the RGB Cartesian space, or the chromatic distance of Eq.6.3.
- The Chromatic distance threshold δ, which determines the chromatic resolution of the region merging process.

This section reports results of two experiments, the first one compares our proposal of section 6.4.3 with other instances of the algorithm, whereas in the second one we will to provide a more extensive qualitative validation our method using the well know Berkeley benchmark image collection[100] which provides hand-draw artistic shape boundaries.

6.5.1 First experiment

In this section we will use a well known benchmark image [91] to compare our proposed segmentation process with variations of Algorithm 6.3 obtained with several parameter settings. The dark regions are critical to the perceptually correct gradient computation, while the bright spots may induce false edge detection.

The operational parameter setting are $n = 100$ and $\delta = 0.1$. In Fig.6.10 we show the segmentation results on this image for all combinations of the

Original image

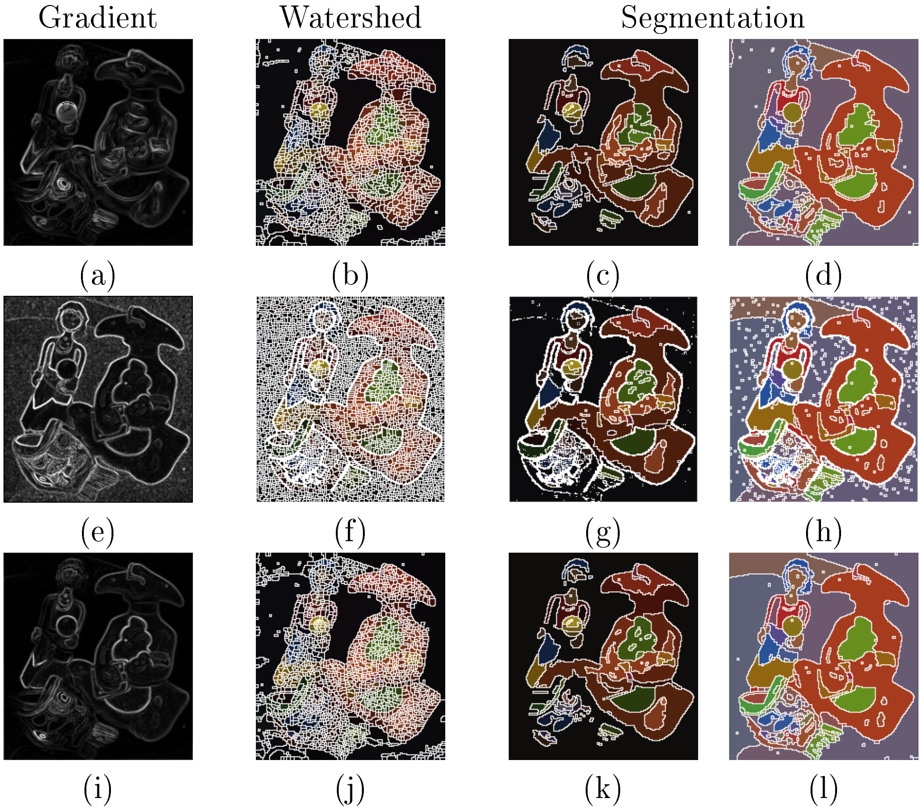

(a) (b) (c) (d)

(e) (f) (g) (h)

(i) (j) (k) (l)

Figure 6.10: Image segmentation results with different parameterizations of Algorithm 6.3.

remaining Algorithm 6.3 parameter settings. The column of images labeled “Gradient” has the gradient magnitude images. From top to bottom, Fig.6.10(a), 6.10(e), 6.10(i) show, respectively the result of the intensity gradient, the chromatic gradient of equation Eq.(6.5), and the hybrid gradient of Eq.(6.7). The column of images labeled “Watershed” correspond to the image region partition performing only to the flooding process, without any region merging, on the corresponding gradient magnitude images. It can be appreciated that the hybrid gradient watershed removes most of the dark microregions originated by the chromatic gradient. There are, however, some regions with different colors in this rough dark region which are not fully identified by the intensity gradient watershed of Fig.6.10 (b) and are better detected by the hybrid gradient watershed in Fig.6.10(j). The two image columns with the heading “segmentation” show the results of the region merging from the corresponding gradient watershed in the same row. The left column shows the results of using of the Euclidean distance on the RGB Cartesian coordinates. The right segmentation column show the results of the using the chromatic distance of Eq. (6.3). If we want to ascertain the effect of the color representation and the chromatic distance we must compare the rightmost columns in Fig.6.10. We find that the general effect is that the chromatic distance on polar coordinates is better identifying the subtle color regions in the darkest areas of the image, it detects better the shape of the objects, has better color constancy properties, and it is much less sensitive to bright spots or shining areas. Comparing the gradient operators attending to the final segmentation we observe that the hybrid gradient is better than the others in removing noise from the dark regions and maintain the object integrity. Overall the best result is obtained with our proposal as shown in Fig.6.10(l), where we can easily identify the subtle regions in the upper dark area, the shadow of the lowermost object, and we can clearly identify object with the same color unaffected by shading and bright spots.

6.5.2 Validation on the Berkeley images

In the Fig.6.11 we can show the experimental results using the Berkeley collection of images [100]. The first and fourth rows shows the original images, the second and fifth shows our respective outputs, whereas the third and sixth rows shows the human segmentation reference. As we can see our method gives always homogeneous regions, and the segmentation output is close to the human segmentation. Some facts that we find comparing our segmentation with the hand-drawn segmentation:

- Large chromatically smooth regions are well segmented by our approach despite variations in intensity, e.g. the face skin of the portrayed man, the river, the road in the road race image.
- Some subtle chromaticity variations are detected and segmented, like the reflections in the water of the jungle river image.
- The algorithm does not use any spatial information to segment textured objects. However it can cope with some textured spatial intensity variations of chromatically constant regions, outlining the corresponding object, i.e. the clouds in the flying plane image, the yellow skirt in the jungle river image.
- The hand-draw contours obviate some regions of the image that the artist may have found irrelevant, i.e. the clouds in the sky in some images, the texture details of some bushes. Some of these regions can not be segmented as a unit unless some spatial texture information is used, like the bushes in the jungle river image, or the skyscraper windows.

6.6 Conclusions

In this chapter we have presented two innovative image segmentation methods having in common to be grounded on DRM and their use of a spherical coordinate representation of the RGB color space. The chromatic distance used endows the approaches with good color constancy properties, avoiding the effect of highlights and shadows, though they are specially sensitive to noise in very dark image regions. To overcome this sensitivity, we have defined hybrid versions of the chromatic distance and gradients, mixing them with the conventional grayscale differences and gradients following the inspiration of the human vision system. Hybridization parameters can be tuned to optimize segmentation for different image conditions.

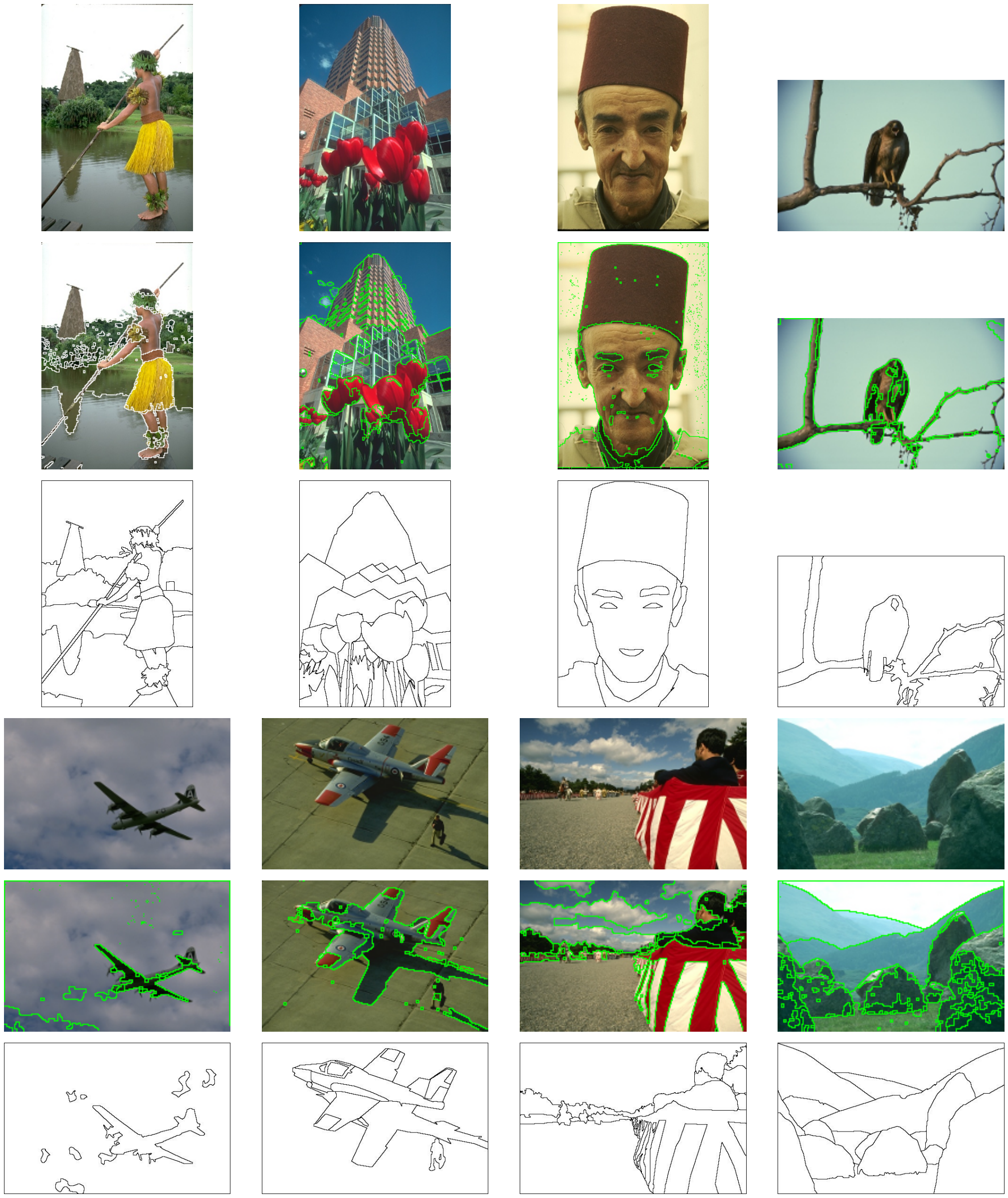

Figure 6.11: Segmentation results on some of the Berkeley images. Second and fourth rows show the results of our approach. Third and last row show the hand-drawn shapes.

Region Growing: It is a one-pass method which can achieve real time performance for small images. It doesn't need an image preprocessing for edge detection contrary to other approaches. It avoids spurious region detection due to highlights produced by illumination, detecting color edges with a physical interpretation as boundaries of surfaces with different reflectances. Regarding real-time performance, current experiments on the NAO robot off-loading the image segmentation to an auxiliary workstation give real-time responses for small image frames (20 frame/second).

Watershed and Region Merging Segmentation: A robust hybrid chromatic spatial gradient is used to realize a robust chromatic watershed segmentation. This gradient operator has good color edge detection in lightened areas and does not suffer from the noise in the dark areas. The region merging is based on the defined chromatic distance. We compare our approach with other algorithms obtained with different setting of the general algorithm, obtaining the best qualitative segmentation. The results on the Berkeley database images find excellent approximations to the provided hand-drawn segmentations, without using spatial or semantic information.

Chapter 7

Hyperspectral Images

Colorimetric ideas are not applied on hyperspectral images. Images never are normalized with respect to the illumination, therefore an uniform illumination is assumed. Reflection is different depending of the season of the year, the satellite position coordinates and point of view. Moreover, earth is not a uniform surface, there are highlights and shadows due to occlusions and strong variations of reflectance properties. This chapter introduces the chromatic representations and tools discussed in previous chapters for RGB images to hyperspectral image processing, which help to solve the problem of highlights and shadows in segmentation processes. We formulate the Dichromatic Reflectance Model (DRM) for hyperspectral images in Euclidean coordinates and Hyperspherical coordinates.

This chapter is outlined as follows: Section 7.1 introduces hyperspectral images and their differences with RGB images. Section 7.2 reviews applications and state of the art. Section 7.3 introduces the Hyperspherical coordinates for hyperspectral image interpretation given a chromatic description. Section 7.3.2 formulates the DRM for hyperspectral images.

7.1 Hyperspectral Images

An image is a projection of an observed scene containing the effect of light reflection from the objects in the scene. Standard RGB images are specialized for human vision, catching only the visible spectrum (from $400nm$ to $780nm$), a tiny fraction of light spectrum. Current hyperspectral cameras have a sensitivity ranging from $100nm$ to $2400nm$.

Standard RGB sensors (such as conventional digital photographic cameras) are designed according to the human retinal behavior by using the Bayer filter. It means, that the *Red*, *Green* and *Blue* receptors of digital cameras are spatially distributed according to the human sensitivity for these colors. *Red*, *Green* and *Blue* sensitivity functions correspond to overlapping ranges of the visible spectrum. Therefore, a color doesn't corresponds exactly with a wavelength of the light spectrum, a color corresponds with a set of ranges within visible spectrum, besides these sets could be disjoint.

Hyperspectral cameras overcome the visual human perception resolution and range of wavelengths. The hyperspectral camera detection range is divided in n disjoint and contiguous intervals whose union give the full spectral range. The energy detected in the n-th section is saved into the n-th image band. Then, a band of a hyperspectral image has the image energy for the corresponding light wavelet interval, and the union of all bands of a pixel is gives the spectral pixel signature. Hyperspectral cameras provide images over hundreds of bands. Aforementioned ideas are drawn in Fig.7.1, where we can see the spectral range difference between a RGB image and a hyperspectral image. Note that in RGB images each channel correspond to overlapping filters whereas in hyperspectral images each band correspond to a little filter.

There are many and different hyperspectral cameras, e.g. for little labs, the company *Surface Optics* sells hyperspectral cameras like the SOC 710 capturing images in the wavelength range from $333nm$ to $900nm$ into 128 bands. Our research group has bought one such cameras, and some experimental images were obtained with it.

7.2 State of the Art

Hyperspectral images are used in a lot of topics. First applications were done in the field of mineralogy and in works on the restoration of historical manuscripts. Nowadays, their foremost application is in remote sensing for earth observation. The increased number of sensors, both airborne and on board of satellites, are make burgeoning the field of hyperspectral image processing. Here we will comment on some of the recent trends for computational methods and applications.

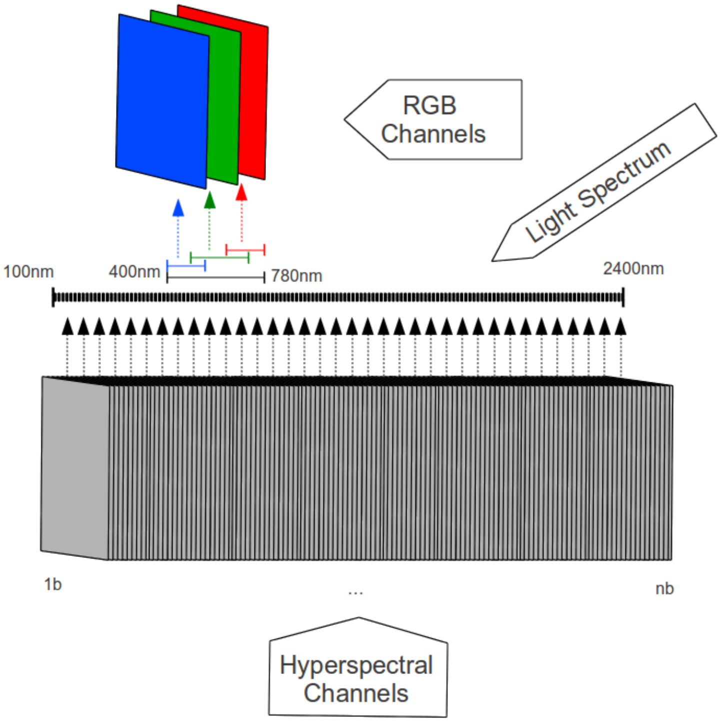

Figure 7.1: Schema of hyperspectral image

7.2.1 Computational methods

Classification and Machine Learning Hyperspectral images have more reflectance information than RGB images. Classification methods have in this images a perfect testing ground. In fact, all classification algorithms have been applied to build thematic maps on them in one moment or other. For instance, Artificial Neural Networks are applied for robust classification of the nutrition state in crop plants in [105]. A comparison of support vector machines, import vector machines and relevance vector machines is reported in [106] over a HyMap dataset. Support vector machines are applied too successfully for tree classification in the Southern Alps on high geometrical resolution airborne hyperspectral data [107].

Image Processing and Compression Image processing of hyperspectral imagery poses specific problems due to the high dimensionality of the data.

For instance, edge detection using tensor algebra is proposed in [108] in order to avoid false edges. Graph theory is applied for image clustering[109].

One of the unavoidable features of these images is their large size, therefore an important topic is the high performance computing for its processing and compression with minimal loss. In this way there are some relevant works too. For instance, unsupervised clustering is applied for hyperspectral image compression in [110]. A fast deconvolution of large fluorescence hyperspectral microscopic images is proposed in [111]. A novel architecture for real-time matching is proposed in [112] where the architectural design and hardware implementation of two hyperspectral matching algorithms (spectral angle and cross correlation) onto a Virtex-5 FPGA device with a speed up 600 faster than conventional software implementation.

Physical Modeling and Calibration Brook [113] proposes a full-chain process to extracting reflectance information from hyperspectral (HRS) data which is valid for all sensor qualities. This method is based on a mission-by-mission approach, followed by a unique vicarious calibration stage. Qian[114] describes a joint development of a compact and low distortion imaging spectrometer system for future Mars sample return mission and unmanned aerial vehicles under. A Dyson design was selected as the imaging spectrometer due to its compactness, high optical output and low distortion. Zang [115] presents a field imaging spectrometer system based on a cooling area CCD which shows huge potential applications in geology, food, agriculture, forestry and other respective field. Briottet[116] proposes a new hyperspectral sensor (HYPXIM).

7.2.2 Applications

There are a lot of applications of hyperspectral imagery. It is out of the scope of this thesis to review all of them, however we pick the foremost areas.

Mineralogy remote sensing Airborne hyperspectral data have been available to mineralogy researchers since the early 1980s and their use for geologic applications is well documented. Recently, a method for the automatic supervised detection of multiple mineral targets in hyperspectral mineral data is presented in [117]. This method method makes use of wavelet analysis, wavelet-based denoising using thresholding of wavelet detail coefficients, and feature reduction based on sequential forward selection, which utilizes an extension of receiver operating characteristic curves to fuzzy set membership in order to measure discriminating capability. Hyperspectral images have also a role in astrophysics [118, 119, 120, 121].

Forestry and oceans: In [122] helicopter on-board imaging spectroscopy is used for mapping species variation. Erins [107] has done a classification of individual trees to 5 conifer and deciduous species in mixed Baltic forest, based on processing of airborne hyperspectral and LiDAR data. Torrecilla[123] have done a sensitivity analysis of a follow up of phytoplankton biodiversity.

Industry and environment: There are applications for quality control, where in [124] is applied to polyolefins recycling. There are applications for petrol inspection tasks, like in[125] where authors try to separate bitumen from oil sand, and for chemical identification of pharmaceutical tablets [126].

Defense and security: There are also applications for surveillance purposes. The hyperspectral research has an increasing role for military aims (like endmember detection for hyperspectral unmixing). There are works about real-time hyperspectral data compression system for military goals[127]. Algorithms for autonomous Hyperspectral change detection [128]. And there are many works related with airborne strategies for surveillance in conjunction with other technologies like wireless, radar, SAR, CBRNE, and more [129]. Verancini[130] develops a spectral-based algorithm for automatic global anomaly detection consisting in a two stage process. First, the background Probability Density Function (PDF) is approximated through a data-adaptive kernel density estimator. Then, anomalies are detected as those pixels that deviate from such a background model on the basis of the Likelihood Ratio Test (LRT) decision rule. Bajorski[131] proposes a new type of a segmented matched filter, called a directional segmented matched filter (DSMF), based on geometric considerations between the target, background, and a given pixel.

Agricultural and ecological systems: Hyperspectral data also can provide significant improvements in spectral information content for detecting of early-stage vegetation stress, identifying small differences in percent green vegetation cover, discriminating land cover types, leaf pigment concentrations, modeling quantitative biophysical and yield characteristics of agricultural crops. Within remote sensing field, from the space are observed the growing and shrinking of forest, the evolution of burned regions and are followed up agricultural crops like soybean crops [132, 133, 134, 135, 136]. A study of the estimation of canopy chlorophyll and nitrogen content is done in [137]. Feret [138] has done a study of the performance of two supervised classifiers, linear and regularized discriminant analysis where these are compared for canopy species discrimination in humid tropical forest. Finally, a work for the estimation of fruit yield in citrus is done in [139].

7.3 Hyperspherical Coordinates and Chromaticity

Here we present the Hyperspherical representation of a hyperspectral image, extrapolating the idea of chromaticity to the hyperspectral domain. An n-sphere is a generalization of the surface of an ordinary sphere to an n-dimensional space. n-Spheres are named Hyperspheres when dimensionality is bigger then 3. We are interested in the hyperspherical representation of an hyperdimensional point and its implications for image segmentation under a chromatic point of view. In the RGB three-dimensional color space, Fig. 7.2 shows the spherical representation of a color point. A color c with (r, g, b) coordinate values in RGB color space can be represented by spherical coordinates (θ, ϕ, l), where θ and ϕ are the angular parameters and l the vector magnitude.

In the three-dimensional RGB color space, there is a direct correspondence between angular parameters (θ, ϕ) and chromaticity. The angular parameters define a line which is the natural characterization of the pixel chromaticity. In other words, all points on this line have the same chromaticity. The spherical expression of a point in Euclidean space allows to separate intensity and chromaticity, where l is the intensity, and the angular parameters provide a representation/codification of the pixel's chromaticity. These ideas can be extrapolated to n-dimensional spaces.

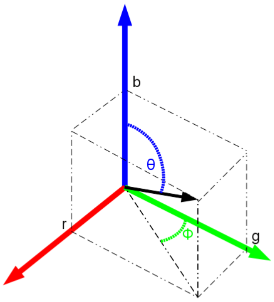

Figure 7.2: A vectorial representation of color c in the RGB space

7.3.1 Hyperspherical coordinates

Let us denote p a hyperspectral pixel color in n dimensional Euclidean space. In Cartesian coordinates it is represented by $p = \{v_1, v_2, v_3, ..., v_n\}$ where v_i is the coordinate value of the i-th dimension. This pixel can be represented in Hyperspherical coordinates $p = \{l, \phi_1, \phi_2, \phi_3, .., \phi_{n-1}\}$, where l is the vector magnitude that gives the radial distance, and $\{\phi_1, \phi_2, \phi_3, .., \phi_{n-1}\}$ are the angular parameters. This coordinate transformation is performed uniquely by the following expression

$$\begin{array}{c} l = \sqrt{v_1^2 + v_2^2 + v_3^2 + ... + v_n^2} \\ \phi_1 = \cot^{-1} \frac{v_1}{\sqrt{v_2^2+v_3^2+...+v_n^2}} \\ \phi_2 = \cot^{-1} \frac{v_2}{\sqrt{v_3^2+v_4^2+...+v_n^2}} \\ \vdots \\ \phi_{n-2} = \cot^{-1} \frac{v_{n-2}}{\sqrt{v_{n-1}^2+v_n^2}} \\ \phi_{n-1} = 2\cot^{-1} \frac{\sqrt{v_{n-1}^2+v_n^2} - v_{n-1}}{v_n} \end{array},$$

for all cases except the following exceptions: if $v_i \neq 0$ for some i but all of $v_{i+1}, \ldots, v_n$ are zero then $\phi_i = 0$ when $v_i > 0$. When all $v_i, \ldots, v_n$ are zero then ϕ_i is undefined, usually a zero value is assigned.

A more compact notation for the hipersphherical coordinates is $p = \{l, \bar{\phi}\}$, where $\bar{\phi}$ is the vector of size $n - 1$ containing the angular parameters. Given a hyperspectral image $\mathbf{I}(x) = \{(v_1, v_2, v_3, ..., v_n)_x ; x \in \mathbb{N}^2\}$, where x denotes the spatial pixel coordinates in the image domain, we denote the corresponding hyperspherical representation as $\mathbf{P}(x) = \{(l, \bar{\phi})_x ; x \in \mathbb{N}^2\}$, from which

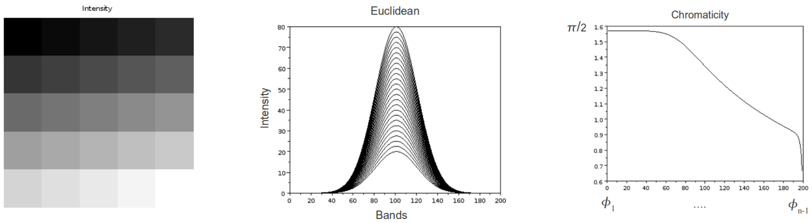

(a) (b) (c)

Figure 7.3: Synthetic image (a) the image intensity $\{l_x\}$, (b) shows the Gaussian shaped signature profile of all the pixels, and (c) shows the angle components of the hyperspherical coordinates shared by the spectral signatures of all pixels in the image, corresponding to the common chromaticity of the pixels.

we use $\bar{\phi}_x$ as the chromaticity representation of the pixel's and l_x as its (grayscale) intensity.

To clarify the meaning of the chromaticity in the hyperspectral image domain, we give an illustrative example. We have generated a synthetic hyperspectral image of 5 × 5 pixels and 200 spectral bands. Each pixel spectral signature has the same Gaussian shaped profile but with different peak height, corresponding to different image intensity as can be appreciated in Fig. 7.3(a) showing the image intensity $\{l_x\}$. Fig. 7.3(b) shows the spectral signature of all pixels in the Cartesian coordinate representation, Fig. 7.3(c) shows the chromatic spectral signature $\left\{\bar{\phi}_x\right\}$ which is the same plot for all pixels. The chromaticity $\bar{\phi}$ thus defines a line in the n-dimensional space of hyperspectral pixel colors of points that only vary their luminosity l.

According to the aforegoing coordinate transformation, we can accomplish the following hyperspectral separation. Given a hyperspectral image $\mathbf{I}(x)$ in the traditional Cartesian coordinate representation we can compute the equivalent hyperspherical representation $\mathbf{P}(x) = \left\{(l, \bar{\phi})_x; x \in \mathbb{N}^2\right\}$. Then, we can construct the separate intensity image $\mathbf{L}(x) = \left\{(l)_x; x \in \mathbb{N}^2\right\}$, and the chromaticity image $\mathbf{C}(x) = \left\{(\bar{\phi})_x; x \in \mathbb{N}^2\right\}$. In the synthetic example shown at Fig. 7.3, $\mathbf{I}(x)$ pixels are plotted in Fig. 7.3 (b), the spectral chromaticity $\mathbf{C}(x)$ in Fig. 7.3(c) and the image intensity $\mathbf{L}(x)$ in Fig. 7.3(a).

This separation allows us the independent processing of hyperspectral color and intensity information, so that segmentation algorithms showing color constancy can be defined in the hyperspectral domain. This decomposition can be also embedded in models of reflectance like the Dichromatic Reflection Model [37] of the Bidirectional Reflection Distribution Function where they can be decomposed as diffuse and specular components.

7.3.2 DRM for n-Dimensional images

DRM was presented for standard RGB images, it explains the perceived color intensity $I \in \mathbb{R}^3$ of each pixel in the image as the addition of two components, one diffuse component $D \in \mathbb{R}^3$and a specular component $S \in \mathbb{R}^3$. We will adapt it for multidimensional spaces. That is, $I \in \mathbb{R}^n$, $D \in \mathbb{R}^n$ and $S \in \mathbb{R}^n$. For the sake of clearness, we will refer them as I^n, D^n, S^n expressing the n-dimensionality. The mathematical expression of the model, when we have only one surface color in the scene, is as follows:

$$\mathbf{I}^n(x) = m_d(x)\mathbf{D}^n + m_s(x)\mathbf{S}^n, \tag{7.1}$$

where m_d and m_s are weighting values for the diffuse and specular components. Equivalently, Eq. (7.1) can be expressed it in Hyperspherical coordinates as:

$$\mathbf{I}^n(x) = (\bar{\phi}_\mathbf{D}, l_\mathbf{D}(x)) + (\bar{\phi}_\mathbf{S}, l_\mathbf{S}(x)),$$

where $\bar{\phi}_\mathbf{D}$ is the diffuse chromaticity, and

$$l_\mathbf{D}(x) = \sqrt{\sum_{i=1}^{n} (m_d(x)\mathbf{D}_i)^2},$$

and $\bar{\phi}_\mathbf{S}$ is the specular chromaticity and

$$l_\mathbf{S}(x) = \sqrt{\sum_{i=1}^{n} (m_s(x)\mathbf{S}_i)^2}.$$

For a scene with several surface colors, the DRM equation must assume that the diffuse component may vary spatially, while the specular component is constant across the image domain:

$$\mathbf{I}^n(x) = m_d(x)\mathbf{D}^n(x) + m_s(x)\mathbf{S}^n, \tag{7.2}$$

that in Hyperspherical coordinates is expressed as:

$$\mathbf{I}(x) = (\bar{\phi}_{\mathbf{D}}(x), l_{\mathbf{D}}(x)) + (\bar{\phi}_{\mathbf{S}}, l_{\mathbf{S}}(x)),$$

where $\bar{\phi}_{\mathbf{D}}(x)$ is the pixel diffuse chromaticity, and

$$l_{\mathbf{D}}(x) = \sqrt{\sum_{i=1}^{n} (m_d(x)\mathbf{D}_i(x))^2},$$

and $\bar{\phi}_{\mathbf{S}}$ the specular chromaticity, and

$$l_{\mathbf{S}}(x) = \sqrt{\sum_{i=1}^{n} (m_s(x)\mathbf{S}_i)^2}.$$

The chromaticity of the specular component $\bar{\phi}_{\mathbf{S}}$ is space invariant, meaning that the ISC is constant all over the scene.

Chapter 8

Hyperspectral Gradients

In this chapter proposes two gradients for hyperspectral images; first one is a chromatic gradient whereas the second one is a hybrid gradient, combining the chromatic gradient and another based Euclidean distance for the improved edge detection in dark regions. These proposals are grounded on DRM through Hyperspherical coordinates providing robustness against illumination effects: highlights and shadows.

The structure of the chapter is as follows: Section 8.1 provides a short review of the state of the art. Section 8.2 introduces the chromatic gradient for hyperspectral images. Section 8.3 gives some experimental results of the chromatic gradient. Section 8.4 describes the hyperspectral hybrid gradient. Section 8.5 gives some results of the hybrid gradient. Section 8.6 gives the chapter conclusions.

8.1 State of the Art

Edge detection in hyperspectral images is an intrinsically difficult problem because there is no appropriate definition of the gradient operator in multivariate functions. The straightforward approach of combining the independent gradients computed on each band can be mislead by confusing and contradicting detection. Some works have used this approach for watershed segmentation [103]. The band gradients are combined into a vector valued approach [140] performing clustering of the pixel hyperspectral signature composed of the band gradient values instead of the original intensity values. The result is a unsupervised classification of pixels into edge and non-edge pixels.

Manifold Learning

A definition of the spectral edge is presented in [141] based on a data-driven manifold learning. Authors construct the manifold coordinate system of the hyperspectral imagery by using a local property preserved manifold learning method and then rewrite the image with the manifold coordinates of each pixel, it is by using the LTSA algorithm. After that they apply the canny edge detector induced by the Jacobian of the new manifold. Bakker [142] applied the laplacian edge detector on hyperspectral images by using three different distances (Euclidean, angular and intensity difference) inside the laplacian descriptor. Similar idea is applied by using cellular automate (CA)[143]. In this work, a CA implements morphological operators and other one implements Prewitt edge detector. Dimensionality reduction is performed alternatively by PCA, Fisher's linear discriminant analysis (LDA), and an unsupervised LDA approach that utilizes clustering.

Other works follow similar approaches, like the Spectral Similarity Measure for Edge Detection [144] performing first a dimensionality reduction by PCA , afterward applies an edge detector defined as follow. It uses a generalized Prewitt and Sobel mask which are implemented using the Euclidean distance, Taxicab, Maximum distance, Spectral angle or Spectral information divergence. These distances are defined for the spectral vector. Authors implement the derivative of the laplacian too.

Reflection model based

There are some works grounded on reflection models, for example [145] performs a self-correcting brightness gradients for urban areas using the BDRF model. The method can justify the changes of reflectance depending of the point of view and the illumination source position. After that, authors apply different threshold mask over the input image correcting the brightness gradient which is applied successfully in urban areas with different features (vegetated surfaces, highways and buildings). For multi-spectral images, Robles A. [146] proposes the use of DRM looking for photometric invariance. This approach is interesting because refer to a colorimetric concept. The goal of this work is to estimate the DRM parameter of the image, hence they are able to separate the diffuse and specular components. This work is applied

$$\begin{bmatrix} -1 & 0 & 1 \\ -1 & 0 & 1 \\ -1 & 0 & 1 \end{bmatrix} \begin{bmatrix} -1 & -1 & -1 \\ 0 & 0 & 0 \\ 1 & 1 & 1 \end{bmatrix}$$

Figure 8.1: Convolution kernels for the Prewitt edge detection operator.

for human face recognition. Neither of the aforementioned references may be taken as grounded chromaticity or colorimetric approaches, except the timid approximation of [146] referring to photometry and DRM in multispectral images.

8.2 Chromatic Gradient Operators

The simplest convolution kernels for edge detectors are the Prewitt operators, illustrated in Fig. 8.1. We build our spatial chromatic gradient operators following their pattern. To take into account spectral information, the straightforward approach is to apply the gradient operators to each spectral band as an independent intensity image and to combine the results afterwards $\nabla \mathbf{I} = \sum_{i=1}^{n} \nabla I_i / n$, where I_i denotes the i-th image spectral band.

Fig. 8.2 shows the results of this approach using Prewitt gradient operators on two hyperspectral images (The first one is a plastic blue ball in front of a green background, the second one is a plastic orange ball in front of the same green background. Both images captured under natural sun illumination). The first row shows one band of the images. Second row shows the gradient magnitude. The third row shows some edges detected applying a threshold to the gradient magnitude image. The intensity image component has a strong influence on this gradient computation, therefore some highlights and shadows are identified as image regions and their boundaries detected as image edges.

In order to define a chromatic gradient operator, we may assume a kind of non-linear convolution where the convolution mask has the same structure as the Prewitt operators in Fig.8.1, but the underlying chromatic distance is

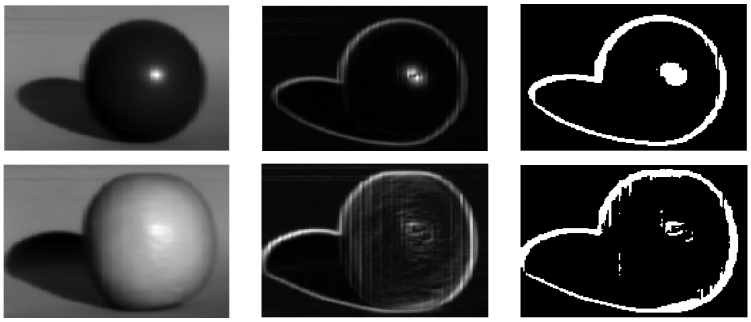

Figure 8.2: Results on two hyperspectral images of image gradient computed applying the Prewitt gradient operators to each band independently. Left, a single band of the original image. Middle, gradient magnitude. Right, edge detection thresholding the gradient magnitude.

based only on the chromaticity as follows: For two pixels p and q we compute the Manhattan distance on the chromatic representation of the pixels:

$$\angle(p,q) = \sum_{i=1}^{n-1} \left| \bar{\phi}_{p,i} - \bar{\phi}_{q,i} \right| . \tag{8.1}$$

Note that the $\angle(\mathbf{C}_p, \mathbf{C}_q)$ distance is always positive. Note also that the process is non linear, so we can not express it by linear convolution kernels. The row pseudo-convolution operator is defined as

$$CG_R\left(\mathbf{C}\left(i,j\right)\right) = \sum_{r=-1}^{1} \angle\left(\mathbf{C}\left(i-r, j+1\right), \mathbf{C}\left(i-r, j-1\right)\right),$$

and the column pseudo-convolution operator is defined as

$$CG_C\left(\mathbf{C}\left(i,j\right)\right) = \sum_{c=-1}^{1} \angle\left(\mathbf{C}\left(i+1, j-c\right), \mathbf{C}\left(i-1, j-c\right)\right),$$

so that the color distance between pixels substitutes the intensity subtraction of the Prewitt linear operator. The hyperspectral chromatic gradient magnitude image is computed as:

$$CG(x) = CG_R\left(x\right) + CG_C\left(x\right) \tag{8.2}$$

8.3 Experimental results

Experiments are performed on images taken by SOC 710 hyperspectral camera. Spectral resolution is 128 bands in the range 300mn to 1000nm. These images have been presented in the first row of Fig. 8.2. On these images we can analyze the illumination effects over the objects. On these images there are only two chromatically different surfaces, a uniform green background and a monochromatic object, in one case a dark blue ball with a sweet surface; in the other one is plastic model of an orange. In the second case, the object has a wrinkled surface.

We have applied the chromatic gradient of Eq. (8.2) on the images. The results are shown in Fig. 8.3. First row shows the original intensity images. The second row shows the chromatic gradient magnitude image. As we can appreciate, true surface edges are better detected than in Fig. 8.2, even on shadowy regions of the image. The highlights have lower response than in Fig. 8.2, so that no spurious edges are detected around them. The chromatic gradient has a high response on the shadows, but this response is uniformly distributed on the whole shadow and it is not bigger than the true borders. This effect is consequence of the noise distribution on the image. The chromatic distance is more sensitive on region with poor illumination or on regions poor reflectance like the blue ball. Comparing these results with the traditional gradients like the shown on Fig.8.2, the chromatic gradient is focused on the chromaticity and has a bigger response on chromatic edges. Finally, last row shows the edge detection after applying a threshold on the gradient magnitude image. The threshold is computed by the Otsu minimal variance approach. In these results, we have found the correct object edges avoiding the false detection of borders of highlights and shadows despite the high dimensional nature of these hyperspectral images.

8.4 A Hybrid Hyperspectral Gradient

Analogously to the chromatic gradient, we can define a distance for the original image in the Euclidean coordinate representation of the spectra of two pixels as:

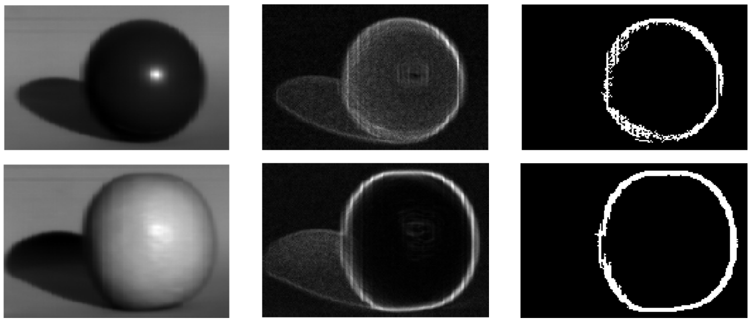

Figure 8.3: Pseudo Prewitt gradient on the chromatic image

$$\psi(p,q) = \sum_{i=1}^{n} \|I_{p,i} - I_{q,i}\| \tag{8.3}$$

where n is the vector dimensionality, the number of bands in the hyperspectral image.

The row pseudo-convolution is defined as:

$$IG_R\left(\mathbf{I}\left(i,j\right)\right) = \sum_{r=-1}^{1} \psi\left(\mathbf{I}\left(i-r,j+1\right), \mathbf{I}\left(i-r,j-1\right)\right),$$

and the column pseudo-convolution is defined as

$$IG_C\left(\mathbf{I}\left(i,j\right)\right) = \sum_{c=-1}^{1} \psi\left(\mathbf{I}\left(i+1,j-c\right), \mathbf{I}\left(i-1,j-c\right)\right),$$

so that the distance between pixel spectra substitutes the intensity subtraction of the Prewitt linear operator. The hyperspectral gradient image is computed as:

$$IG(x) = IG_R\left(x\right) + IG_C\left(x\right) \tag{8.4}$$

Fig. 8.4 shows examples of the intensity gradient performance. As we can see, it is very sensitive to intensity changes, but it can detect edges in regions with poor illumination better than the chromatic gradient.

8.4.1 Hybrid gradient

Our goal is to develop a hybrid gradient with takes profit of the best properties of each one of the previous gradients. Inspired on the HVS, on the

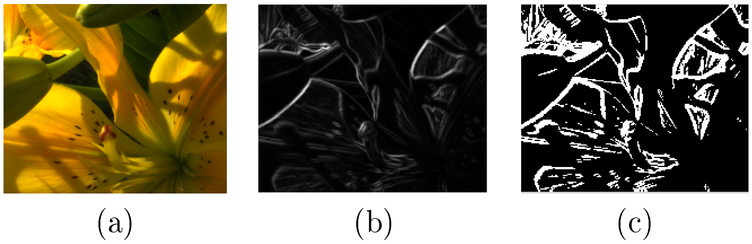
(a) (b) (c)

Figure 8.4: e-Gradient. (a) Original hyperspectral image, (b) intensity gradient magnitude, (c) a binarization of the intensity gradient magnitude.

retina, there are two main kinds of cells; cones and rods. The rods are luminance detectors and the cones are chromatic detectors. Both need different energy levels for their activation. Rods need less energy than cones, for this reason human vision becomes grayscale under poor illumination, and colors are better detected with a good illumination.

We propose the mixing function $\alpha(x)$ of the chromatic and intensity components of the hybrid gradient. For intensity values below a, the chromatic component of the distance is inactive. For intensity values in the interval $[a, b]$ we smoothly change the contribution of the chromatic component of the hybrid distance from zero to its maximum $c \leq 1$ according to a sinusoidal function. Finally, for intensity values above b its contribution is always c. The three parameters a, b, c are in the range $[0, 1]$. The function $\alpha(x)$ specifying the mixing of the chromatic and grayscale distances depending on the image intensity is defined as follows:

$$\boldsymbol{\alpha}(x) = \begin{cases} 0 & x \leq a \\ \frac{c}{2} + \frac{c}{2}\cos\left(\frac{(x-a)\cdot\pi}{b-a} + \pi\right) & a < x < b \\ c & x \geq b \end{cases} \tag{8.5}$$

By analogy with the human visual system, we propose the hybridization scheme illustrated in Fig. 8.5.

1. Given a hyperspectral image **I** we can obtain the chromaticity image **C** and the intensity image **J**.
2. Applying Eq.(8.4) on **I** we obtain the image gradient IG.
3. Applying the Eq.(8.2) on **C** we obtain the image gradient CG.

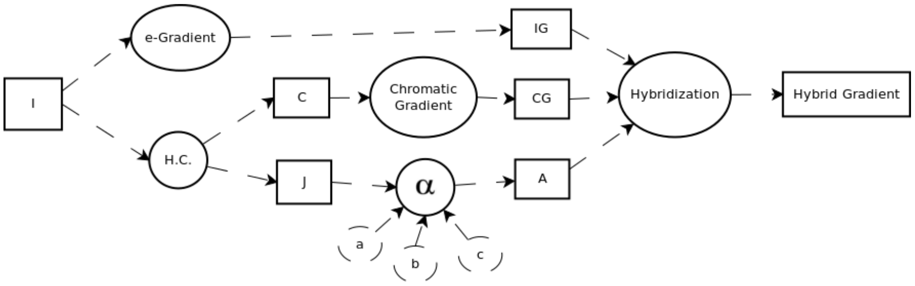

Figure 8.5: Scheme of the hybrid gradient

4. Applying the Eq.(8.5) on **J** we obtain the $\boldsymbol{A}$ matrix which help to compute the hybridization of the whole image as:

$$HG = \boldsymbol{A} * CG + (1 - \boldsymbol{A}) * IG \tag{8.6}$$

8.5 Experimental Results of the Hybrid Gradient

The response of the proposed hybrid gradient can be adapted to different images or different expectations of results by using the a, b, c parameters of the α function. For the experiment on this section, we have used the same parameters $a = 0$, $b = 0.1$ and $c = 1$. It means that we are going to perform mainly a chromatic gradient and for regions poorly illuminated we use the e-gradient, as we defend in this work. Nevertheless, changing the parameters of α we can obtain different gradients.

We present some experimental results over the images of Foster data set[147]. Fig.8.6 shows the experimental results. First column contains the original RGB images, second one contains the hybrid gradient output and third row show a binarization based on Otsu thresholding. We can appreciate on the first image, how the digital[1] flower is perfectly detected and differenced from the background, hence it looks homogeneity inside in despite of the shadows of each bell. Worth some words the third image which can differentiate the different chromatic regions with independence of it intensity. If we compare it with the output of the Fig.8.4, we can appreciate how the hybrid gradient avoids the shortcoming of the previous gradients and takes

---

[1] digital is the name of this flower

profit of the best properties of each ones, and by the hybridization we have a good result; invariance respect to the intensity changes, and edge detection on dark regions. Last image shows a clear example as the shadow effects are avoid by the hybrid gradient. The shadow on the frontage house has not effect on the gradient, whereas edges of dark regions like the houses behind are well detected.

8.6 Conclusions

The computation of gradients on hyperspectral images implies the combination of high dimensional information and is prone to spurious detections due to noise and illumination effects, such as highlights and shadows. In this chapter, the approach proposed in [96] for color images, is extended to high-dimensional images, allowing the robust detection of object boundaries despite strong illumination effects. We have tested the approach on indoors captured hyperspectral images. Object boundaries are effectively found and spurious edges are avoided in these images. Further work needs to be done on the extensive validation of the approach on hyperspectral images with known ground truth.

Second part of this chapter, presents a hybrid gradient for hyperspectral images. It is versatile thanks to the α function which can adapt the hybrid gradient performance to different expectations. In addition, the e-gradient can be used on n-dimensional images, and the Hyperspherical coordinates can be applied too on n-dimensional images, therefore, the proposed Hybrid gradient can be used on all images (independent of its amount of bands). Results on hyperspectral images show that the hybrid algorithm provides robust edge detection avoiding false edges introduced by highlights and shadows.

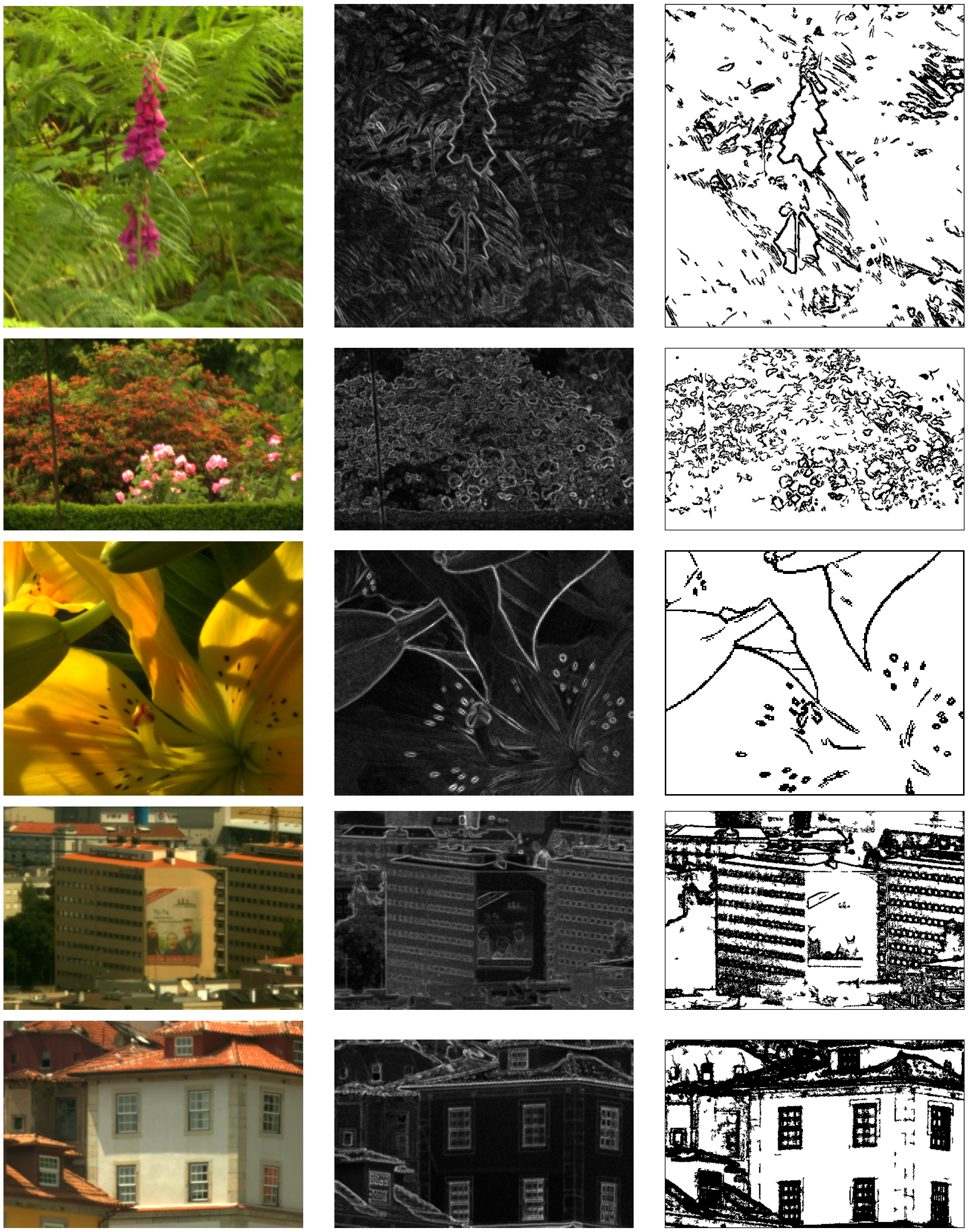

Figure 8.6: Hybrid gradient on hyperspectral images. First column shows the grayscale image, second column shows the chromatic gradient and third column shows a binarization of the gradient image based on Otsu threshold.

Chapter 9

Hyperspectral Image Segmentation

This chapter presents a segmentation method for hyperspectral images based on the well-known watershed transformation with some improvements in order to overcome oversegmentation issues. The approach uses the aforegoing chromatic and hybrid gradients for hyperspectral images, therefore it is grounded on the hyperspherical transform taking profit of the DRM for hyperspectral images. The chapter approach is algorithmic and experimental.

This chapter is outlined as follows: Section 9.1 does a brief review of some segmentation methods for hyperspectral images (state of the art). Section 9.2 explains in detail the segmentation method. Section9.2.3 shows the experimental results on images taken with a SOC 710 camera, and on images of the Foster dataset. Finally, Section9.3 gives the conclusions.

9.1 State of the Art

Most computational methods for hyperspectral image segmentation are classification methods which fall into three categories: supervised, semi-supervised and unsupervised methods. Supervised methods require prior knowledge in the form of a given ground truth to guide the building of the segmentation method. Unsupervised methods do not need prior knowledge to carry out a segmentation. Finally, semi-supervised methods are a mixture of both. Often classification methods are preceded by some dimensionality reduction in order to reduce noise effects and improve the speed-up.

Supervised methods

Jun Li et al. [148, 149] apply active learning to hyperspectral image segmentation in a Bayesian framework. Their algorithm is summarized in two steps:

1. Learning the class posterior probability distributions, based on a multinomial logistic regression (MLR) model, using the LORSAD algorithm.

2. Segmenting the hyperspectral image, based on the posterior probability distribution of the image of class labels built on the learned pixel-wise class distributions.

Active learning is used in order to maximize the classification performance with the minimum size training set. The relevant question is what samples should be chosen to be labeled from the pool of unlabeled samples. Authors iteratively select the samples which is expected to provide the maximum information with respect to the actual random vector of MLR regressors. Other supervised Bayesian approaches [150, 151] use MLR too, but combined with Random Markov Fields or multilevel logistic spatial prior, exploiting spatial and spectral information.

Semi-supervised methods

A semi-supervised segmentation method exploiting spatial contextual information is proposed in [88, 152]. The method has two steps:

1. Apply a semi-supervised learning algorithm to infer the class distributions

2. Afterwards perform the image segmentation, by inferring the labels from a posterior distribution.

Semi-supervised learning methods combine labeled and unlabeled pixels, unlabeled pixels are dealt with by unsupervised methods, such as clustering, and fused with labeled pixels in a supervised classification step. The class distributions are modeled with a MLR.

Unsupervised methods

Mercier [153] presents a Hidden Markov Chain whose parameter estimation is performed by the Iterative Conditional Estimation (ICE) method. At the heart of this method there is a C-means that initializes the parameters of the HMC, afterwards ICE completes the parameter estimation. This work is tested with diverse dimensionality reduction algorithms (PCA, MNF, PP, NAP, CCA y CDA). Other works perform clustering processes, such as [154] which relies only on the spectral information; the image is statistically characterized by means of a Gaussian Mixture Model (GMM). In short, this method : 1) it finds a discriminant function. 2) it performs a partial segmentation procedure, evaluating the parameters of GMM by using a RELAXation technique. 3) The segmentation process is concluded by combining the partial results obtained from the analysis of each significant component. Bilgin [155] uses a one-class Support Vector Machine (OC-SVM) where the cluster validity measure is based on the power of spectral discrimination.

There are also methods exploiting the spatial information. Ertürk[156] presents a method based on the phase-correlation between subsamples. This method is based on FFT and it's robust against noisy data. It defines the phase-correlation as a distance to guide a region growing segmentation strategy. The Butterfly approach introduced by Gorretta [157] works with the spectral and spatial information in two separated steps. The image segmentation is carried out by an iterative process interleaving spatial and spectral segmentation steps until reaching convergence. Active contours are applied by Zhang [158] for hyperspectral image segmentation using the Chan-Vese's energy function adapted to hyperspectral images. Finally, Tarabalka [103] work is based on the watershed transformation, performing the watershed on each band, seeking afterwards to find the image edges piling up all watershed edges in a image matrix.

9.2 Segmentation Method

The hyperspectral image segmentation method proposed in this chapter is based on the watershed transformation following a straightforward approach, because we do not aim to define a chromaticity based region growing/merging process, and we may benefit by the hyperspectral gradients presented in the previous chapter for the definition of the watershed transform.

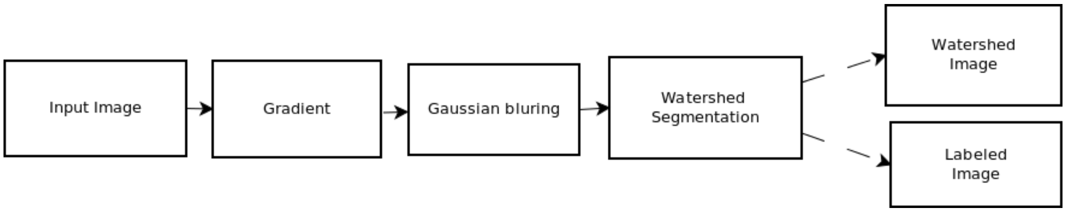

Figure 9.1: Hyperspectral segmentation diagram flow

9.2.1 Segmentation Algorithm

As defined previously, the watershed transformation interprets a gradient image as a topographic relief. The transformation begins with a flooding process carried out from each gradient local minima. Where neighboring regions meet, a watershed edge appears. Each local minimum of the image gradient corresponds only to one image region in the segmentation. This is called the natural segmentation.

A shortcoming of the standard watershed transform is over-segmentation. The natural segmentation is composed of many small regions. To avoid oversegmentation we combine two strategies. On the one hand, we use a threshold to merge neighboring low gradient regions. On the other hand, applying a Gaussian smoothing filter we reduce over-segmentation in regions of high intensity gradient. A feature of the application of Gaussian blurring to the gradient image is that its main peaks are preserved, whereas spurious local minima are removed. Henceforth, we refer to this watershed variant as t-Watershed.

Fig.9.1 shows the diagram flow of the segmentation algorithm. First, the method calculates a hyperspectral gradient. Second, it applies a Gaussian smoothing filter. The blurred gradient is the input of the proposed t-Watershed transform. At the end, the method outputs an image with the watershed edges and another one with the labeled regions.

9.2.2 t-Watershed Algorithm

The code of the algorithm is specified in detail in Algorithm9.1. The algorithm input is a *gradient* image (IG), a initial *threshold* (thr) and the *amount* *of iterations* (steps); its output is the watershed image (WS), and an image containing the labeled regions (IL). A description its workings is as follows:

- First, it initializes the output images, and defines the intensity jump for thresholding the image gradient.
- Applies a threshold to find regions of minimal gradient. Usingy the Matlab primitive function 'bwlabel' it initializes the image containing the segmentation region labels.
- The algorithm begins the flooding process which is finished after performing 'steps' iterations
    - It calculates the new threshold (thi), and, applying it on the image gradient, it finds the new pixels to be labeled.
    - For each unlabeled pixel, it finds out in its respective neighborhood if some of its neighboring pixels has been labeled.
    - Depending of the labels found in the neighborhood, the algorithm does different things on the current pixel:
        - If there are not labeled pixels, it creates a new label assigning it to the current pixel
        - If there is only one label, it assigns it to the current pixel
        - If there are several labels
            - If the gradient intensity is lower than the parameter 'thr', it merges all regions in a label, assigning it to the current pixel
            - In any other case, it marks it as watershed pixel

9.2.3 Experimental Results

Experimental results are carried out, first on the hyperspectral images taken with the SOC 710 camera, second on some images of the Foster database. The main goal of our segmentation algorithms is to provide robustness against illumination effects, such as shines, shadows and sudden illumination changes. The aim is to perform the image segmentation on the basis of the true surface

Algorithm 9.1 t-Watershed code

```
function [WS, IL]= t-Watershed(IG,thr, steps)


[a,b] = size(IG);
WS = zeros(a,b); // Watershed image
IL = zeros(a,b); //Image labels
mx = max (IG); mn = min (IG); df = mx - mn; // intensity range
jump = df / steps; // jump size


// initilize first regions
s = find(IG < mn + jump); IL(s) = 1;
[IL, nLabels] = bwlabel(IL);


for i = 1:  steps // repeat until finish
    BW2 = zeros(a,b); // temporal matrix
    thi = mn + (jump * i); // current intensity threshold
    s = find(IG < thi & IG > 0); BW2 (s) = 1;// select pixels with intensity < thi
    //find the new pixels and the already labeled set 0
    s2 = find (IL > 0); BW2(s2) = 0;
    // new pixels labeling
    [f,c] = find(BW2 == 1);


    for j = 1:  size(f,2) // for each new pixel to label
        fl = f(j); //row and column
        cl = c(j);
        // look into the 8-neighborhood
        lvec = 0; //neighbor list
        nvec = 0; //amount of neighbors
        VnL = zeros(3,3);// copy of window neighborhood
        for ff = -1:1
            for cc = -1:1
                vec = [ff + fl , cc + cl]; // range control
                if vec(1) > 0 & vec(1) < a & vec(2) > 0 & vec(2) < b &(ff != 0 | cc != 0)
                    if IL(vec(1), vec(2))> 0 // this neighbor is already labeled
                        nvec = nvec +1;
                        lvec(nvec) = IL(vec(1), vec(2)); // save the label
                        VnL(ff+2,cc+2)= IL(vec(1), vec(2));
                    end
                end
            end
        end


        // different cases depending of the labels into the neighborhood
        if nvec == 0 // there are not label in the neighborhood
            nLabels = nLabels +1; // to increment label counter
            IL(fl,cl) = nLabels; // assign the new label to the current pixel
        else //there are some label
            llbvec =0; // label list for the neighborhood
            nlbvec =0; // counter
            lb = 0;// current label
            // look for the labels in the neighborhood
            for it = 1:nvec
                lb = lvec(it);
                s = find(llbvec == lb); // look if this label is already saved in the list
                if size(s,1) == 0 // it is not into the list
                    nlbvec = nlbvec +1;
                    llbvec(nlbvec) = lb;
                end
            end
            if nlbvec == 1 then // there is only label into the neighborhood
                IL(fl,cl) = lb; // assign it to the current pixel
            else // there are many labels
                if IG(fl,cl) < thr then // region merging
                    lb = llbvec(1);
                    for k = 2:nlbvec
                        s = find(IL == llbvec(k));
                        IL(s)= lb;
                    end
                else // mark it as Watershed
                    WS(fl,cl)=1;
                end
            end
        end
    end
end
endfunction
```

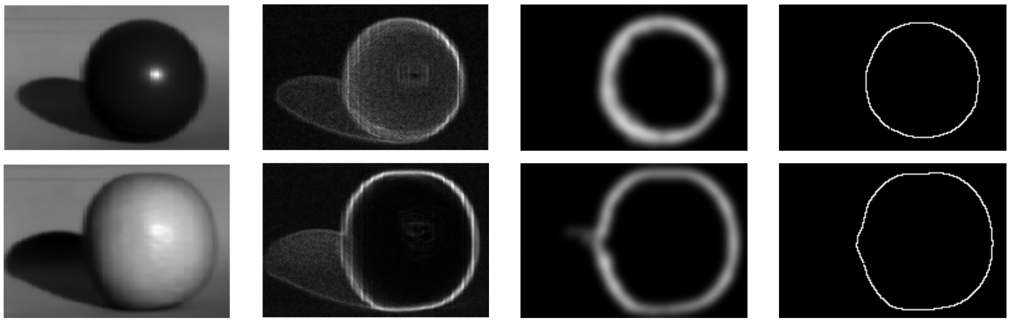

Figure 9.2: t-Watershed segmentation of images taken with SOC 710 camera

features. For this reason we work on the hyperspherical coordinate representation of the pixel spectra, which are included in the chromatic and hybrid hyperspectral gradients used for the segmentation process. For all experiments reported below we set $thr = 0.2$ and $steps = 100$.

9.2.3.1 SOC 710 images

First experiments are done on two hyperspectral images who we have captured with the SOC 710 camera: the blue ball and the synthetic orange. Fig. 9.2 shows the results. First row of images in the figure shows the process of the blue ball image, the second row shows the process of the synthetic orange image. From left to right, images in the first column are the intensity images. The second column show the corresponding chromatic gradient. The third column shows the blurred output of the edge detected using the approach introduced in the previous chapter. The last (rightmost) column shows the output of the proposed t-Watershed algorithm. We can appreciate that the segmentation gives the correct segmentation avoiding segmentation of the spurious edges induced by the shines and the shadows.

9.2.3.2 Foster Database Images

This segmentation is applied over some images of the Foster database. In these images, there are few shines but there are many shadows and strong intensity changes. In this case we have used the hybrid hyperspectral gradient proposed in the previous chapter, where the parameters of the alpha function are set as follows: $a = 0$, $b = 0.1$ and $c = 1$.

Fig.9.3 shows the experimental results. From left to right, the first column shows a RGB rendering of the original images, the second shows the blurred hyperspectral image gradient, and the last one (rightmost) shows their output segmentation. We can appreciate in the first image that flowers and dark regions are well separated from the green background. Respect to the second image, we can see how the shadow of the house facade is avoided whereas the rest of the image is well segmented. The third image is a good test for out method because it has a lot of intensity changes whereas it has few different region colors. As we can note in its corresponding the output segmentation, regions with different chromatic properties are well differentiated. For instance, the boundaries between the flower and the green leaves are detected, while the intensity changes due to illumination effects inside the yellow region are ignored. Last image row shows the segmentation of some buildings with some regions well illuminated and other ones into the shadows.

These experiments show the nominal response of the proposed method setting parameters to their more standard values despite variation in the images. Because the most important parameter of the segmentation method is in the mind of the user. For different segmentation goals we must to change some parameters into the code and adapt it accordingly with the desired segmentation.

9.3 Conclusion

In this chapter we have proposed a new segmentation method for hyperspectral images with the following properties:

- It uses an adjustment of the watershed transform (t-Watershed).
- It is grounded on DRM through the use of the hyperspherical transformation discussed in previous chapters.
- It avoids oversegmentation of low and high gradient regions. In the first case by using a threshold, and in the second case by applying a Gaussian blurring.

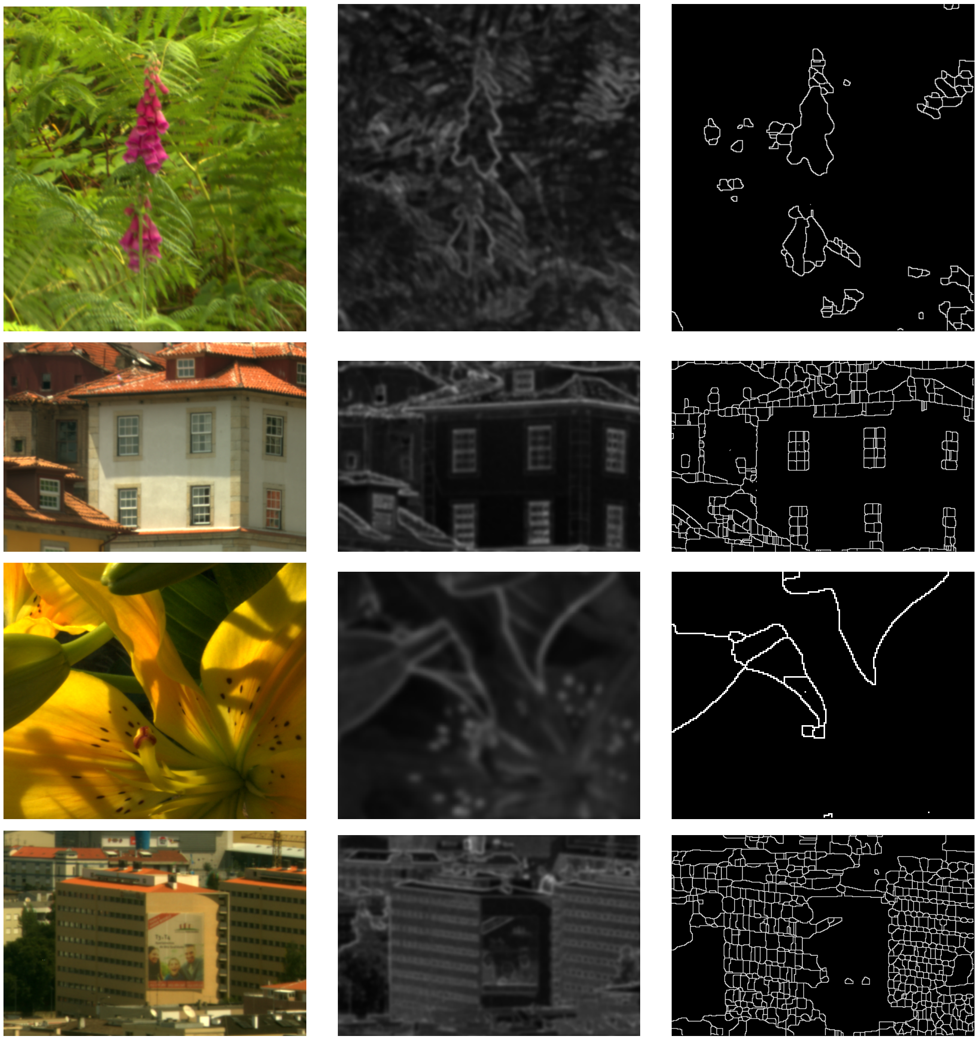

Figure 9.3: t-Watershed segmentation of some images from the Foster's database.

- Experimental results (preliminar) show good segmentation, avoiding shadows and shines, because it is guided by the diffuse component of DRM, thus dealing with the true surface.
- It shows a good behavior too in natural scenes.
- By tuning the *alpha function* parameters of the hybrid gradient and the parameters of the t-Watershed the user could easily tune the segmentation to his needs. Further work must be addressed to provide some automatized tool for this parameter tuning, such as some kind of interactive evolutionary algorithm.

Appendix A

Glosary

Albedo of an object is the extent to which it diffusely reflects light from the sun. It is therefore a more specific form of the term reflectivity. Albedo is defined as the ratio of diffusely reflected to incident electromagnetic radiation. It is a unit less measure indicative of a surface's or body's diffuse reflectivity. The word is derived from Latin albedo "whiteness", in turn from albus "white". The range of possible values is from 0 (dark) to 1 (bright).

Azimuth is the horizontal angular distance from a reference direction, usually the northern point of the horizon, to the point where a vertical circle through a celestial body intersects the horizon, usually measured clockwise. Sometimes the southern point is used as the reference direction, and the measurement is made clockwise through 360 grades.

Chromaticity is an objective specification of the quality of a color irrespective of its luminance, that is, as determined by its colorfulness (or saturation, chroma, intensity, or excitation purity) and hue.

Colorfulness, chroma, and saturation are related concepts referring to the intensity of a specific color. More technically, colorfulness is the perceived difference between the color of some stimulus and gray, chroma is the colorfulness of a stimulus relative to the brightness of a stimulus that appears white under similar viewing conditions, and saturation is the colorfulness of a stimulus relative to its own brightness. Though this general concept is intuitive, terms such as chroma, saturation, purity, and intensity are often used without great precision, and even when well-defined depend greatly on the specific color model in use.

Diffuse reflection is the reflection of light from an uneven or granular surface such that an incident ray is seemingly reflected at a number of angles. It is the complement to specular reflection. If a surface is completely non specular, the reflected light will be evenly spread over the hemisphere surrounding the surface (2π steradians). The most familiar example of the distinction between specular and diffuse reflection would be matte and glossy paints as used in home painting. Matte paints have a higher proportion of diffuse reflection, while gloss paints have a greater part of specular reflection.

Fresnel equations, deduced by Augustin-Jean Fresnel, describe the behavior of light when moving between media of differing refractive indices. The reflection of light that the equations predict is known as Fresnel reflection.

Hue is one of the three main attributes of perceived color, in addition to lightness and chroma (or colorfulness). Hue is also one of the three dimensions in some color spaces along with saturation, and brightness (also known as lightness or value). Hue is that aspect of a color described with names such as "red", "yellow", etc.

Insolation (Incident solar radiation) is a measure of solar radiation energy received on a given surface area in a given time. It is commonly expressed as average irradiance in watts per square meter (W/m^2) or kilowatt-hours per square meter per day ($\frac{kW*h}{m^2*day}$) , or in the case of photovoltaic it is commonly measured as $kWh/kWp*y$ (kilowatt hours per year per kilowatt peak rating). Sometimes, as in the text below, a long-term average intensity of incoming solar radiation will be given in units such as watts per square meter (W/m2 or W*m-2) and called insolation, with the duration (such as daily, annual, or historical) stated or only implied.

Irradiance, radiant emittance, and radiant exitance are radiometry terms for the power of electromagnetic radiation at a surface, per unit area. "Irradiance" is used when the electromagnetic radiation is incident on the surface. "Radiant exitance" or "radiant emittance" is used when the radiation is emerging from the surface. The SI units for all of these quantities are watts per square meter ($W * m^{-2}$).

Lambert's cosine law in optics says that the radiant intensity observed from a "Lambertian" surface is directly proportional to the cosine of the angle θ between the observer's line of sight and the surface normal. The law is also known as the cosine emission law or Lambert's emission law. It is named after Johann Heinrich Lambert, from his Photometria, published in 1760.

Lambertian reflectance, light falling on it is scattered such that the apparent brightness of the surface to an observer is the same regardless of the observer's angle of view. More technically, the surface luminance is isotropic. For example, unfinished wood exhibits roughly Lambertian reflectance, but wood finished with a glossy coat of polyurethane does not (depending on the viewing angle, specular highlights may appear at different locations on the surface). Not all rough surfaces are perfect Lambertian reflectors, but this is often a good approximation when the characteristics of the surface are unknown. Lambertian reflectance is named after Johann Heinrich Lambert.

Luminance is a photometric measure of the density of luminous intensity in a given direction. It describes the amount of light that passes through or is emitted from a particular area, and falls within a given solid angle. The SI unit for luminance is candela per square met re (cd/m2). The CGS unit of luminance is the stilb, which is equal to one candela per square centimeter or 10 kcd/m2.

Radiance and spectral radiance are radiometric measures that describe the amount of light that passes through or is emitted from a particular area, and falls within a given solid angle in a specified direction. They are used to characterize both emission from diffuse sources and reflection from diffuse surfaces. The SI unit of radiance is watts per steradian per square meter ($W * sr^{-1} * m^{-2}$).

Reflectivity is the fraction of incident radiation reflected by a surface. In full generality it must be treated as a directional property that is a function of the reflected direction, the incident direction, and the incident wavelength. However it is also commonly averaged over the reflected hemisphere to give the hemispherical spectral reflectivity: $\rho(\lambda) = \frac{G_{refll}(\lambda)}{G_{incid}}$ where Grefl(λ) and Gincid(λ) are the reflected and incident spectral (per wavelength) intensity, respectively.

Reflection is the change in direction of a wave front at an interface between two different media so that the wave front returns into the medium from which it originated. Common examples include the reflection of light, sound and water waves.

Snell's law (also known as Descartes' law or the law of diffraction), is a formula used to describe the relationship between the angles of incidence and refraction, when referring to light or other waves, passing through a boundary between two different isotropic media, such as water and glass. The law says that the ratio of the sines of the angles of incidence and of refraction is a constant that depends on the media.

Specular reflection is the perfect, mirror-like reflection of light (or sometimes other kinds of wave) from a surface, in which light from a single incoming direction (a ray) is reflected into a single outgoing direction. Such behavior is described by the law of reflection, which states that the direction of incoming light (the incident ray), and the direction of outgoing light reflected (the reflected ray) make the same angle with respect to the surface normal, thus the angle of incidence equals the angle of reflection; this is commonly stated as $\theta i = \theta r$.

Zenith is the direction pointing directly above a particular location (perpendicular, orthogonal). Since the concept of being above is itself somewhat vague, scientists define the zenith in more rigorous terms. Specifically, in astronomy, geophysics and related sciences (e.g., meteorology), the zenith at a given point is the local vertical direction pointing away from direction of the force of gravity at that location.

Bibliography

[1] K. Hara, K. Nishino, and K. Ikeuchi, "Light source position and reflectance estimation from a single view without the distant illumination assumption.," *IEEE Trans Pattern Anal Mach Intell*, vol. 27, pp. 493–505, Apr 2005.

[2] I. Sato and K. Ikeuchi, "Illumination from shadows," *Pattern Analysis and Machine Intelligence, IEEE Transactions on*, vol. 25, pp. 290–300, 2003.

[3] R. Moreno, M. Graña, and A. d'Anjou, "Illumination source chromaticity estimation based on spherical coordinates in rgb," *Electronics Letters*, vol. 47, no. 1, pp. 28–30, 2011.

[4] T. Tan, K. Nishino, and K. Ikeuchi, "Illumination chromaticity estimation using inverse-intensity chromaticity space," in *Computer Vision and Pattern Recognition, 2003. Proceedings. 2003 IEEE Computer Society Conference on*, vol. 1, pp. I–673–I–680vol.1, 18-20 June 2003.

[5] Y.-J. C. Kuk-Jin Yoon and I. S. Kweon, "Illuminant chromaticity estimation using dichromatic slope and dichromatic line space," in *Korea-Japan Joint Workshop on Frontiers of Computer Vision*, pp. 219–224, FCV, 2005.

[6] c. H. Marc Ebner, "On determining the color of the illuminant using the dichromatic reflection model," in *Pattern Recognition* (S. B. . Heidelberg, ed.), vol. 3663/2005, pp. 1–8, 2005.

[7] D. A. Forsyth and J. Ponce, *Computer Vision: A Modern Approach.* Prentice Hall, US ed ed., Aug. 2002.

[8] J. Lambert, *Photometria sive de mensure de gratibus luminis, colorum umbrae.* Eberhard Klett, 1760.

[9] T. Gevers and A. W. M. Smeulders, "Color-based object recognition," *Pattern Recognition*, vol. 32, pp. 453–464, Mar. 1999.

[10] P. Skorupski and L. Chittka, "Is colour cognitive?," *Optics & Laser Technology*, vol. In Press, Corrected Proof, 2010.

[11] D. Pascale, "A review of rgb color spaces," 2003. http://www.babelcolor.com/download/Af.

[12] J. C. Maxwel, "Experiments on colour, as perceived by the eye, with remarks on colour-blindness," *TRANSACTIONS OF THE ROYAL SOCIETY OF EDlNBURGH*, vol. 21, pp. 255–299, 1885.

[13] J. L. Barbur and K. Spang, "Colour constancy and conscious perception of changes of illuminant," *Neuropsychologia*, vol. 46, no. 3, pp. 853–863, 2008.

[14] K. Barnard, *Practical colour constancy.* PhD thesis, Burnaby, BC, Canada, Canada, 1999. AAINQ51839.

[15] D. H. Foster, S. M. C. Nascimento, B. J. Craven, K. J. Linnell, F. W. Cornelissen, and E. Brenner, "Four issues concerning colour constancy and relational colour constancy," *Vision Research*, vol. 37, pp. 1341–1345, Apr. 1997.

[16] H. Spitzer and S. Semo, "Color constancy: a biological model and its application for still and video images," *Pattern Recognition*, vol. 35, pp. 1645–1659, Aug. 2002.

[17] J. Geusebroek, R. van den Boomgaard, A. W. M. Smeulders, and T. Gevers, "Color constancy from physical principles," *Pattern Recognition Letters*, vol. 24, pp. 1653–1662, July 2003.

[18] K.-J. Yoon, Y. J. Chofi, and I.-S. Kweon, "Dichromatic-based color constancy using dichromatic slope and dichromatic line space," in *Image Processing, 2005. ICIP 2005. IEEE International Conference on*, vol. 3, pp. III–960–3, 11-14 Sept. 2005.

[19] G. D. Finlayson and G. Schaefer, "Solving for colour constancy using a constrained dichromatic reflection model," *INTERNATIONAL JOURNAL OF COMPUTER VISION*, vol. 42, pp. 127—144, 2002.

[20] S. Mallick, T. Zickler, D. Kriegman, and P. Belhumeur, "Beyond lambert: reconstructing specular surfaces using color," in *Computer Vision and Pattern Recognition, 2005. CVPR 2005. IEEE Computer Society Conference on*, vol. 2, pp. 619–626 vol. 2, 2005.

[21] T. Zickler, S. Mallick, D. Kriegman, and P. Belhumeur, "Color subspaces as photometric invariants," in *Computer Vision and Pattern Recognition, 2006 IEEE Computer Society Conference on*, vol. 2, pp. 2000–2010, 2006.

[22] E. LAND, "Retinex theory of color vision," *JOURNAL OF THE OPTICAL SOCIETY OF AMERICA*, vol. 57, pp. 1428–&, 1967.

[23] R. Zia-ur, W. G. A, and J. D. J, "A comparison of the multiscale retinex with other image enhancement techniques," 1997.

[24] D. H. Brainard and B. A. Wandell, "Analysis of the retinex theory of color vision," *Journal of the Optical Society of America A*, vol. 3, pp. 1651–1661, Oct. 1986.

[25] S. Hong and S. Grossberg, "A neuromorphic model for achromatic and chromatic surface representation of natural images," *Neural Networks*, vol. 17, pp. 787–808, 2004.

[26] F. E. Nicodemus, "Directional reflectance and emissivity of an opaque surface," *Applied Optics*, vol. 4, pp. 767–773, July 1965.

[27] K. E. Torrance and E. M. Sparrow, "Theory for off-specular reflection from roughened surfaces," in *Radiometry*, pp. 32–41, Jones and Bartlett Publishers, Inc., 1967.

[28] H. Ragheb and E. Hancock, "A light scattering model for layered dielectrics with rough surface boundaries," *International Journal of Computer Vision*, vol. 79, pp. 179–207, 2008.

[29] K. Zhou, P. Du, L. Wang, Y. Matsushita, J. Shi, B. Guo, and H. Shum, "Decorating surfaces with bidirectional texture functions," *Visualization and Computer Graphics, IEEE Transactions on*, vol. 11, pp. 519–528, 2005.

[30] G. Hu, S. Ong, Y. Chen, and A. Nee, "Reflectance modeling for a textured object under uncontrolled illumination from high dynamic range maps," *Computers & Graphics*, vol. 31, pp. 262–270, Apr. 2007.

[31] H. W. Jensen, S. R. Marschner, M. Levoy, and P. Hanrahan, "A practical model for subsurface light transport," in *Proceedings of the 28th annual conference on Computer graphics and interactive techniques*, pp. 511–518, ACM, 2001.

[32] C. Donner and H. W. Jensen, "A Spectral BSSRDF for Shading Human Skin," in *Rendering Techniques 2006: 17th Eurographics Workshop on Rendering*, pp. 409–418, June 2006.

[33] R. L. Cook and K. E. Torrance, "A reflectance model for computer graphics," *ACM Transactions on Graphics (TOG)*, vol. 1, p. 7–24, Jan. 1982. ACM ID: 357293.

[34] H. W. Gary, *A BRDF Database Employing the Beard-Maxwell Reflection Model.*

[35] B. HAPKE, "Bidirectional reflectance spectroscopy .1. theory," *JOURNAL OF GEOPHYSICAL RESEARCH*, vol. 86, pp. 3039–3054, 1981.

[36] F. Weiwei and W. qingnong, "A scatterometer for measuring the polarized bidirectional reflectance distribution function of painted surfaces in the infrared," *Infrared Physics & Technology*, vol. In Press, Corrected Proof, 2008.

[37] S. A. Shafer, "Using color to separate reflection components," *color research and aplications*, vol. 10, pp. 43–51, april 1984.

[38] B. Maxwell, R. Friedhoff, and C. Smith, "A bi-illuminant dichromatic reflection model for understanding images," in *Computer Vision and Pattern Recognition, 2008. CVPR 2008. IEEE Conference on*, pp. 1 –8, june 2008.

[39] V. Osma-Ruiz, J. I. Godino-Llorente, N. Sáenz-Lechón, and P. Gómez-Vilda, "An improved watershed algorithm based on efficient computation of shortest paths," *Pattern Recogn.*, vol. 40, pp. 1078–1090, March 2007.

[40] A. Bieniek and A. Moga, "An efficient watershed algorithm based on connected components," *Pattern Recognition*, vol. 33, no. 6, pp. 907 – 916, 2000.

[41] M. Elwaseif and L. Slater, "Quantifying tomb geometries in resistivity images using watershed algorithms," *Journal of Archaeological Science*, vol. 37, no. 7, pp. 1424 – 1436, 2010.

[42] P. De Smet, "Optimized high speed pixel sorting and its application in watershed based image segmentation," *Pattern Recogn.*, vol. 43, pp. 2359–2366, July 2010.

[43] S. Beucher and C. Lantuejoul, "Use of Watersheds in Contour Detection," in *International Workshop on Image Processing: Real-time Edge and Motion Detection/Estimation, Rennes, France.*, Sept. 1979.

[44] F. Hachouf and N. Mezhoud, "A clustering approach for color image segmentation," in *Advanced Concepts for Intelligent Vision Systems* (J. Blanc-Talon, W. Philips, D. Popescu, and P. Scheunders, eds.), vol. 3708 of *Lecture Notes in Computer Science*, pp. 515–522, Springer Berlin / Heidelberg, 2005.

[45] G. Li, C. An, J. Pang, M. Tan, and X. Tu, "Color image adaptive clustering segmentation," in *Image and Graphics, 2004. Proceedings. Third International Conference on*, pp. 104–107, 2004.

[46] H. Cheng, X. Jiang, Y. Sun, and J. Wang, "Color image segmentation: advances and prospects," *Pattern Recognition*, vol. 34, pp. 2259–2281, Dec. 2001.

[47] J. Fan, M. Han, and J. Wang, "Single point iterative weighted fuzzy c-means clustering algorithm for remote sensing image segmentation," *Pattern Recognition*, vol. 42, pp. 2527–2540, Nov. 2009.

[48] K. Fu and J. Mui, "A survey on image segmentation," *Pattern Recognition*, vol. 13, no. 1, pp. 3–16, 1981.

[49] N. R. Pal and S. K. Pal, “A review on image segmentation techniques,” *Pattern Recognition*, vol. 26, pp. 1277–1294, Sept. 1993.

[50] D. Kim, K. H. Lee, and D. Lee, “A novel initialization scheme for the fuzzy c-means algorithm for color clustering,” *Pattern Recognition Letters*, vol. 25, pp. 227–237, 2004.

[51] M. Oussalah and S. Nefti, “On the use of divergence distance in fuzzy clustering,” *Fuzzy Optimization and Decision Making*, vol. 7, pp. 147–167, June 2008.

[52] Y. Xia, D. D. Feng, T. Wang, R. Zhao, and Y. Zhang, “Image segmentation by clustering of spatial patterns,” *Pattern Recognition Letters*, vol. 28, pp. 1548–1555, Sept. 2007.

[53] M. Grana, R. Moreno, and F. X. Albizuri, “Convex coordinates based on lattice independent sets as pattern features,” in *Proc. IEEE Int Fuzzy Systems Conf*, pp. 225–230, 2006.

[54] G. X. Ritter, G. Urcid, and M. S. Schmalz, “Autonomous single-pass endmember approximation using lattice auto-associative memories,” *Neurocomput.*, vol. 72, pp. 2101–2110, June 2009.

[55] H. Struve and R. Struve, “Lattice theory and metric geometry,” *Algebra Universalis*, vol. 58, pp. 461–477, 2008.

[56] A. H. And, *Mathematical Morphology in the L*a*b* Colour Space.* Technical Report N-36/01/MM, CMM„ 2001.

[57] A. Hanbury and J. Serra, *Mathematical Morphology in the HLS Colour Space.* British Machine Vision Conference, Manchaster, 2001.

[58] A. Hanbury and J. Serra, “Colour image analysis in 3d-polar coordinates,” in *In Proceedings of the DAGM'03 conference*, pp. 124–131, Springer-Verlag, 2003.

[59] J. Serra and Angulo, “Mathematical morphology in color spaces applied to the analysis of cartographic images,” *International Workshop on Semantic Processing of Spatial Data GEOPRO 2003*, vol. (ISBN 970-, pp. 59–66.

[60] D. Wang, "A multiscale gradient algorithm for image segmentation using watershelds," *Pattern Recognition*, vol. 30, no. 12, pp. 2043 – 2052, 1997.

[61] I. Dagher and K. E. Tom, "Waterballoons: A hybrid watershed balloon snake segmentation," *Image and Vision Computing*, vol. 26, no. 7, pp. 905 – 912, 2008.

[62] H. Zhang, J. E. Fritts, and S. A. Goldman, "Image segmentation evaluation: A survey of unsupervised methods," *Computer Vision and Image Understanding*, vol. 110, no. 2, pp. 260 – 280, 2008.

[63] J. Kittler, "On the accuracy of the sobel edge detector," *Image and Vision Computing*, vol. 1, no. 1, pp. 37 – 42, 1983.

[64] I. Abdou and W. Pratt, "Quantitative design and evaluation of enhancement/thresholding edge detectors," *Proceedings of the IEEE*, vol. 67, pp. 753 – 763, may 1979.

[65] J. Canny, "A computational approach to edge detection," *Pattern Analysis and Machine Intelligence, IEEE Transactions on*, vol. PAMI-8, pp. 679 –698, nov. 1986.

[66] L. G. Roberts, "MACHINE PERCEPTION OF THREE-DIMENSIONAL SOLIDS,," tech. rep., May 1963.

[67] R. A. Kirsch, "Computer determination of the constituent structure of biological images," *Computers and Biomedical Research*, vol. 4, no. 3, pp. 315 – 328, 1971.

[68] G. S. Robinson, "Edge detection by compass gradient masks," *Computer Graphics and Image Processing*, vol. 6, no. 5, pp. 492 – 501, 1977.

[69] B. Jahne, *Practical Handbook on Image Processing for Scientific and Technical Applications, Second Edition.* CRC Press, 2 ed., Mar. 2004.

[70] F. Segonne, "Active contours under topology Control—Genus preserving level sets," *International Journal of Computer Vision*, vol. 79, pp. 107–117, 2008.

[71] W. Mcilhagga, "The canny edge detector revisited," *Int. J. Comput. Vision*, vol. 91, pp. 251–261, February 2011.

[72] R. Moreno, M. Graña, and A. d'Anjou, "Evolutive parametric approach for specular correction in the dichromatic reflection model," in *Hybrid Artificial Intelligence Systems*, vol. 5271 of *Lecture Notes in Computer Science*, pp. 665–672, Springer Berlin / Heidelberg, 2008.

[73] M. G. Ramón Moreno, A. d'Anjou, and C. Hernandez, "Bayesian reflectance component separation," in *Knowledge-Based and Intelligent Information and Engineering Systems*, vol. 5712 of *Lecture Notes in Computer Science*, pp. 846–852, Springer Berlin / Heidelberg, 2009.

[74] R. Moreno, M. Graña, and A. d'Anjou, "A geometrical method of diffuse and specular image components separation," in *Advances in Computational Intelligence* (J. Cabestany, I. Rojas, and G. Joya, eds.), vol. 6692 of *Lecture Notes in Computer Science*, pp. 83–89, Springer Berlin / Heidelberg, 2011.

[75] J. Lellmann, J. Balzer, A. Rieder, and J. Beyerer, "Shape from specular reflection and optical flow," *International Journal of Computer Vision*, vol. 80, pp. 226–241, Nov. 2008.

[76] J. Seyama and T. Sato, "Shape from shading: estimation of reflectance map," *Vision Research*, vol. 38, pp. 3805–3815, Dec. 1998.

[77] K. Yoon, E. Prados, and P. Sturm, "Joint estimation of shape and reflectance using multiple images with known illumination conditions," *International Journal of Computer Vision*, vol. 86, no. 2, pp. 192–210, 2010.

[78] R. Feris, R. Raskar, K.-H. Tan, and M. Turk, "Specular reflection reduction with multi-flash imaging," in *Computer Graphics and Image Processing, 2004. Proceedings. 17th Brazilian Symposium on*, pp. 316–321, 17-20 Oct. 2004.

[79] J. Toro, "Dichromatic illumination estimation without presegmentation," *Pattern Recognition Letters*, vol. 29, pp. 871–877, May 2008.

[80] A. Gijsenij, T. Gevers, and J. van de Weijer, "Generalized gamut mapping using image derivative structures for color constancy," *International Journal of Computer Vision*, vol. 86, no. 2, pp. 127–139, 2010.

[81] R. T. Tan, K. Nishino, and K. Ikeuchi, "Color constancy through inverse-intensity chromaticity space.," *J Opt Soc Am A Opt Image Sci Vis*, vol. 21, pp. 321–334, Mar 2004.

[82] R. Tan and K. Ikeuchi, "Reflection components decomposition of textured surfaces using linear basis functions," in *Computer Vision and Pattern Recognition, 2005. CVPR 2005. IEEE Computer Society Conference on*, vol. 1, pp. 125–131vol.1, 20-25 June 2005.

[83] H. Shen, H. Zhang, S. Shao, and J. H. Xin, "Chromaticity-based separation of reflection components in a single image," *Pattern Recognition*, vol. 41, pp. 2461–2469, Aug. 2008.

[84] R. Tan and K. Ikeuchi, "Separating reflection components of textured surfaces using a single image," in *Computer Vision, 2003. Proceedings. Ninth IEEE International Conference on*, pp. 870–877 vol.2, 2003.

[85] S. Umeyama and G. Godin, "Separation of diffuse and specular components of surface reflection by use of polarization and statistical analysis of images," *IEEE Trans. Pattern Anal. Mach. Intell.*, vol. 26, no. 5, pp. 639–647, 2004.

[86] K. Yoon and I. Kweon, "Voting-based separation of diffuse and specular pixels," *Electronics Letters*, vol. 40, no. 20, pp. 1260–1261, 2004.

[87] K.-J. Yoon, Y. Choi, and I. S. Kweon, "Fast separation of reflection components using a specularity-invariant image representation," in *Image Processing, 2006 IEEE International Conference on*, pp. 973–976, 8-11 Oct. 2006.

[88] J. Li, J. M. Bioucas-Dias, and A. Plaza, "Semi-supervised hyperspectral image segmentation," in *First Workshop on Hyperspectral Image and Signal Processing: Evolution in Remote Sensing, 2009. WHISPERS '09*, pp. 1–4, IEEE, Aug. 2009.

[89] R. Moreno, J. López-Guede, and A. d'Anjou, "Hybrid color space transformation to visualize color constancy," in *Hybrid Artificial Intelligence*

Systems, vol. 6077 of *Lecture Notes in Computer Science*, pp. 241–247, Springer Berlin / Heidelberg, 2010.

[90] M. Styner, C. Brechbuhler, G. Szckely, and G. Gerig, "Parametric estimate of intensity inhomogeneities applied to mri," *Medical Imaging, IEEE Transactions on*, vol. 19, pp. 153–165, 2000.

[91] R. T. Tan, K. Nishino, and K. Ikeuchi, "Separating reflection components based on chromaticity and noise analysis.," *IEEE Trans Pattern Anal Mach Intell*, vol. 26, pp. 1373–1379, Oct 2004.

[92] T. M. Lehmann and C. Palm, "color line search for illuminant estimation in real-word scenes," *Journal of the Optical Society of America A*, vol. 18, pp. 2679–2691, 2001.

[93] G. Winkler, *Image analysis, random fields and dynamic Monte Carlo methods*. Springer Verlag, 1995.

[94] E. Oja, "Principal components, minor components, and linear neural networks," *Neural Networks*, vol. 5, no. 6, pp. 927 – 935, 1992.

[95] R. Moreno, M. Graña, and A. d'Anjou, "A color transformation for robust detection of color landmarks in robotic contexts," in *Trends in Practical Applications of Agents and Multiagent Systems*, vol. 71 of *Advances in Soft Computing*, pp. 665–672, Springer Berlin / Heidelberg, 2010.

[96] R. Moreno, M. Grañ anda, and A. d'Anjou, "An image color gradient preserving color constancy," in *Fuzzy Systems (FUZZ), 2010 IEEE International Conference on*, pp. 1 –5, july 2010.

[97] S. Skaff, T. Arbel, and J. J. Clark, "A sequential bayesian approach to color constancy using non-uniform filters," *Computer Vision and Image Understanding*, vol. 113, pp. 993–1004, Sept. 2009.

[98] O. Lézoray and C. Charrier, "Color image segmentation using morphological clustering and fusion with automatic scale selection," *Pattern Recognition Letters*, vol. 30, pp. 397–406, Mar. 2009.

[99] R. Moreno, M. Graña, and E. Zulueta, "Rgb colour gradient following colour constancy preservation," *Electronics Letters*, vol. 46, no. 13, pp. 908–910, 2010.

[100] D. Martin, C. Fowlkes, D. Tal, and J. Malik, "A database of human segmented natural images and its application to evaluating segmentation algorithms and measuring ecological statistics," in *Proc. 8th Int'l Conf. Computer Vision*, vol. 2, pp. 416–423, July 2001.

[101] H. Takagi, "Interactive evolutionary computation: Fusion of the capacities of ec optimization and human evaluation.," *Proceedings of the IEEE*, vol. 89, no. 9, pp. 1275–1296, 2001.

[102] H. Beyer and H. Schwefel, "Evolution strategies: A comprehensive introduction," *Journal Natural Computing*, vol. 1, no. 1, pp. 3–52, 2002.

[103] Y. Tarabalka, J. Chanussot, and J. A. Benediktsson, "Segmentation and classification of hyperspectral images using watershed transformation," *Pattern Recogn.*, vol. 43, no. 7, pp. 2367–2379, 2010.

[104] J. Angulo and J. Serra, "Modelling and segmentation of colour images in polar representations," *Image and Vision Computing*, vol. 25, pp. 475–495, Apr. 2007.

[105] A. Backhaus, F. Bollenbeck, and U. Seiffert, "Robust classification of the nutrition state in crop plants by hyperspectral imaging and artificial neural networks," in *Hyperspectral Image and Signal Processing: Evolution in Remote Sensing (WHISPERS), 2011 3rd Workshop on*, pp. 1–4, 2011.

[106] A. Braun, U. Weidner, and S. Hinz, "Support vector machines, import vector machines and relevance vector machines for hyperspectral classification — a comparison," in *Hyperspectral Image and Signal Processing: Evolution in Remote Sensing (WHISPERS), 2011 3rd Workshop on*, pp. 1–4, 2011.

[107] G. Erins, A. Lorencs, I. Mednieks, and J. Sinica-Sinavskis, "Tree species classification in mixed baltic forest," in *Hyperspectral Image and Signal Processing: Evolution in Remote Sensing (WHISPERS), 2011 3rd Workshop on*, pp. 1–4, 2011.

[108] M. Marin-McGee and M. Velez-Reyes, "A structure tensor for hyperspectral images," in *Hyperspectral Image and Signal Processing: Evolution in Remote Sensing (WHISPERS), 2011 3rd Workshop on*, pp. 1–4, 2011.

[109] R. Mercovich, J. Albano, and D. Messinger, "Techniques for the graph representation of spectral imagery," in *Hyperspectral Image and Signal Processing: Evolution in Remote Sensing (WHISPERS), 2011 3rd Workshop on*, pp. 1–4, 2011.

[110] D. Cerra, J. Bieniarz, J. Avbelj, P. Reinartz, and R. Mueller, "Compression-based unsupervised clustering of spectral signatures," in *Hyperspectral Image and Signal Processing: Evolution in Remote Sensing (WHISPERS), 2011 3rd Workshop on*, pp. 1–4, 2011.

[111] S. Henrot, C. Soussen, and D. Brie, "Fast deconvolution of large fluorescence hyperspectral images," in *Hyperspectral Image and Signal Processing: Evolution in Remote Sensing (WHISPERS), 2011 3rd Workshop on*, pp. 1–4, 2011.

[112] P. Horstrand, S. Lopez, G. Callico, J. Lopez, and R. Sarmiento, "Novel architectures for real-time matching in hyperspectral images," in *Hyperspectral Image and Signal Processing: Evolution in Remote Sensing (WHISPERS), 2011 3rd Workshop on*, pp. 1–4, 2011.

[113] A. Brook and E. Ben Dor, "Supervised vicarious calibration (SVC) of hyperspectral remote-sensing data," in *Hyperspectral Image and Signal Processing: Evolution in Remote Sensing (WHISPERS), 2011 3rd Workshop on*, pp. 1–5, 2011.

[114] S. Qian, M. Maszkiewicz, A. Hollinger, E. Thibeault, E. Martin, J. Ardouin, and A. Jouan, "Development of compact and low distortion imaging spectrometer for mars missions and airborne aerial vehicles," in *Hyperspectral Image and Signal Processing: Evolution in Remote Sensing (WHISPERS), 2011 3rd Workshop on*, pp. 1–4, 2011.

[115] L. Zhang, J. Wang, J. Fang, Y. Xue, and Q. Tong, "A field imaging spectrometer system," in *Hyperspectral Image and Signal Processing: Evolution in Remote Sensing (WHISPERS), 2011 3rd Workshop on*, pp. 1–4, 2011.

[116] X. Briottet, R. Marion, V. Carrere, S. Jacquemoud, S. Chevrel, P. Prastault, M. D'oria, P. Gilouppe, S. Hosford, B. Lubac, and

A. Bourguignon, "HYPXIM: a new hyperspectral sensor combining science/defence applications," in *Hyperspectral Image and Signal Processing: Evolution in Remote Sensing (WHISPERS), 2011 3rd Workshop on*, pp. 1–4, 2011.

[117] M. Mitchley, M. Sears, and S. Damelin, "Target detection in hyperspectral mineral data using wavelet analysis," in *Geoscience and Remote Sensing Symposium,2009 IEEE International,IGARSS 2009*, vol. 4, pp. IV–881–IV–884, 2009.

[118] F. Soulez, S. Bongard, E. Thiebaut, and R. Bacon, "Restoration of hyperspectral astronomical data from integral field spectrograph," in *Hyperspectral Image and Signal Processing: Evolution in Remote Sensing (WHISPERS), 2011 3rd Workshop on*, pp. 1–4, 2011.

[119] S. Bourguignon, H. Carfantan, E. Slezak, and D. Mary, "Sparsity-based spatial-spectral restoration of muse astrophysical hyperspectral data cubes," in *Hyperspectral Image and Signal Processing: Evolution in Remote Sensing (WHISPERS), 2011 3rd Workshop on*, pp. 1–4, 2011.

[120] I. Meganem, Y. Deville, S. Hosseini, H. Carfantan, and M. Karoui, "Extraction of stellar spectra from dense fields in hyperspectral muse data cubes using non-negative matrix factorization," in *Hyperspectral Image and Signal Processing: Evolution in Remote Sensing (WHISPERS), 2011 3rd Workshop on*, pp. 1–4, 2011.

[121] O. Berne, M. Rosenberg, and A. Tielens, "Explaining mid-infrared astronomical spectra: Non-negative matrix factorization vs theoretical spectroscopic database," in *Hyperspectral Image and Signal Processing: Evolution in Remote Sensing (WHISPERS), 2011 3rd Workshop on*, pp. 1–4, 2011.

[122] D. Goodenough, G. Quinn, K. OlafNiemann, H. Chen, and D. Ton, "Helicopter high resolution imaging spectroscopy: Mapping species variation," in *Hyperspectral Image and Signal Processing: Evolution in Remote Sensing (WHISPERS), 2011 3rd Workshop on*, pp. 1–4, 2011.

[123] E. Torrecilla, J. Piera, A. Bracher, B. Taylor, and A. Bernhardt, "Spectral range sensitivity analysis to improve hyperspectral remote sensing of phytoplankton biodiversity in the ocean," in *Hyperspectral Image*

and Signal Processing: Evolution in Remote Sensing (WHISPERS), 2011 3rd Workshop on, pp. 1–4, 2011.

[124] S. Serranti, A. Gargiulo, and G. Bonifazi, "Hyperspectral imaging based platforms for particulate solids characterization, inspection and quality control. case studies: Application to polyolefins recycling," in *Hyperspectral Image and Signal Processing: Evolution in Remote Sensing (WHISPERS), 2011 3rd Workshop on*, pp. 1–4, 2011.

[125] B. Rivard, J. Feng, V. Bushan, and M. Lipsett, "Infrared reflectance hyperspectral features of athabasca oil sand ore and froth," in *Hyperspectral Image and Signal Processing: Evolution in Remote Sensing (WHISPERS), 2011 3rd Workshop on*, pp. 1–4, 2011.

[126] M. Lopes, J. Bioucas-Dias, M. Figueiredo, J. Wolff, N. Mistry, and J. Warrack, "Comparison of near infrared and raman hyperspectral unmixing performances for chemical identification of pharmaceutical tablets," in *Hyperspectral Image and Signal Processing: Evolution in Remote Sensing (WHISPERS), 2011 3rd Workshop on*, pp. 1–4, 2011.

[127] D. Lorts, "Real-time embedded hyperspectral image compression for tactical military platforms," in *Applied Imagery Pattern Recognition Workshop, 2002. Proceedings. 31st*, p. 140, 2002.

[128] A. Schaum and A. Stocker, "Advanced algorithms for autonomous hyperspectral change detection," in *Information Theory, 2004. ISIT 2004. Proceedings. International Symposium on*, pp. 33–38, 2004.

[129] M. Genisio, "New concepts in airborne and ground surveillance systems," in *Advanced Video and Signal-Based Surveillance (AVSS), 2011 8th IEEE International Conference on*, p. 507, 2011.

[130] T. Veracini, S. Matteoli, M. Diani, and G. Corsini, "An anomaly detection architecture based on a data-adaptive density estimation," in *Hyperspectral Image and Signal Processing: Evolution in Remote Sensing (WHISPERS), 2011 3rd Workshop on*, pp. 1–4, 2011.

[131] P. Bajorski, "Directional segmented matched filter for hyperspectral images," in *Hyperspectral Image and Signal Processing: Evolution in Remote Sensing (WHISPERS), 2011 3rd Workshop on*, pp. 1–4, 2011.

[132] L. Guozhu, S. Kaishan, and N. Shuwen, “Soybean LAI estimation with in-situ collected hyperspectral data based on BP-neural networks,” in *Recent Advances in Space Technologies, 2007. RAST ’07. 3rd International Conference on*, pp. 331–336, 2007.

[133] D. Krezhova and E. Kirova, “Hyperspectral remote sensing of the impact of environmental stresses on nitrogen fixing soybean plants (Glycine max l.),” in *Recent Advances in Space Technologies (RAST), 2011 5th International Conference on*, pp. 172–177, 2011.

[134] S. Monteiro, Y. Minekawa, Y. Kosugi, T. Akazawa, and K. Oda, “Prediction of sweetness and nitrogen content in soybean crops from high resolution hyperspectral imagery,” in *Geoscience and Remote Sensing Symposium, 2006. IGARSS 2006. IEEE International Conference on*, pp. 2263–2266, 2006.

[135] S. T. Monteiro, Y. Minekawa, Y. Kosugi, T. Akazawa, and K. Oda, “Prediction of sweetness and amino acid content in soybean crops from hyperspectral imagery,” *ISPRS Journal of Photogrammetry and Remote Sensing*, vol. 62, no. 1, pp. 2 – 12, 2007.

[136] Z. Zhou, Y. Zang, B. Shen, X. Zhou, and X. Luo, “Detection of cowpea weevil (Callosobruchus maculatus (F.)) in soybean with hyperspectral spectrometry and a backpropagation neural network,” in *Natural Computation (ICNC), 2010 Sixth International Conference on*, vol. 3, pp. 1223–1227, 2010.

[137] J. Clevers and L. Kooistra, “Using hyperspectral remote sensing data for retrieving total canopy chlorophyll and nitrogen content,” in *Hyperspectral Image and Signal Processing: Evolution in Remote Sensing (WHISPERS), 2011 3rd Workshop on*, pp. 1–4, 2011.

[138] J. Feret, G. Asner, and S. Jacquemoud, “Regularization of discriminant analysis for the study of biodiversity in humid tropical forests,” in *Hyperspectral Image and Signal Processing: Evolution in Remote Sensing (WHISPERS), 2011 3rd Workshop on*, pp. 1–4, 2011.

[139] X. Ye and K. Sakai, “Application of airborne hyperspectral imagery to estimating fruit yield in citrus,” in *Hyperspectral Image and Signal Processing: Evolution in Remote Sensing (WHISPERS), 2011 3rd Workshop on*, pp. 1–6, 2011.

[140] V. Dinh, R. Leitner, P. Paclik, and R. Duin, "A clustering based method for edge detection in hyperspectral images," in *Image Analysis* (A.-B. Salberg, J. Hardeberg, and R. Jenssen, eds.), vol. 5575 of *Lecture Notes in Computer Science*, pp. 580–587, Springer Berlin / Heidelberg, 2009.

[141] Y. Zhou, B. Wu, D. Li, and R. Li, "Edge detection on hyperspectral imagery via manifold techniques," in *First Workshop on Hyperspectral Image and Signal Processing: Evolution in Remote Sensing, 2009. WHISPERS '09*, pp. 1–4, IEEE, Aug. 2009.

[142] W. Bakker and K. Schmidt, "Hyperspectral edge filtering for measuring homogeneity of surface cover types," *ISPRS Journal of Photogrammetry and Remote Sensing*, vol. 56, pp. 246–256, July 2002.

[143] M. A. Lee and L. M. Bruce, "Applying cellular automata to hyperspectral edge detection," in *Geoscience and Remote Sensing Symposium (IGARSS), 2010 IEEE International*, pp. 2202–2205, IEEE, July 2010.

[144] W. Luo and L. Zhong, "Spectral similarity measure edge detection algorithm in hyperspectral image," in *2nd International Congress on Image and Signal Processing, 2009. CISP '09*, pp. 1–4, IEEE, Oct. 2009.

[145] S. Schiefer, P. Hostert, and A. Damm, "Correcting brightness gradients in hyperspectral data from urban areas," *Remote Sensing of Environment*, vol. 101, pp. 25–37, Mar. 2006.

[146] C. Huynh and A. Robles-Kelly, "A solution of the dichromatic model for multispectral photometric invariance," *International Journal of Computer Vision*, vol. 90, pp. 1–27, 2010. 10.1007/s11263-010-0333-y.

[147] D. H. Foster, S. M. Nascimento, and K. Amano, "Information limits on neural identification of colored surfaces in natural scenes," *Visual neuroscience*, vol. 21, no. 3, pp. 331–336, 2004. PMID: 15518209 PMCID: 1991287.

[148] J. Li, J. M. Bioucas-Dias, and A. Plaza, "Hyperspectral image segmentation using a new bayesian approach with active learning," *IEEE Transactions on Geoscience and Remote Sensing*, vol. 49, pp. 3947–3960, Oct. 2011.

[149] J. Li, J. M. Bioucas-Dias, and A. Plaza, "Supervised hyperspectral image segmentation using active learning," in *2010 2nd Workshop on Hyperspectral Image and Signal Processing: Evolution in Remote Sensing (WHISPERS)*, pp. 1–4, IEEE, June 2010.

[150] J. S. Borges, J. M. Bioucas-Dias, and A. R. Marcal, "Bayesian hyperspectral image segmentation with discriminative class learning," *IEEE Transactions on Geoscience and Remote Sensing*, vol. 49, pp. 2151–2164, June 2011.

[151] J. Li, J. M. Bioucas-Dias, and A. Plaza, "Spectral–Spatial hyperspectral image segmentation using subspace multinomial logistic regression and markov random fields," *IEEE Transactions on Geoscience and Remote Sensing*, vol. PP, no. 99, pp. 1–15.

[152] J. Li, J. M. Bioucas-Dias, and A. Plaza, "Semisupervised hyperspectral image segmentation using multinomial logistic regression with active learning," *IEEE Transactions on Geoscience and Remote Sensing*, vol. 48, pp. 4085–4098, Nov. 2010.

[153] G. Mercier, S. Derrode, and M. Lennon, "Hyperspectral image segmentation with markov chain model," in *Geoscience and Remote Sensing Symposium, 2003. IGARSS '03. Proceedings. 2003 IEEE International*, vol. 6, pp. 3766– 3768 vol.6, IEEE, July 2003.

[154] N. Acito, G. Corsini, and M. Diani, "An unsupervised algorithm for hyperspectral image segmentation based on the gaussian mixture model," in *Geoscience and Remote Sensing Symposium, 2003. IGARSS '03. Proceedings. 2003 IEEE International*, vol. 6, pp. 3745– 3747 vol.6, IEEE, July 2003.

[155] G. Bilgin, S. Erturk, and T. Yildirim, "Segmentation of hyperspectral images via subtractive clustering and cluster validation using One-Class support vector machines," *IEEE Transactions on Geoscience and Remote Sensing*, vol. 49, pp. 2936–2944, Aug. 2011.

[156] A. Erturk and S. Erturk, "Unsupervised segmentation of hyperspectral images using modified phase correlation," *IEEE Geoscience and Remote Sensing Letters*, vol. 3, pp. 527–531, Oct. 2006.

[157] N. Gorretta, J. M. Roger, G. Rabatel, V. Bellon-Maurel, C. Fiorio, and C. Lelong, "Hyperspectral image segmentation: The butterfly approach," in *First Workshop on Hyperspectral Image and Signal Processing: Evolution in Remote Sensing, 2009. WHISPERS '09*, pp. 1–4, IEEE, Aug. 2009.

[158] J. Zhang, J. Chen, Y. Zhang, and B. Zou, "Hyperspectral image segmentation method based on spatial-spectral constrained region active contour," in *Geoscience and Remote Sensing Symposium (IGARSS), 2010 IEEE International*, pp. 2214–2217, IEEE, July 2010.